



Advances and challenges of ammonia delivery by urea-water sprays in SCR systems

M. Börnhorst^{a,c}, O. Deutschmann^{a,b,c,*}

^a Institute for Chemical Technology and Polymer Chemistry, Karlsruhe Institute of Technology (KIT)

^b Institute for Catalysis Research and Technology, Karlsruhe Institute of Technology (KIT)

^c Karlsruhe Institute of Technology (KIT), Kaiserstr. 12, Karlsruhe 76128, Germany

ARTICLE INFO

Keywords:

Urea
Selective catalytic reduction
Spray/wall interaction
Deposits

ABSTRACT

Over the past decades, selective catalytic reduction (SCR) using aqueous urea sprays as ammonia precursor has become the prevalent technique for NO_x emission control in mobile applications. Preparation of ammonia from urea water sprays still represents a challenge in aftertreatment engineering as complex interactions of multi-phase physics and chemical reactions have to be handled. Increasingly stringent emission legislations and the ongoing development of fuel-efficient engines and close-coupled aftertreatment systems raise high demands to SCR systems. Due to highly transient conditions and short mixing lengths, incomplete spray evaporation can result in liquid/wall contact and formation of solid urea deposits lowering ammonia selectivity and homogeneity. This article reviews the ongoing development of SCR systems with focus on the efficient evaporation and decomposition of the injected spray for a homogeneous ammonia distribution in front of the SCR catalyst. Critical aspects of spray evaporation and impingement, liquid film and deposit formation are pointed out and potentials for system optimization are discussed.

1. Controlling NO_x emissions of internal combustion engines

Internal combustion engines always produce nitrogen oxides to a certain extent due to the use of air as oxidizing agent. Many primary, on the engine operation side, and secondary measures, on the emission aftertreatment side, have been developed and applied over the last decades to reduce the amount of NO_x emitted from internal combustion (IC) engines. In the last decade, the challenge of NO_x emission control has gained a worldwide public attention in particular for Diesel operated passenger cars. While the after-treatment of nitrogen oxide emissions seemed to be solved at stoichiometric operating conditions applying the conventional three-way catalytic converter as aftertreatment device, the problem became obvious for lean operation, which otherwise helps to reduce fuel consumption and, consequently, reduces the emission of the greenhouse gas (GHG) CO₂.

Hence, NO_x raw emissions have to be treated not only in Diesel operated passenger cars but also in lean-operated engines using any other fuel including hydrogen as long as air is the oxidizing agent. Substitution of Diesel operated passenger cars by hybrid (battery/IC engine) vehicles may be even counter-productive in terms of GHG emissions if these vehicles are equipped with a rather strong gasoline

fueled engine and taking into account the current sources of electricity in most countries of the world. Even the fast substitution of efficient Diesel operated vehicles by huge fleets of battery electric vehicles may not lead to the desired reduction of GHG emissions, because the additionally needed electricity is often provided by the combustion of fossil fuels [1].

In order to reduce GHG emissions, natural gas fueled IC engines have gained significant interest and a certain market share in some countries and sectors. In some regions of the world, liquefied and compressed natural gas are popular fuels for cars, light and heavy duty vehicles, even though their main application is expected to be in ships, combined heat and power plants, and power generators. Natural gas engines may become even more attractive when fueled with *green* methane produced by methanation, a reaction of *green* hydrogen and CO and/or CO₂, or biogas. The most efficient operation mode again is the lean one, which however results not only in a significant amount of NO_x in the raw emissions but also in slip of the strong GHG methane, even though beneficial primary measures are applied such as advanced direct injection strategies [2]. There is still no reliable catalyst technology available for the low-temperature aftertreatment of CH₄ [3].

In the future, the availability of green hydrogen, produced by electrolyzers using solar and wind power may boost the use of hydrogen

* Corresponding author.

E-mail address: deutschmann@kit.edu (O. Deutschmann).

<https://doi.org/10.1016/j.pecs.2021.100949>

Received 14 December 2020; Received in revised form 12 July 2021; Accepted 21 July 2021

Available online 7 August 2021

0360-1285/© 2021 The Authors. Published by Elsevier Ltd. This is an open access article under the CC BY license (<http://creativecommons.org/licenses/by/4.0/>).

Nomenclature*Greek Symbols*

β	Spreading factor
η	Dynamic viscosity
ρ	Density
σ	Surface tension
θ	Contact angle

Latin Symbols

\dot{m}	Mass flow
A	Area
d	Diameter
d_{32}	Sauter mean diameter
G	Spray mass flux
K	Splashing parameter
L	Characteristic length scale
La	Laplace number
Oh	Ohnesorge number
q	Heat flux
r	Radius

R_a	Mean roughness
Re	Reynolds number
T	Temperature
t	Time
T^*	Dimensionless temperature
u	Velocity
We	Weber number

Subscripts

0	Initial
B	Boiling
CHF	Critical heat flux
cr	Critical
d	Droplet
LF	Leidenfrost
l	Liquid
max	Maximum
N	Nukiyama
sp	Spray
v	Vapor
w	Wall

fueled engines, in particular in the transportation sector [4]. The GHG free exhaust of these engines will still contain NO_x . Here, the use of hydrogen as reducing agent for NO_x conversion seems attractive but no reliable technology is available. State-of-the-art catalysts do not work over sufficiently wide temperature, produce rather high amounts of the GHG N_2O and are not very selective, i.e., the catalysts simply burn most of the reducing agent H_2 [5]. Hence, the control of NO_x emissions of internal combustion engines has to be taken care of even in the light of the transitions we are expected to see in the transportation and energy sectors in the next decades.

The concentration of pollutants in the raw exhaust mainly depends on fuel and combustion mode. As primary measure, the raw exhaust emissions can be affected by the motor operation mode. For example, controlling the air/fuel ratio according to motor operation or a recirculation of the exhaust gas can bring benefits with respect to emission concentrations. Regarding particulate matter (PM) and NO_x emissions from diesel engines, a trade-off occurs, which can be managed by motor operation. Another trade-off, in particular for NO_x emissions, has often to be considered in terms of fuel consumption and exhaust pollutant concentration. As secondary measure, exhaust gas aftertreatment systems are designed to reduce pollutant emissions. System configurations do not only need to fit the requirements resulting from operation range and motor control but also the installation space restrictions arising from various vehicle geometries. Modern exhaust gas aftertreatment systems represent a combination of different components responsible for the removal of one or more pollutants. Due to consecutive or combined arrangements, thermal and chemical interactions between the aftertreatment components have to be considered. Therefore, the following paragraphs give an overview on the different components of the exhaust gas aftertreatment system for lean-operated engines, today mainly fueled by diesel.

Selective Catalytic Reduction Selective catalytic reduction (SCR) catalysts using ammonia as reductant have been commercialized for NO_x removal in the stationary sector for decades. Selective catalytic reduction of nitrogen oxide emissions describes the conversion of NO_x to nitrogen (N_2) and water on a catalyst using ammonia as reducing agent. Commonly applied SCR catalysts are vanadia, Cu-zeolites and Fe-zeolites prepared on a monolithic support. Depending on the $\text{NO}_2:\text{NO}_x$ ratio and temperature, different reactions occur on the catalyst. Eq. (1.1) shows the *standard* SCR reaction. The fastest and preferred reaction is presented in Eq. (1.2), the *fast* SCR reaction. This is commonly promoted

by a diesel oxidation catalyst (DOC) converting NO to NO_2 . An excess of NO_2 results in the *slow* SCR reaction, (1.3), which is undesirable since it may yield N_2O as by-product.



The catalyst performance is mainly dependent on the catalyst composition and aging condition. NO_x conversion efficiency strongly depends on the gas temperature. The light-off region for commonly used SCR catalysts is 200–300 °C.

Due to its toxic properties and resulting safety issues, ammonia is supplied by an aqueous urea solution. The majority of mobile SCR applications carry a 32.5wt.-% urea solution commercially named *AdBlue®* in Europe and Diesel Exhaust Fluid (DEF) in the USA. The urea concentration of 32.5wt.-% was chosen because it marks the eutectic mixture of urea and water resulting in the lowest possible melting/freezing point of –11 °C. The precursor liquid is sprayed into the tailpipe in front of the SCR catalyst, as shown in Fig. 1.

In the mixing section the spray droplets evaporate and ammonia is generated by two-step thermal decomposition of urea. Urea melts at a

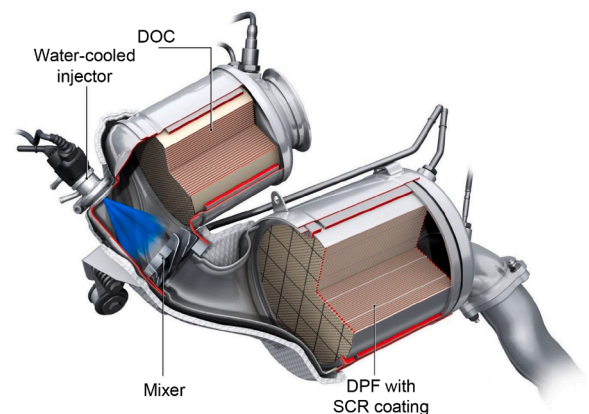


Fig. 1. Close-coupled exhaust gas aftertreatment system including a diesel oxidation catalyst (DOC) and an SCR coated diesel particle filter (DPF) [6].

temperature of 133 °C and simultaneously starts to decompose in two steps. By thermolysis, urea reacts to isocyanic acid (HNCO) and ammonia (NH₃). In a second step isocyanic acid is hydrolyzed to ammonia and carbon dioxide (CO₂):



Complete conversion of urea to ammonia and a homogeneous distribution of ammonia over the tailpipe cross-section in front of the SCR catalyst is necessary for efficient NO_x removal. In case of a non-homogeneous distribution or excess of ammonia due to highly transient operating conditions, it may exit the SCR catalyst referred to as ammonia slip. To support spray preparation, mixing devices are commonly placed between the injection position and SCR catalyst (Fig. 1) maintaining multiple functions, which will be discussed in Section 7. However, spray preparation and urea decomposition is not trivial and has remained a challenging task, which will be addressed in Section 2. [7]

Mobile SCR systems are an efficient tool for NO_x abatement and are commonly installed in heavy duty vehicles and large size passenger cars. However, the additional efforts for AdBlue® fill-up and carriage, spray injection and urea decomposition raise recurring discussions about potential alternatives. Great effort has been put in finding alternative sources for ammonia in order to decrease size and cost of the system and to enable SCR application at low ambient temperatures. Approaches for alternative ammonia precursors are given by ammonium formate [8], methanamide [9] solid ammonium carbamate [10,11] and metal ammine chloride salts [12] representing only few examples. All these approaches offer advantages and disadvantages in terms of melting point, ammonia storage capacity and ammonia yield. However, until now their qualities have remained insufficient for a substitution of urea as commercial SCR reducing agent.

In order to remove excess ammonia an ammonia slip catalyst (ASC) can be installed downstream the SCR catalyst to oxidize ammonia to N₂ and water. Besides oxidation of unreacted ammonia, undesired formation of nitrous oxide may occur if NO is still present in the exhaust gas as a consequence of poor urea conversion and mixing or an insufficient urea dosing amount. [7]

NO_x Storage Catalyst

A NO_x storage catalyst (NSC) or lean NO_x trap (LNT) can be applied for reduction of nitrogen oxide emissions in lean combustion processes with excess air. Alkaline or alkaline earth metals like BaCO₃ are used as storage material. Platinum and rhodium are the commonly used catalytically active materials. During lean operation, NO₂ is continuously stored as nitrate, e. g. Ba(NO₃)₂. Since NO is not stored in an NSC, an efficient DOC has to be installed upstream or integrated to the NSC. When a high catalyst loading is reached, the catalyst is regenerated by a short period of rich operation (lack of oxygen). Stored nitrogen oxide is then oxidized by reducing agents from the rich exhaust gas, such as CO and HC. Oxidation reaction can result in undesired production of ammonia (NH₃) or nitrous oxide N₂O, which is a strong greenhouse gas. Although selective catalytic reduction (SCR) shows a better efficiency for NO_x removal, the NSC is characterized by its simplicity and does not require an additional tank for the reducing agent. [13]

Diesel Oxidation Catalyst

A DOC is used for oxidation of CO, HC (hydrocarbons) and NO under excess of oxygen. Depending on exhaust gas composition, flow velocity and catalyst material an almost complete oxidation of CO to CO₂ and HC to CO₂ and water vapor is found above a certain temperature, the light-off temperature (170 - 200 °C). For oxidation of NO to NO₂, a temperature-dependent equilibrium is reached, which leads to high NO₂ concentrations below 450 °C and high NO concentrations at higher temperatures. The DOC is placed upstream the SCR catalyst to adjust the NO₂:NO_x ratio for optimal performance of the SCR catalytic converter. In addition to the oxidation of emissions, the DOC is used as a catalytic

burner in the active regeneration of the diesel particle filter. Here, unburned fuel is oxidized releasing heat to achieve the regeneration temperatures of above 550 °C. A DOC consists of a ceramic monolith support with porous oxide-washcoat providing a large surface area. Catalytically active materials used in DOCs are platinum, palladium and rhodium [7].

Diesel Particle Filter Ash and soot particles produced during combustion in the diesel engine are separated from the exhaust gas by a diesel particle filter (DPF). Ceramics such as silicon carbide or cordierite in the form of a honeycomb body with a large number of parallel channels are commonly used as filter material. The adjacent channels are closed alternately forcing the exhaust gas to diffuse through the porous walls. Fig. 2 shows the structure of a DPF in comparison to a monolith catalyst.

The soot particles contained in the exhaust gas may adhere on the surface of the DPF channel walls in the form of a soot layer (surface filtration) or on the pore surface (depth filtration). The gradual increasing soot load leads to an increase of the exhaust gas back pressure, hence requiring a regeneration. A distinction is made between passive and active regeneration. Passive regeneration describes the continuous soot oxidation by a catalytic coating or by NO₂. In active regeneration, fuel is added and the temperature is increased to 600 °C for a controlled soot oxidation. To achieve lower regeneration temperatures, NO₂ is used as oxidant enabling soot oxidation at 250 °C. This requires sufficient conversion of NO by the DOC. [14]

Arrangement of Aftertreatment Systems

Arrangement of the different aftertreatment devices is significant, as each part is dedicated for removal of specific pollutants, while the remaining pollutants may have a promoting or inhibiting effect. For example, HC and CO deplete NO₂ storage at the NSC by reducing relevant NO₂ to NO. For a DPF arranged upstream the NSC or SCR, as shown in Fig. 3 (a) and (b), the DPF regeneration is strongly influenced by NO₂ present in the exhaust. Further, this arrangement facilitates heat-up of the DPF for regeneration and prevents heat losses by NSC or SCR. However, due to the high heat capacity of the DPF the SCR operation temperature is reached late after cold start. Therefore, additional heaters may be required for operating SCR systems. A positive effect can be observed when placing a catalytically coated DPF downstream the SCR, since it additionally functions as ammonia slip catalyst (ASC) and oxidizes ammonia. Fig. 3 shows different arrangements of the presented aftertreatment components with and without usage of urea water solution (UWS) for ammonia generation.

In Fig. 3 (a), an arrangement with combined NSC and SCR catalyst without injection of aqueous urea solution is shown. In comparison, Fig. 3 (b) displays an arrangement with a DeNO_x system consisting of the UWS dosing and SCR catalyst. Fig. 3 (c) shows a configuration with an SCR coated DPF for arrangement in the vicinity of the engine. An SCR coated DPF is an effective measure to reduce total system size. Multifunctional aftertreatment devices gain advantage in cost and sizing of the overall system. For example, a combination of NSC and SCR catalyst reduces installation space and brings advantages of both systems. Under rich conditions, ammonia can be produced on the NSC, which is stored in the SCR catalyst to be released again under lean conditions for NO_x reduction. Another approach is the usage of two consecutive SCR catalysts as described by Balland et al. [15]. Here, the first catalyst is loaded with ammonia by generous ammonia supply. This improves SCR efficiency and cold start management. [7,13]

Recent developments intend to arrange the exhaust gas aftertreatment in the vicinity of the engine, as shown in Fig. 3 (c). With regard to SCR systems, higher temperatures in this region promote UWS spray conversion and increase the catalytic activity for NO_x removal. Fig. 1 shows an exemplary, closed-coupled system containing a DOC and a SCR coated DPF in a tight arrangement with the engine. The system is characterized by a short mixing length. The advantages of the near-engine position are further utilized for double dosing SCR strategies. Here, a second SCR catalyst and UWS dosing is installed in the vehicle underbody in addition to a close-coupled SCR coated DPF. By this

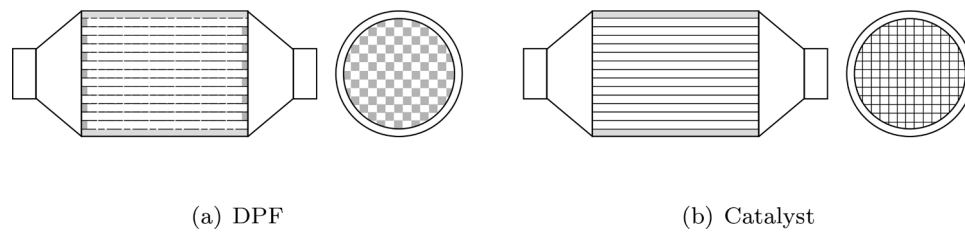


Fig. 2. Monolithic structure of DPF with alternately closed channels in comparison to a catalyst monolith.

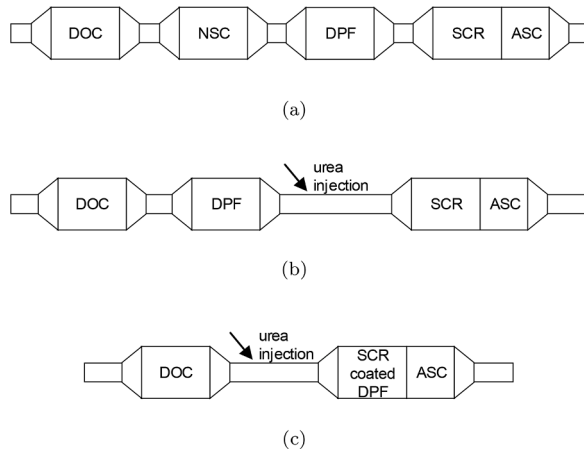


Fig. 3. Schematic of consecutive arrangement of exhaust gas aftertreatment components with different DeNO_x systems: a) combination of NSC and SCR, b) SCR with upstream Urea water solution (UWS) injection c) configuration for close-coupled arrangement to the engine.

arrangement, the catalyst activity is ensured over the entire temperature range. For the combination of DPF and SCR, the influence of soot on the SCR reactions has to be considered. Further, a possible increase of backpressure by the SCR coating and its thermal stability has to be accounted for [7].

2. Challenges of ammonia preparation

High requirements raised by increasingly stringent emission legislations and the ongoing development of more fuel-efficient engines result in the challenge of sufficient spray preparation for NO_x reduction with, at the same time, increasing urea dosing rates and decreasing exhaust temperatures. SCR system efficiency heavily relies on the available amount and homogeneous distribution of ammonia over the tailpipe cross section immediately in front of the catalyst.

The formation of ammonia from UWS comprises droplet evaporation and thermal decomposition of urea in the gas phase as well as urea decomposition from liquid films formed on the mixer, pipe or catalyst surfaces. Due to the highly transient conditions in the tailpipe in terms of exhaust gas flow and temperature and the short distances between injector and SCR catalyst, complete spray evaporation over the wide range of operating conditions remains critical. Incomplete evaporation inevitably is accompanied by the interaction of droplets with mixing devices, tailpipe walls and the catalyst front face, particularly when considering the requirement of high dosing rates to meet today's NO_x emission limits. The increasing trend of close-coupled positioning of the aftertreatment system with tightened spatial restrictions supports these undesired phenomena. Positioning of the SCR system even upstream the turbocharger [16] leads to further challenges due to elevated pressure and mechanical interactions. Furthermore, low exhaust temperatures resulting from increasingly fuel efficient engine operation impede sufficient spray preparation. Until now, UWS is commonly not injected

below temperatures of 180 °C in mobile applications in order to ensure efficient spray evaporation and urea conversion. Therefore, enhancing evaporation and diminishing spray/wall contact is a major objective, in order to decrease this injection threshold and reach sufficient conversion of NO_x over the total operating range.

Spray dispersion and deflection is mainly dependent on the complex interaction of system geometry and resulting flow field, injector mounting and its characteristics, such as injector type, spray angle, droplet size and velocity distribution. When spray impinges on a solid surface in the tailpipe, the exhaust conditions, such as flow velocity and temperature, and the impact conditions such as droplet inertia and wall temperature decide on the outcome of impingement. High thermal and kinetic energies dominating spray impingement lead to secondary atomization, which is beneficial in terms of ammonia generation. For low thermal and kinetic energies, spray impact may result in partial wetting of the surface. Consequently, the surface temperature is decreased by evaporative cooling enhancing further liquid deposition. By accumulation, liquid films are formed on the mixing elements and tailpipe walls [17–19]. Detachment of the liquid film on mixer blade edges can result in formation of large secondary droplets, which are at risk to hit the front face of the catalyst before complete evaporation.

In dependence on temperature distribution and residence time, the urea content of the film can thermally decompose into ammonia and isocyanic acid. However, undesired reactions of the intermediate isocyanic acid can form solid by-products, such as biuret, triuret, cyanuric acid,ammelide and ammeline [20–23]. Solid deposits formed from urea and its by-products modify the surface properties of mixer and tailpipe walls and hence, influence further spray/wall interaction. By decreasing ammonia production and affecting the flow field, ammonia uniformity is impaired. Deposits formed on mixing elements can be detached and entrained by liquid film dynamics and clog the catalyst channels. Increasing deposit growth results in high backpressure and, in severe cases, in a blockage of the tailpipe.

This review discusses the state of the art of ammonia preparation by UWS dosing and points out potentials as well as challenges of NO_x removal by modern SCR systems. The following sections focus on different physical and chemical phenomena in the mixing section of SCR systems, as indicated in Fig. 4: UWS dosing and resulting spray characteristics, droplet evaporation and gas phase reactions, spray/wall interaction, liquid film and deposit formation. Interactions of presented physical and chemical phenomena are reviewed and modeling approaches are given.

3. UWS dosing and spray characteristics

Spray injection, propagation in the turbulent flow field and droplet evaporation are important physical phenomena of the dispersed liquid in the gas phase and strongly affect the overall ammonia conversion and homogenization. Fast evaporation, complete thermal conversion of urea to ammonia and appropriate mixing are desired for a homogeneous ammonia distribution in the gas flow entering the SCR catalyst. Hence, injection and spray characteristics are decisive for the quality of the SCR system. A thorough understanding of the spray properties is required for modeling and design of SCR systems. Optimization of spray quality reduces the risk of droplet impingement, film formation and resulting

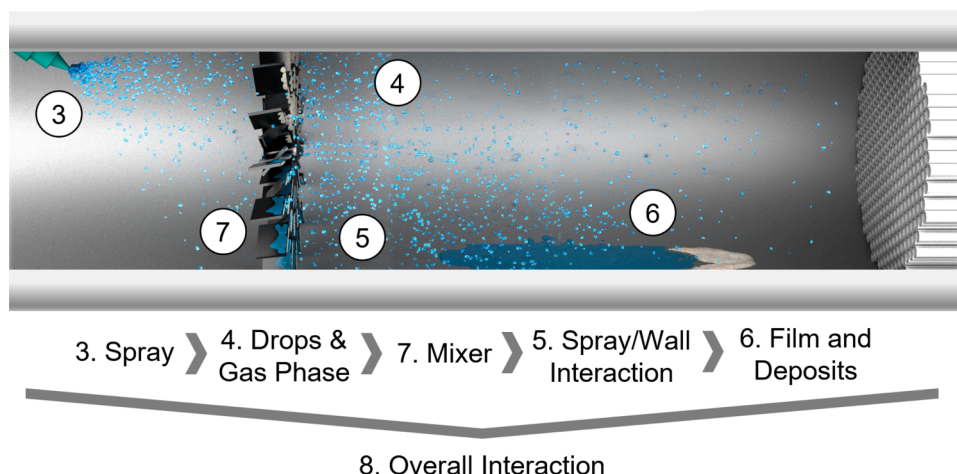


Fig. 4. Schematic of relevant physical and chemical processes in the mixing section of SCR systems. Numbers indicate the respective section number, in which the different phenomena are discussed.

deposit formation.

In mobile applications, UWS injectors are commonly driven by pressures of 3 - 10 bar to generate sprays of 10 - 160 μm depending on injection technology [24]. Spray quality is generally characterized by global and local spray parameters, including the initial jet velocity, the spray angle, spray penetration and both the droplet size and velocity distribution. Knowledge of primary spray parameters is substantial for SCR system design and modeling studies. Investigations on the developed spray characteristics serve to evaluate the effect of operating conditions on spray behavior aiming to reduce the risk of spray impingement and film formation.

Patternators are frequently used for determination of the spray mass flux in quiescent environment. For detailed UWS spray analysis, a wide range of optical methods can be found in literature applied in quiescent and incident flow conditions. Prevalent diagnostics for droplet size and velocity are Laser induced fluorescence (LIF) [25], Long Distance (LD) Microscopy [25–29], Mie scattering [25,26,30,31], Phase doppler anemometry (PDA) [32–34], Particle image velocimetry (PIV) [30,32] and high-speed imaging [30,31,33,35,36]. However, optical spray analysis remains challenging due to the complex layout of modern SCR systems offering limited access close to the nozzle. Furthermore, an intrinsically irregular spray structure characterized by non-spherical droplets, intersections and overlaps impede optical analysis. Particularly at high temperature conditions, sophisticated measurement and post-processing techniques are required [27,28]. Following, different injection technologies and related studies on UWS spray characteristics and their interactions with the operating conditions are discussed.

3.1. Urea-water solution injection

Primary droplet size and velocity distributions of the UWS spray are mainly dependent on injector characteristics and dosing strategy. General system layout, injector position and mounting additionally affect spray penetration. However, due to the large number of individual system designs, these are not discussed at this point. Detailed measurements and a comparison of spray characteristics of different, commercial injectors were performed by Liao et al. [37]. Two primary injection technologies are applied for UWS supply in SCR system: air assisted and airless (pressure-driven) injection. The applied technology is mainly chosen by the respective dosing quantity and spray quality. Spray quality is associated with the initial spray characteristics and their interaction with the flow field (penetration, mixing, droplet entrainment) and solid walls (impingement, secondary atomization, film and deposit formation) [7]. Generally, air assisted injection provides smaller droplet diameters, expressed by the Sauter mean diameter d_{32} , and leads

to stronger entrainment of the droplets due to their size compared to airless injection. Air assisted injection is characterized by good spray mixing and less droplet impingement. However, a comparable mixing length is required due to reduced heat transfer to the droplets for air assisted injection. Furthermore, dosing is difficult as it is less precise and the UWS mass flow is limited. In contrast, pressurized, airless injection results in larger droplets and an increased risk of impingement. Larger relative velocities promote heat transfer, but evaporation time increases with droplet size. In combination with mixing devices, advantages of airless injection can be utilized, as the suitability of the injection technology depends on the individual system layout and urea distribution strategy [38].

For comparison, Fig. 5 shows the spray contours of two example injectors, air assisted and airless, without cross-flow.

For air assisted injection, stabilization of the spray cone width by the co-flowing injector air is observed. For pressure driven, airless injection, the spray cone width is continuously increasing by the initial spray cone angle, resulting in a larger area of potential droplet impingement at the opposite wall. A constant velocity of the spray cone tip is determined whereas for air assisted injection, non-uniform velocity values are measured.

Different spray geometries are applied to reach optimal spray homogenization in the individual systems. For pressure driven injection, pressure swirl and liquid jet (full or hollow cone) injectors are applied. Fig. 6 illustrates the different spray geometries of a pressure swirl injector and a 3-hole liquid jet injector.

The liquid distribution inside the spray body is measured with a patternator for a defined distance to the injector. The pressure swirl injector shows the highest droplet concentration in the center, which is gradually decreasing with larger spray body diameter. For the liquid jet injector, the highest droplet concentration is observed in the three individual spray cones [7]. The liquid distribution is decisive for appropriate mixing and, in case of incomplete evaporation, for the spray impingement pattern on mixing elements and walls.

Valve opening and closing was observed to strongly affect the droplet size distribution of the initial spray. Fig. 7 demonstrates the effect of valve opening on the UWS spray quality.

Images are taken during injection to a test rig without cross-flow using a commercial, pressure-driven 3-hole injector. Initially, a large conglomeration of liquid is injected, which impinges on the wall and forms a liquid film. Subsequently, the primary breakup mechanism effectively produces the specified droplet size distribution. This inhomogeneity in droplet size drastically increases the impinging liquid mass and the risk of film and deposit formation. In particular, pulsed injection systems suffer from this phenomenon, since the injection

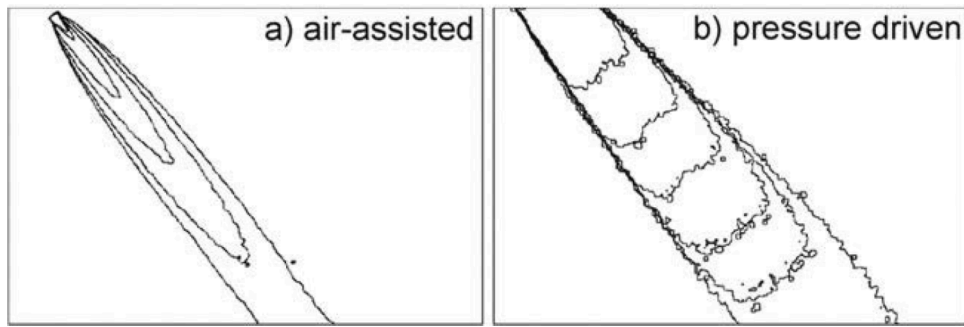


Fig. 5. Spray contours during the start of injection for an air assisted (left) and pressure driven, airless system (right) at low cross-flow conditions. Reprinted by permission from Springer Nature Customer Service Centre GmbH: [38], Springer Nature.

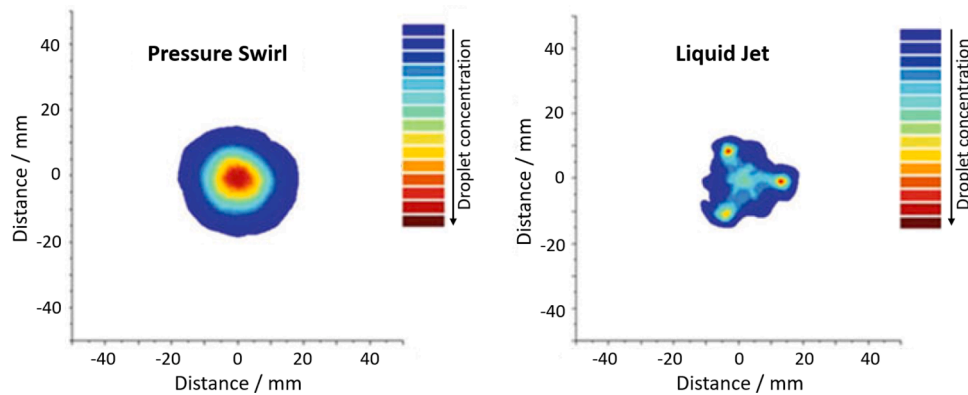


Fig. 6. Liquid distribution for two different spray geometries from airless injection measured by a patternator. Reprinted by permission from Springer Nature Customer Service Centre GmbH: [7], Springer Nature.

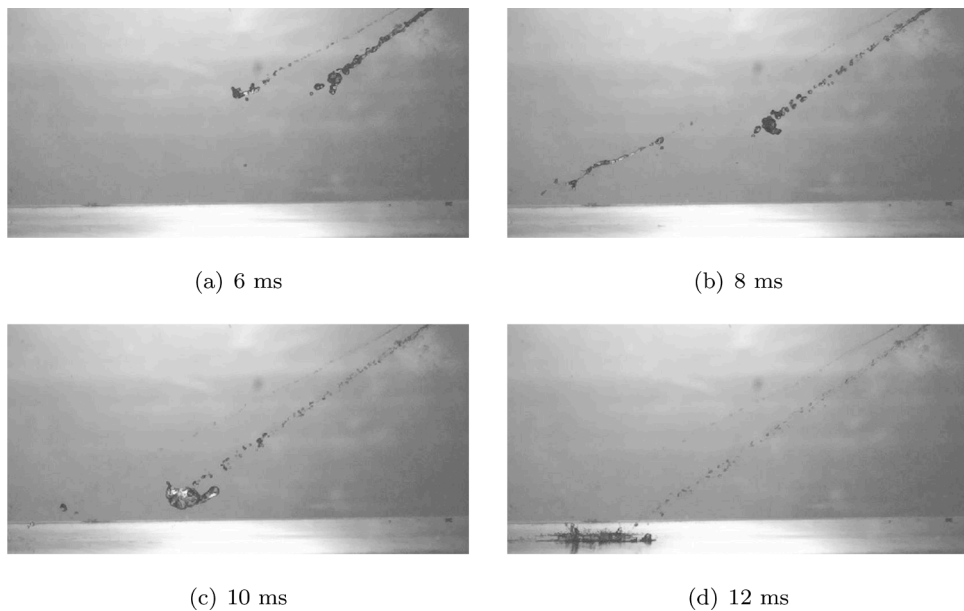


Fig. 7. Effect of valve opening on the initial droplet size distribution of pressure-driven injection. Images show UWS injection by a 3-hole commercial dosing module in quiescent conditions at different time instants after start of injection.

procedure relies on the continuous opening and closing of the valve. This effect has to be considered in spray measurements [34] and for overall system design.

Few studies are available on detailed injector geometry and its influence on the UWS spray development [39–41]. Cai et al. [40]

investigate the influence of nozzle geometry on the draining of UWS by back suction and on potential bubble formation in the injector pipe. The effect of diameter ratio and inclination angle of a simplified nozzle geometry is investigated by Computational Fluid Dynamics (CFD) simulations using a phase-field method. Fig. 8 presents two modifications of

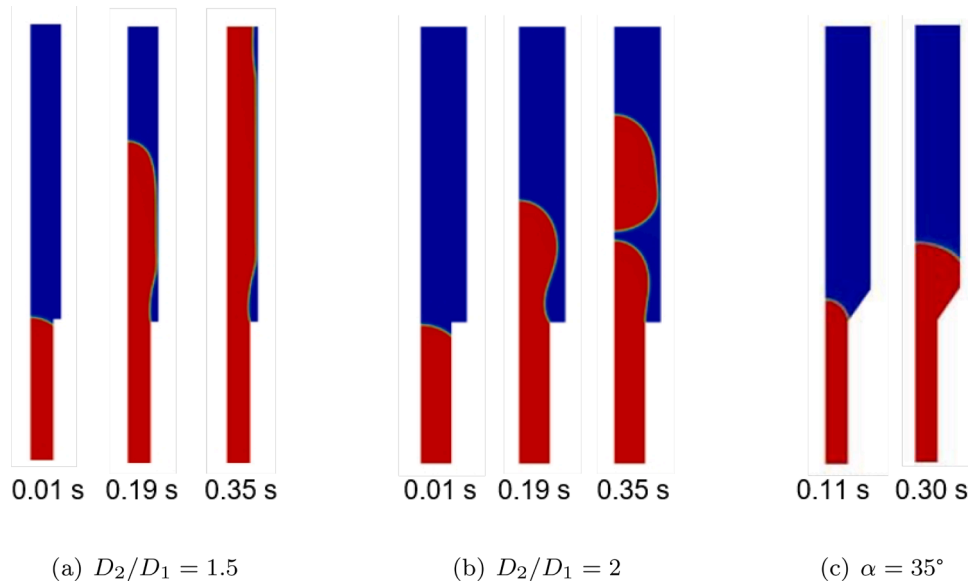


Fig. 8. CFD simulation of liquid back suction and bubble formation for different nozzle geometries. Reprinted by permission from Springer Nature Customer Service Centre GmbH: [40], Springer Nature.

the applied geometry, which is represented by two connected, concentric pipes with a defined diameter ratio.

Results indicate that a decreasing diameter ratio can delay bubble formation. Furthermore, the existence of a critical inclination angle is proposed, which impedes bubble formation, as shown in Fig. 8. The results show the strong effect of geometrical nozzle design on the two phase flow inside the nozzle during injection breaks.

3.2. Spray development and characterization

Spray development and its interaction with the flow field is decisive for the overall system performance. Spray penetration depends not only on geometrical injector characteristics and injection pressure, which determine the initial droplet size and velocity distribution. The density difference between gas and liquid as well as the ambient pressure further affect the penetration depth [42–44]. The most relevant parameter is the relative velocity of the droplets. For SCR application, studies focus on scenarios of droplets accelerated by the gas flow, as the injection velocity is smaller than the gas velocity. For passenger cars and trucks, exhaust gas velocities range from 5 to 100ms⁻¹ and injection velocities from 5 to 25ms⁻¹ [45]. For given primary UWS spray characteristics, the effect of relative velocity was investigated by altering the gas flow rate [30,33,46]. High gas flow rates promote entrainment of small drops and decrease spray density, which affects the extent and characteristics of spray impingement and reduces potential film formation [46].

Spiteri and Dimopoulos Eggenschwiler [30] study injection and spray development in a hot gas flow rig with a cross section of 80 x 80mm using optical imaging techniques, such as shadow imaging, PIV and Mie scattering. A commercial 6-hole full cone injector is used. Results show that the spray tip penetration velocity and the spray cone angle are independent from the gas flow conditions. Image intensity analysis is applied to investigate spray density and contours. The spray is described to consist of a dense core region surrounded by a peripheral region, which increases downstream and contains entrained droplets. The injected mass in the spray core is likely to impinge on the wall for all tested conditions [30]. Fig. 9 shows results of the image intensity analysis for sprays at different gas flow momentums (a) and a comparison of UWS and water spray behavior (b).

The described spray structure is observed both for high and low gas flow momentum. The low flow momentum spray contours strongly differ from the high flow momentum cases. The low flow momentum

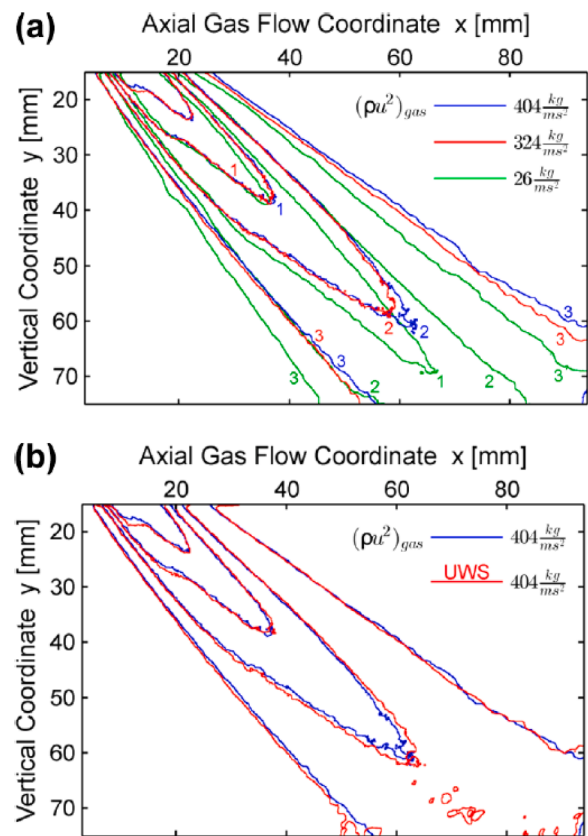


Fig. 9. (a) Characteristic image intensity isocontours for sprays at different gas flow momentums $(\rho u^2)_{gas}$: 1, high-density contours; 2, intermediate contours; 3, low-intensity outer contours. (b) Comparative image intensity isocontours for water and UWS spray at identical gas flow momentums. Reprinted with permission from [30]. Copyright (2020) American Chemical Society.

spray is less deflected and shows a larger core region due to less entrainment. A comparison of UWS and water sprays shows no significant difference in the spray structure at the same operating conditions.

Shadow images of spray penetration at different gas flow conditions

are given in Fig. 10. Liao et al. [31] perform a comprehensive analysis of the spray behavior under exhaust flow conditions using non-intrusive optical techniques. The commercial 3-hole injector is mounted 50° to the gas flow direction and operated at 9 bar. The spray cone deflection due to different gas flow velocities is negligible. However, increased entrainment can be observed for high gas flows. Furthermore, an increase in gas temperature is shown to decrease spray impingement. Note that, in this case, the gas velocity is affected by gas temperature due to the change in density, while the mass flow is kept constant.

Postrioni et al. [33] study the effect of the gas flow conditions on spray characteristics by PDA. Fig. 11 presents results for the mean velocity and the Sauter mean diameter of the droplets in dependence on gas temperature.

The increase in velocity for higher gas temperatures is clearly shown. Furthermore, the effect of enhanced evaporation on the droplet size is shown by a decrease in droplet size. For a constant relative velocity, a change in gas temperature was observed to hardly influence spray propagation [46]. In contrast to the gas temperature, van Vuuren et al. [47] found that the UWS liquid temperature drastically affects spray quality, as high temperatures were found to enhance the level of atomization. Experiments were performed from room temperature to boiling temperature by pre-heating the injected solution. Temperature changes affect viscosity and surface tension of the liquid. The effect of liquid properties on the atomization quality has been elucidated in numerous works, i. e. [48–51]. The relation of viscous to surface tension and inertial forces is generally expressed by the Ohnesorge number, including the liquids dynamic viscosity η , density ρ and surface tension σ as well as a characteristic length scale L .

$$Oh = \frac{\eta}{\sqrt{\rho\sigma L}} = \frac{\sqrt{We}}{Re} \quad (3.1)$$

For UWS injection, surfactant addition was studied and showed improved breakup characteristics and a decrease of the droplet size distribution width due to lowered surface tension [52].

Note, that all studies presented here rely on different flow setups and injection systems. Therefore, comparability is only partially ensured. Non-invasive, representative measurements of spray characteristics in hot flow environment have remained a challenging task. Establishment of good spray quality reduces the risk of subsequent droplet impingement, film formation and deposit build-up, which will be discussed in the next sections.

4. Droplet evaporation and gas phase decomposition

Efficient evaporation of the atomized liquid is required for appropriate conversion of urea to ammonia and a homogeneous reducing agent distribution. Furthermore, rapid evaporation of the droplets prevents liquid/wall contact and resulting film and deposit formation. Subsequent reactions in the gas phase determine the gas composition and relevant species ratios entering the SCR catalyst. For an optimized NO_x removal at the catalyst, uniform distributions as well as NO/NO_2 and NH_3/NO_x ratios of unity are desired for the fast SCR reaction. The NO/NO_2 ratio entering the SCR mixing section is affected by the DOC positioned upstream the SCR system responsible for the oxidation of unburned hydrocarbons, CO and NO. For avoidance of ammonia slip, efficient evaporation and conversion of UWS to ammonia is required to reach the desired NH_3/NO_x ratio while dosing the stoichiometric amount of the solution.

Complete evaporation of the spray requires a sufficient temperature and residence time in the mixing section. Static mixing devices are commonly used for short mixing length for secondary atomization of the spray, as it will be discussed in Section 7. Lower gas velocities were found to increase the spray evaporation efficiency due to increased droplet residence time [53]. However, for a constant residence time, a rise in relative velocity increases evaporation efficiency as a result of stronger convection. It is assumed that, depending on spray characteristics, enrichment effects of the surrounding gas phase affect the evaporation efficiency, as dense droplet clusters may lead to a vapor saturated environment. For combustion applications, droplet cluster evaporation accompanied gas phase enrichment was studied experimentally and numerically [54–56]. The role of enrichment is not included in current SCR research and deserves detailed studies.

Droplet evaporation under hot flow conditions can be evaluated by optical measurements of droplet size as presented in the previous section. Generally, droplet evaporation is enhanced by high relative velocities and temperatures [17,33,34], see Fig. 11.

4.1. Evaporation kinetics

For a detailed analysis of evaporation kinetics, experiments and simulations are performed for single droplets. Evaporation of single UWS droplets is stated to follow three evaporation stages [57,58]. Musa et al. [57] suspended single UWS droplets on a thin quartz fiber in a heated, quiescent atmosphere, while monitoring the evaporation process by a camera. The droplet diameter is evaluated by image analysis. An example for characteristic droplet evaporation of UWS showing three stages compared to water is presented in Fig. 12.

In the first stage, evaporation behavior is similar to pure water and follows the D^2 -law. Here, the evaporation rate is expressed by the droplet volume decrease indicated by its squared diameter, which follows a linear decrease in time. The second stage is marked by a reduction of the evaporation rate. The extent of this rate decrease mainly depends on temperature affecting the increase of urea concentration and a

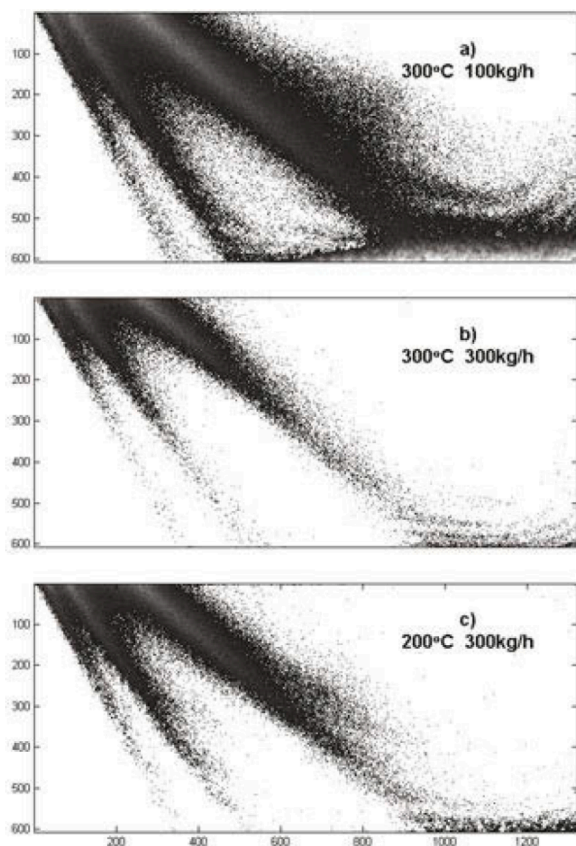


Fig. 10. Shadow images of spray penetration for different operating conditions. Given conditions result in gas flow velocities of 7, 21 and 17.5ms^{-1} (top to bottom). Reprinted by permission from Springer Nature Customer Service Centre GmbH: [31], Springer Nature.

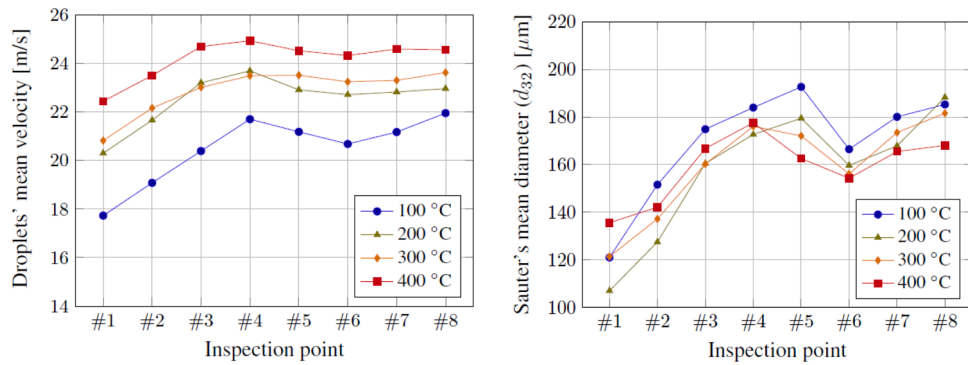


Fig. 11. PDA results for droplet size and velocity in dependence on gas temperature given for multiple measurement positions at a constant distance from the nozzle. #6 denotes the position in the injector axis. Measurements are performed for a 3-hole full cone injector. Reprinted from [33], Copyright (2020), with permission from Elsevier.

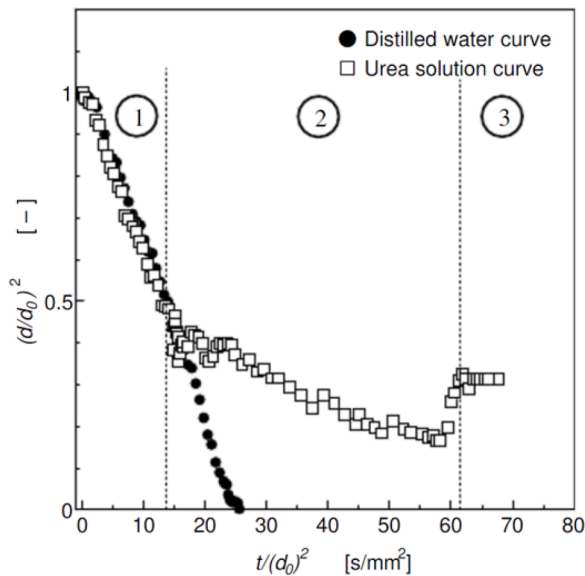


Fig. 12. Evaporation characteristics of millimetric water and 30 wt.-% urea solution droplets in a furnace at 200 °C [57].

decrease in saturation vapor pressure. In addition, boiling phenomena like bubble formation and expansion and crystallization of urea can be

observed leading to an unsteady development of $\left(\frac{d}{d_0}\right)^2$. It is assumed

that, depending on temperature, bubble formation and expansion is caused by gaseous reaction products of urea decomposition. Solidification of urea at the gas-liquid interface was partly observed to lead to microexplosions of droplets due to high pressures from boiling inside the liquid center [58]. The third stage represents the crystallization stage leading to complete solidification. Wei et al. [59] summarize the evaporation process of suspended UWS droplets in four stages, as they defined the initial temperature rise up to the water boiling point as a separate stage.

Theoretical models for the evaporation of multi-component droplets were developed in the context of spray drying [60,61]. These are capable to predict the diameter evolution as well as concentration and temperature profiles in the droplet. Existing evaporation models for urea water solution droplets confirm the different evaporation stages given in Fig. 12 [45,62]. Birkhold et al. [45] compared two droplet evaporation models applied to UWS droplets. The Rapid mixing (RM) model considers infinite high transport coefficients for the liquid phase leading to uniform temperature, concentration and liquid properties inside the droplet. The Diffusion limit (DL) model neglects internal convection and

considers only diffusive mass and energy transport in the liquid resulting in radial gradients of temperature, concentration and liquid properties. Results show that the RM model predicts UWS droplet evaporation well while being numerically more effective [45].

There are droplet evaporation models including instantaneous urea thermo-hydrolysis, which is considered as vaporization process [63–65]. In contrast, other models describe urea decomposition subsequent to evaporation using Arrhenius-type expressions [45]. Stein et al. [66] state, that evaporation and decomposition of UWS droplets can be reproduced more accurately by models accounting for a decomposition subsequent to water evaporation, instead of a direct decomposition at the gas-liquid interface. In order to limit computational effort for calculation of droplet evaporation and decomposition rates, reduced models have been proposed, which reproduce droplet evaporation and gas phase reactions in the temperature range relevant for SCR [66,67].

Habchi et al. [68] developed a model for evaporation and thermo-hydrolysis of urea droplets, which was validated by two experimental studies [58,59]. Results prove a good prediction of droplet temperature, evaporation rate and urea gasification over a wide temperature range. Thermal decomposition of urea is accounted for by implementation of a semi-detailed kinetic model comprising 12 reactions. An accurate prediction of urea decomposition is stated for low temperatures, whereas at high temperatures, the non-uniform droplet temperature resulting from bubble nucleation reduces prediction accuracy. Implementation of droplet evaporation and decomposition models to CFD models is discussed in Section 8.

4.2. Gas phase reactions

In addition to droplet evaporation and urea thermo-hydrolysis efficiency, gas phase reactions affect the gas composition at the catalyst inlet. These include the NO/NO₂ equilibrium, potential NO_x reduction and NH₃ oxidation and reactions of other exhaust components, such as CO and HCs. Homogeneous reactions of NO/NH₃ mixtures involving oxygen and water have been studied due to the application of thermal DeNO_x, known as Selective non-catalytic reduction (SNCR), for stationary post-combustion NO_x abatement. Gas phase NO_x reduction by ammonia works in a temperature range of 900 to 1400K. Therefore, experimental [69–71] and modeling [72–74] studies investigate the system particularly above 1000K. However, in the past years gas phase reactions have attracted increased attention in the context of lean-burn natural gas engines and, meanwhile, several studies on homogeneous reactions in gas mixtures at moderate temperature (400–1200K) are available. Significant homogeneous conversion of NO to NO₂ observed at moderate temperatures is assumed to affect catalytic NO_x reduction [75]. In gas mixtures relevant to lean-burn natural gas engines, a promotion of the homogeneous oxidation of light alkanes by NO_x was demonstrated, which can lead to formation of carcinogenic

formaldehyde [76]. Schmitt et al. [77] investigate the effect of different exhaust constituents on homogeneous NO_x conversion in the temperature range of 700 to 1200K. Increased reactivity is observed by addition of NO_2 and HC, such as CH_4 and C_2H_2 , lowering the NO conversion temperature by 200K. Furthermore, methane plays an important role in carbon and nitrogen chemistry, while the influence of CO on NO_x conversion is rather small. With regard to NO_x emission control of Diesel engines, gas phase reactions become increasingly relevant as modern SCR systems are to be developed for a pre-turbine position involving pressures of up to 5 bar and elevated temperatures for rapid light-off. At high temperatures and pressures, not only the NO_x conversion efficiency of SCR catalysts is improved, but also the catalyst performance is highly affected by gas phase reactions [78,79]. However, further studies are needed to understand the impact of gas phase reactions on the complete aftertreatment system.

Due to droplet evaporation and urea thermo-hydrolysis, gaseous intermediates of urea decomposition, particularly isocyanic acid HNCO, are relevant reactants in the gas phase. Gas phase reactions of isocyanic acid are part of several experimental and numerical studies related to combustion involving temperatures of 800 - 1500K [80–84]. It represents an important intermediate in SNCR systems. A recently developed mechanism for gas phase reactions at 900-1400K by Glarborg et al. [84] includes reactions of isocyanic acid with OH , O_2 , H_2O and itself. However, availability of suitable experimental data is limited. Few authors study homogeneous reactions involving isocyanic acid, particularly HNCO hydrolysis, under SCR relevant conditions. Urea thermolysis conversion increases with temperature and residence time. Koebel and Strutz [85] show that urea thermolysis is incomplete in the investigated temperature range of 255–440 °C for residence times of 0.09s. A considerable amount of urea can be detected at the entrance of the SCR catalyst. Complete decomposition of urea to ammonia and isocyanic acid was shown by Yim et al. [86] for temperatures above 350 °C and residence times above 0.1s. Isocyanic acid is observed to be highly stable in the gas phase, as similar concentrations of ammonia and isocyanic acid are detected [83,85]. Chen et al. [83] detect a NH_3 to HNCO ratio increasing from 1.2 to 1.7 with temperature. The maximum investigated temperature is 1273K. Fig. 13 shows results on the NH_3 to HNCO ratio in dependence on temperature and vapor concentration.

Isocyanic acid stability in the gas phase is a major concern in SCR aftertreatment engineering bearing the risk of harmful HNCO and NH_3 emissions. In case of incomplete thermolysis and hydrolysis, a considerable section of the catalyst is utilized to convert urea and isocyanic acid. Particularly short residence times, as present in modern, close-

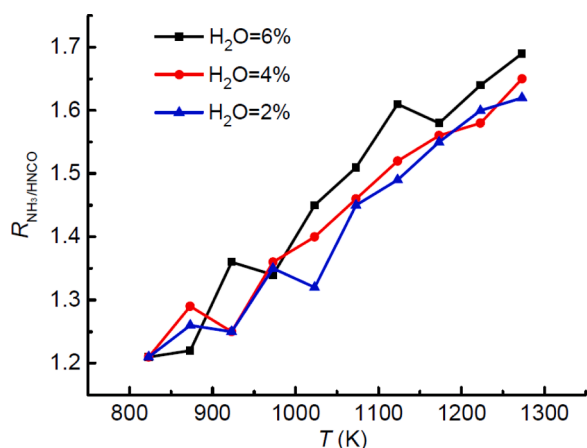


Fig. 13. NH_3 to HNCO ratio in dependence on temperature and vapor concentration. Inlet flow composed of urea with a volume fraction of 0.0004, 2–6% water vapor, 0% O_2 and N_2 balance; flow rate $1\text{ l}/\text{min}^{-1}$. Reprinted by permission from Springer Nature Customer Service Centre GmbH: [83], Springer Nature.

coupled systems, will contribute to the rising challenge of isocyanic acid conversion. In contrast to homogeneous reactions, catalytic isocyanic acid hydrolysis was extensively studied. Generally, isocyanic acid hydrolysis is found to be strongly accelerated by a catalyst [83,85–90]. Rapid hydrolysis was found for silica, alumina and titania [85] as well as for common SCR catalysts, such as VWT [91]. High conversions are achieved for catalytic HNCO hydrolysis even at high space velocities (10^6 h^{-1}) and low temperatures (150K). Particularly high rates for the hydrolysis are found on support materials, e.g. TiO_2 and Al_2O_3 , while the activity is slightly decreased by addition of vanadia, tungsta or CuO respectively [83,91]. The reaction is consistently stated to be limited by internal and external mass transfer [83,91,92]. A decrease of hydrolysis activity is observed for different catalysts by the competitive adsorption of HNCO and NH_3 and subsequent formation of ammonium nitrates [87, 92–94]. However, a re-activation of the catalyst can be achieved by high temperatures [93]. Recent studies propose a competition of HNCO hydrolysis with other reactions, such as oxidation by O_2 or NO_2 and a HNCO-SCR reaction via the formation of HONO [95]. HNCO is less active to interact with NO compared to NH_3 . However, in presence of NO_2 , the reactivity of HNCO acting as reducing agent was seen to be significantly promoted [94]. Kinetic models for the hydrolysis of HNCO over different catalysts were proposed [96,97]. Despite these achievements on catalytic hydrolysis of HNCO, experiments using SCR monoliths and engine test rig experiments considering conditions and catalysts close to application still reveal a significant slip of both ammonia and isocyanic acid [91,98,99]. Therefore, it is recommendable to further study homogeneous and catalytic isocyanic acid reactions, which strongly affect the efficiency of urea conversion and NO_x reduction.

Generally, droplet evaporation efficiency, thermal decomposition and gas phase reactions decide on the composition of the flow entering the SCR catalyst and the initial conditions of droplet impact in terms of momentum, temperature and urea concentration. Therefore, film and deposit formation as well as the overall system efficiency are affected.

5. Spray/wall interaction

In the combustion community and related industries, spray/wall interaction is important for both fuel injection in IC engines and exhaust gas aftertreatment systems. Particularly in ammonia SCR systems, spray/wall interaction is of growing interest [19,33,63,100–103]. Interaction of spray droplets with the tailpipe wall determines the extent of liquid/wall contact and film formation. Since the presence of a liquid film for a certain residence time inevitably results in the formation of solid deposits, spray/wall interaction and particularly droplet/wall interaction represents a critical phenomenon in the preparation of ammonia from UWS. Another important aspect of urea conversion efficiency is impingement on mixing elements, which can be utilized for secondary atomization and enhanced heat transfer to the liquid in case of short mixing lengths (see Section 7). Fundamental thermal and hydrodynamic phenomena during spray and single droplet impact and approaches to regime classification for modeling droplet/wall interaction are reviewed and discussed next.

5.1. Droplet/wall interaction regimes

The impact of single droplets on dry, solid targets motivated by different applications, has been investigated by numerous authors [104–118]. Particularly the continuing developments in high-speed imaging and post-processing techniques throughout the last decades have improved precision and quality of experimental investigations [119–122]. Despite these efforts, not all aspects of droplet/wall interaction including hydrodynamic and thermal effects are fully understood. Spreading, disintegration and formation of secondary droplets are significant hydrodynamic phenomena of droplet impingement.

Droplet/wall interaction is further affected by boiling characteristics, thermal breakup and the Leidenfrost effect [123]. Classification of droplet impact generally comprises thermal and hydrodynamic interaction regimes as indicated in Fig. 14.

In case of non-heated, dry impingement targets, the hydrodynamic outcome of droplet impact is assigned to *Deposition*, *Splash* and *Rebound* regimes [113,125,126]. Deposition means the adhesion of the total droplet mass on the surface resulting in a lense-shaped film dependent on the contact angle. Before reaching its final state, oscillating behavior of spreading and receding of the droplet can be observed. Splashing describes the atomization of the droplet and formation of secondary droplets due to high kinetic energy. Rebound at low wall temperatures marks a droplet reflection dominated by the liquid-solid contact angle. Deposition and rebound occur for low impact energies, whereas splashing is observed for high kinetic energy of the impinging droplet. Rioboo et al. [126] introduced a more detailed classification for kinetic disintegration differentiating between prompt splash (instantaneous disintegration) and corona splash (lamella breakup at maximum spreading length). Regime identification is based on the kinetic impact energy expressed by the droplet Weber number with droplet diameter d_0 and impact velocity u_0 , the liquid density ρ_l and surface tension σ .

$$We = \frac{\rho_l \cdot d_0 \cdot u_0^2}{\sigma} \quad (5.1)$$

Generally, a critical Weber number We_{cr} or a dimensionless splashing parameter $K = f(We, Re)$ incorporating Weber and Reynolds number is defined for regime distinction [127,128]. Different correlations for K can be found in literature in dependence on the experimental boundary conditions [129]. In case of heated targets, thermal interaction regimes, such as *Breakup* and *Rebound*, are considered in addition to hydrodynamics. Here, breakup describes a disintegration of the droplet by dominant thermal mechanisms, while rebound means a reflection of the total droplet. The Leidenfrost (LF) effect describes the formation of an insulating vapor layer between droplet and wall impeding liquid/wall contact. The vapor layer between droplet and wall strongly decreases heat transfer. In dependence on the boundary conditions, transition regimes, e.g. *Rebound with breakup* or *Boiling-induced breakup*, are introduced in literature for wall temperatures of $T_B < T_w < T_{LF}$ [113, 124,125,130,131]. Here, regime distinction is based on the dimensionless parameter T^* representing the ratio of wall temperature T_w and boiling temperature T_B of the liquid.

$$T^* = \frac{T_w}{T_B} \quad (5.2)$$

Moreover, the droplet temperature, heat capacity and the impact angle affect the spray/wall interaction. Thermophysical properties of the wall like thermal conductivity, heat capacity, roughness and

wettability are stated to influence the outcome of droplet impact [132].

Presented dimensionless parameters are used to set up comprehensive regime maps covering the most relevant thermal and hydrodynamic effects of droplet impingement. A qualitative regime map for single droplet impact on heated walls is shown in Fig. 14. It indicates a dependence of thermal boundaries, e.g. the wetting boundary defined by the Leidenfrost temperature, on the Weber number and vice versa, a dependence of the splash threshold on temperature. Regime classification and definition of regime boundaries is not straightforward and depends on various parameters, such as the liquid properties (vapor pressure, viscosity, surface tension), the droplet momentum (droplet diameter, velocity, impact angle) and the target surface characteristics (temperature, wettability, roughness). Droplet/wall interaction has been extensively studied for pure liquids, such as water and fuels, revealing important global dependencies [113,130,133–137]. These will be discussed in the following paragraphs before regime maps for UWS droplets are presented.

High initial droplet sizes and velocities promote spreading of the lamella up to lamella breakup (splash). In case of cold targets, surface wettability (θ) and roughness (R_a) play a major role for impingement dynamics. Small contact angles support intense lamella spreading and kinetic disintegration, whereas increased surface roughness diminishes spreading and induces disintegration at decreased velocities. Similar effects are promoted by liquid property changes to higher surface tension and viscosity [107].

Lamella breakup is promoted by instabilities and bubble nucleation induced by heat transfer from hot surfaces. Bubble nucleation site density is increased by surface roughness [104]. The *wetting boundary* separating wetting and non-wetting regimes depends on the liquid properties and a critical wall temperature, which is directly correlated to the Leidenfrost temperature T_{LF} [138]. Existing literature is contradictory concerning the dependencies of different parameters on the dynamic Leidenfrost temperature. Several authors have studied the effect of impact velocity [107,119,139,140], droplet size [123,141,142] and impact angle [143,144] on the Leidenfrost temperature. However, contrary trends are observed.

5.2. UWS droplet impingement

Concerning real applications, there is a strong need for research on single droplet impingement of solutions, such as UWS. Apart from exhaust after treatment, this is relevant for other technical applications including general heat transfer [145,146] and fire suppression [147]. The solute is observed to increase heat transfer resistance and decrease the vapor pressure [147,148]. Bubble formation and breakup are intensified by the solute and a foaming behavior is recognized [131,135, 148,149]. In case of thermal decomposition, increased gas bubble formation is seen to enhance boiling and droplet disintegration [148]. Solid residues resulting from evaporation of the solution are assumed to alter the subsequent collision dynamics [147].

For the application of SCR systems and the inherent risk of liquid/wall contact from UWS injection, droplet impact behavior of UWS is decisive. Several studies propose regime maps and droplet/wall interaction models for UWS in particular. Birkhold [17] investigated the impact of UWS droplet chains featuring diameters ranging from 90 to 180 μm and impact velocities of 5 to 20 ms^{-1} . High impact frequencies of the droplet generator of up to 10000 Hz complicated the visual analysis of image data and the identification of respective interaction regimes. Corresponding to the determined wetting boundary, a Leidenfrost temperature of 243 $^\circ\text{C}$ was calculated. [17]

Börnhorst and Deutschmann [102] investigated the impact of single UWS droplets in dependence on droplet momentum and target temperature. Droplet impact was classified to the regimes *Deposition*, *Splash*, *Boiling-induced Breakup*, *Rebound with Breakup* and *Total Rebound*. Characteristic impingement behavior for different regimes is illustrated in Fig. 15.

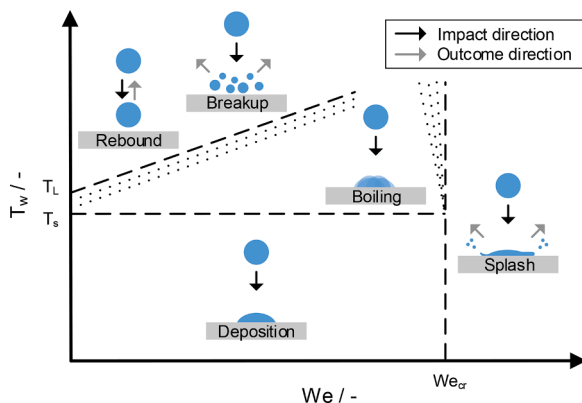


Fig. 14. Qualitative regime map for single droplet impingement on heated walls dependent on dimensionless numbers, adapted from [124].

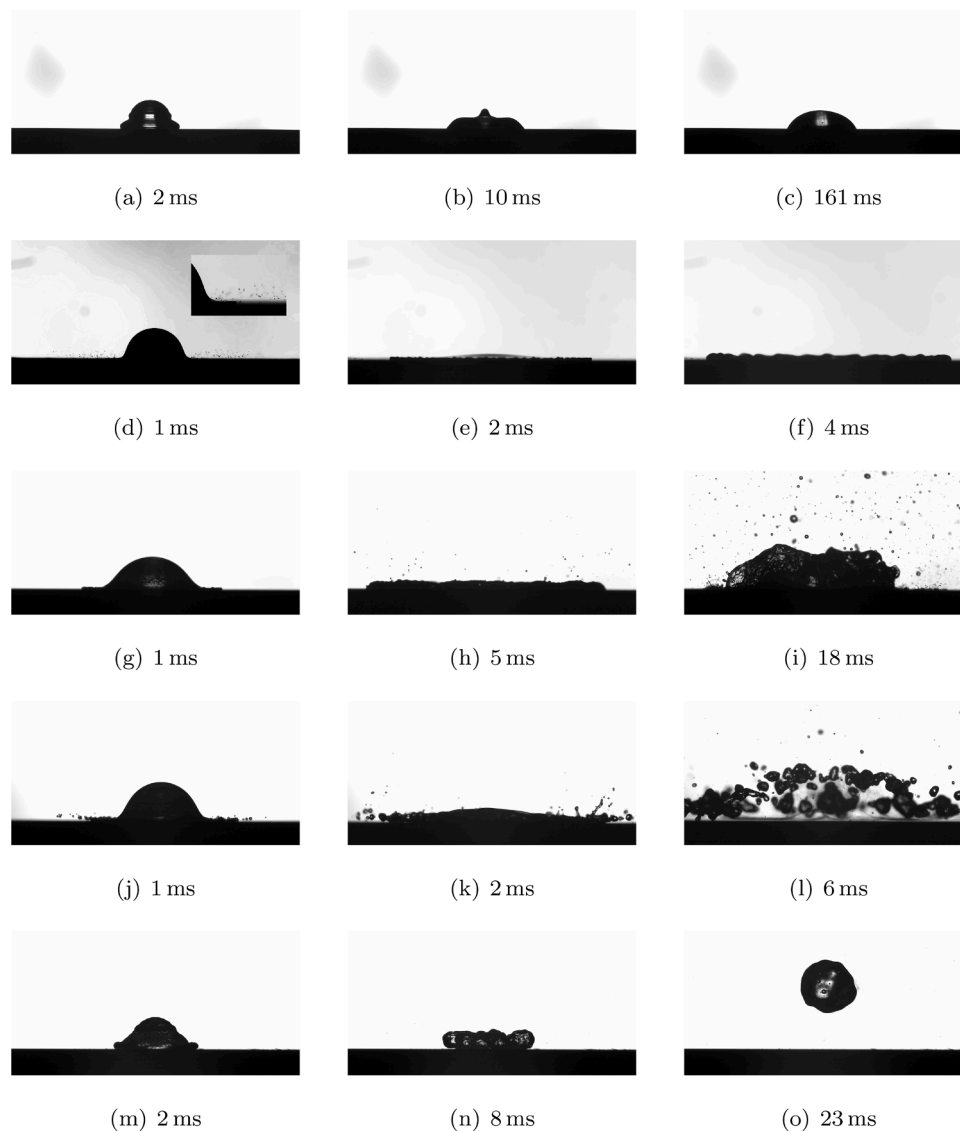


Fig. 15. Characteristic behavior of UWS droplet impact for respective regimes: a-c) Deposition, d-f) Splash, g-i) Boiling-induced Breakup, j-l) Rebound with Breakup m-o) Total Rebound. Time specification indicates time after impact. [150]

Further studies involve a variation in the concentration of the solution and modifications of the target surface. Here, millimetric droplets (2-3mm) with velocities of $1-4\text{ms}^{-1}$ are used for a detailed observation of the phenomena. Results show a strong effect of dissolved urea in comparison to pure water. Dissolved urea promotes droplet breakup processes at higher temperatures due to enhanced bubble nucleation and formation of gaseous decomposition products. However, an increase of urea concentration to 40wt.% is not observed to shift regime boundaries significantly in the applied parameter range. Using an aluminum target, the Leidenfrost temperature is slightly increased from $T_{LF} = 198^\circ\text{C}$ for 32.5wt.% urea to $T_{LF} = 204^\circ\text{C}$ for 40wt.% urea. These values are significantly lower compared to Leidenfrost temperatures measured by Birkhold [17]. Due to the different experimental conditions, particularly droplet size and velocity, results are only partially comparable. [150]

Quissek et al. [103] set up a regime map for UWS based on inclined impact experiments with $300\mu\text{m}$ droplets of $1-8\text{ms}^{-1}$ velocities. Weber number dependent Leidenfrost temperatures of 280 to 310°C are determined. Again, different experimental boundary conditions and the investigated parameter range limit the comparability and general validity of the regime map and characteristic temperatures.

Presented studies do not investigate the effect of target material or surface properties on droplet impingement. Aluminum and stainless steel targets of identical roughness were shown to result in similar regime maps [150]. However, most studies do not consider or give information on the impingement target properties. Bernardin and Mudawar [106] study the effects of surface properties on the Leidenfrost temperature by sessile drop evaporation experiments. Results show that the Leidenfrost temperature is relatively insensitive to wetting conditions of the surface and that increased roughness could lift the wetting boundary up to higher temperatures. Recent studies have shown that surface roughness plays a role for impingement hydrodynamics and can significantly shift the regime boundaries. Fig. 16 shows a regime map for droplet/wall interaction for a rough, porous stainless steel surface compared to a smooth, non-porous reference.

A strong effect is shown on the splashing boundary, which is shifted to lower K values for the rough sample. Droplet rebound by the Leidenfrost effect is shifted to higher temperatures. It is assumed, that vapor can escape through the pores of the target impeding the formation of a stable vapor layer. More detailed investigations are necessary to include the effect of rough or porous surfaces to the regime classification. However, these findings indicate the relevance of surface

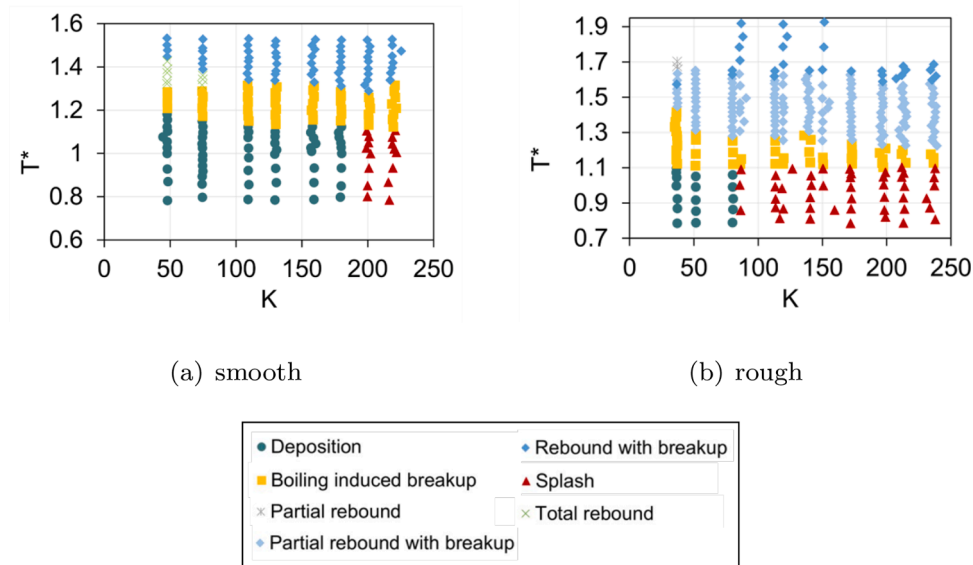


Fig. 16. Experimentally determined regime maps for UWS on a smooth ($R_a = 0.6\mu\text{m}$) and a rough ($R_a = 19.7\mu\text{m}$), porous (43% porosity, $60\mu\text{m}$ mean pore size) stainless steel surface. [276].

properties on the impingement dynamics. The comparison or use of existing regime data e. g. for modeling purposes should be accompanied by a careful analysis of the suitability according to the experimental boundary conditions including surface properties.

5.3. Models for UWS impingement

Spray impact modeling is relevant to many technical applications and has been extensively studied during the past decades. Although single droplet impingement is understood well, the transfer of the results to spray impact models is still an active field of research. Large effort has been put in understanding and modeling multiple droplet interaction [129,152–156]. Many spray impact models rely on single droplet data incorporated to a statistical approach resulting in a superposition of single impact events [132,157–159]. Another approach is the formulation of empirical correlations based on a high number of spray impingement experiments and statistical data analysis [156,160]. The remaining challenge is a reliable prediction of the deposited liquid mass fraction and the characteristics of secondary droplets over a wide

parameter range [129,161].

For UWS, spray impact models are generally based on experimentally determined regime maps implemented as sub-models in CFD codes for the prediction of film and secondary droplet formation. Here, characteristic data of the impacting droplet, the target surface and the environment serve as model input. Depending on the detected regime for this input, number and size of the secondary droplets, velocity components and droplet mass fractions are calculated by statistical functions. Research on spray/wall and spray/film interaction is mainly found in the context of spray cooling [129,161–163] and fuel impingement [159,164–166]. For simulation of spray/wall interaction inside of SCR systems, many studies rely on a model proposed by Kuhnke [132]. From single droplet experiments using isoctane, sodium chloride ethanol solution and glycerol water mixtures a regime map comprising deposition, splash, rebound and breakup was derived based on the parameters K and T^* . The wetting boundary is defined as $T_{cr}^* = 1.1$. Droplets impinging on a wall below this temperature deposit or splash leading to wall film formation, whereas droplets hitting the wall above this temperature are reflected by the Leidenfrost phenomenon or

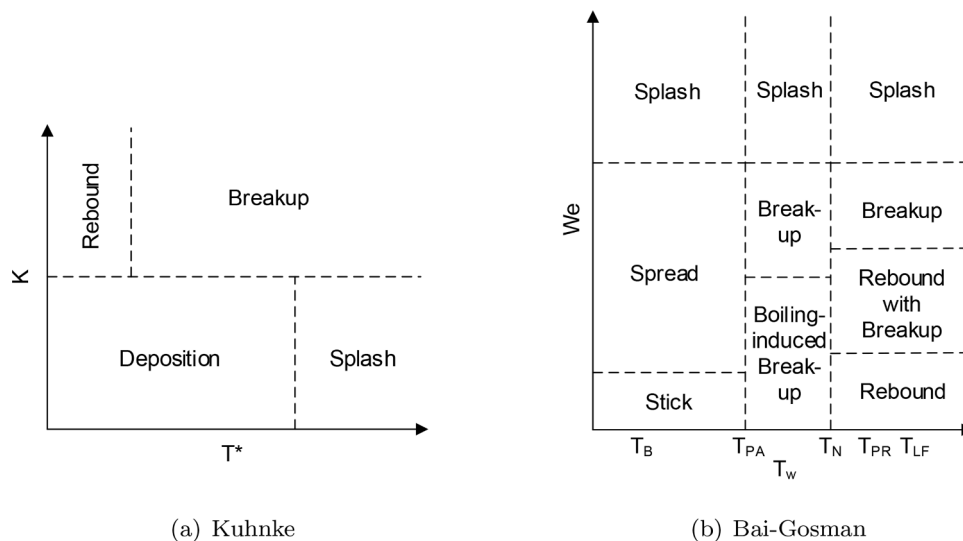


Fig. 17. Qualitative regime maps for droplet impingement on dry walls correlating to mathematical models from literature [125,132].

disintegrate thermally. The underlying regime map is shown qualitatively in Fig. 17 (a).

The Kuhnke model was applied in simulations by Birkhold et al. [45] and adapted in terms of the wetting boundary due to different physical properties of UWS compared to the model fluids. Based on the work of Kuhnke [132], a spray/wall interaction regime map for UWS was proposed. A more sophisticated model for spray/wall interaction was proposed by Bai and Gosman [125]. As this model was intended for simulation of Diesel impingement, it is based on impact data from hydrocarbon sprays. In addition, literature data on water spray impingement is included. The model provides regime classifications and calculations of respective post-impingement data for dry and wetted walls in dependence on the droplet Weber number, the droplet Laplace number $La = \frac{\sigma \rho_l d_0}{\eta_l^2}$ and the wall temperature. Seven different regimes are proposed with respective thermal and kinetic boundaries. Kinetic boundaries are deduced from literature correlations for dry and wetted walls. Thermal boundaries are defined by a *pure adhesion temperature* T_{PA} , which lies above the boiling temperature, the Nukiyama temperature T_N marking the maximum droplet evaporation rate and a *pure rebound temperature*, which is below Leidenfrost temperature. An overview on regimes and boundaries of the Bai-Gosman-model is given in Fig. 17 (b). Garcia Rosa et al. [167] present another approach to model spray/wall interaction. The model consists of statistical correlations and takes the most relevant impact parameters and physical properties into account. The same dimensionless numbers K and T^* are applied for regime classification. Other studies rely on spray/wall impingement models proposed by Stanton and Rutland [165] and O'Rourke and Amsden [168]. O'Rourke and Amsden [168] include the initial film thickness and boundary layer thickness to the dimensionless kinetic parameter E used for setting up the regime maps.

Bai-Gosman wall impingement was applied and adapted by Smith et al. [169]. The model is calibrated based on measurements of original and post-impingement spray characteristics inside a real-scale exhaust gas system including mixing geometries. CFD simulations are found to be predictive for the applied range of operating conditions. Measured ammonia distributions are reproduced qualitatively by the proposed model.

Quissek et al. [103] extended the Bai-Gosman model based on experiments of UWS droplet impingement. For SCR relevant conditions, the regime *Thermal induced Breakup* was added, describing the impingement of droplets on a wall with $T_w > T_B$ forming a liquid film, which immediately starts boiling and produces a large number of secondary droplets. Experimentally obtained regime data was compared to existing literature maps for UWS droplets [45,102]. Results show that the different drop impact setups influence the obtained regime data and

are only partially consistent. The model adaptations were implemented into a CFD code and tested by simulation of an exhaust system. The experimentally established regime map and the adapted Bai-Gosman model are displayed in Fig. 18.

In a subsequent publication, Quissek et al. [170] particularly account for the co-existence of two or more regime characteristics for given boundary conditions. Based on visual analysis of droplet impact high-speed recordings, impingement characteristics are described by a set of four maps assigning mass fractions to the respective impact behavior. The four scenarios used are spread, splash, thermal induced breakup and rebound. The proposed model represents a promising attempt to reduce the shortcomings of fixed boundary models. However, no validation is presented. [170]

5.4. Spreading of impacting droplets

In addition to thermal and hydrodynamic outcomes of droplet impact, researchers are interested in the initial spreading behavior of UWS droplets. Spreading dynamics of impinging droplets are decisive for the extent of wetting and therefore affect deposit formation. Not only the final spreading radius, but also the maximum spreading extent reached during droplet deposition are crucial information of droplet/wall collision processes.

Droplet impact on a solid target results in rapid spreading in radial direction within several milliseconds. A lamella is formed and spreading finally stops reaching a maximum spreading radius before receding. The droplet volume adopts from a sphere to a disc-like shape. Spreading dynamics are dominated by the droplet inertia and further driven by capillary and viscous forces. These forces are quantified by the dimensionless numbers We and Re revealing the droplet inertia (d_0, u_0) and the liquid properties (ρ_l, η_l, σ) as most important influence factors [171].

A typical measure for quantification of wetting dynamics is the spreading factor β , which is defined as the ratio between the instantaneous diameter of the wetted circular base area of the droplet and the initial droplet diameter. Special focus is placed on the maximum spreading factor in literature and several correlations exist to predict β_{max} [172]. At present, no generally valid correlation exists, but the applicability of a model depends on the droplet impact parameters and wall properties. In spite of a large number of investigations using water and other model fluids to propose mentioned correlations, very few studies are found on the dynamic wetting behavior of a UWS droplet, directly relevant to the SCR application. In a recent study on spreading of single UWS droplets, two empirical correlations [173,174] were found to predict the maximum spreading radius for millimetric droplets reasonably well [175]. However, the study reveals limitations of literature correlations as their validity is limited to certain parameter ranges.

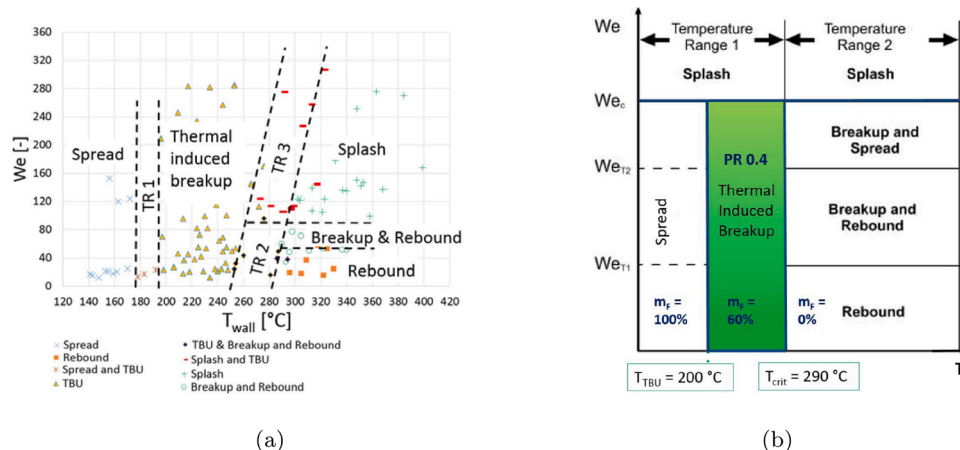


Fig. 18. Experimentally obtained regime map for UWS droplets (a) and adapted Bai-Gosman model (b) by Quissek et al. [103]. Republished with permission of SAE International from [103].

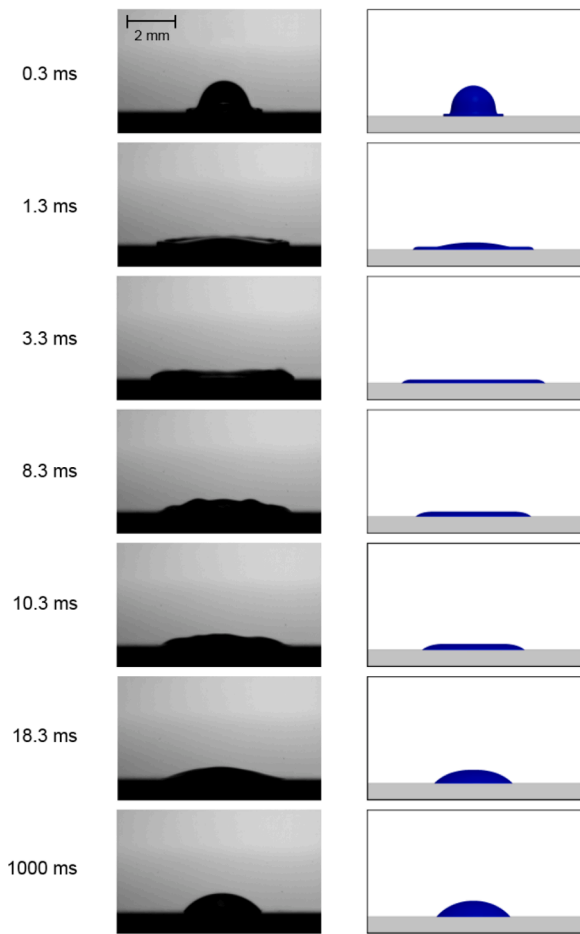
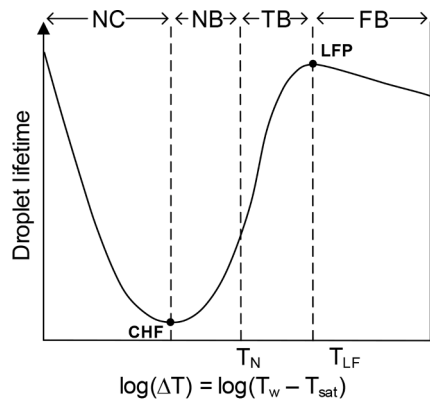


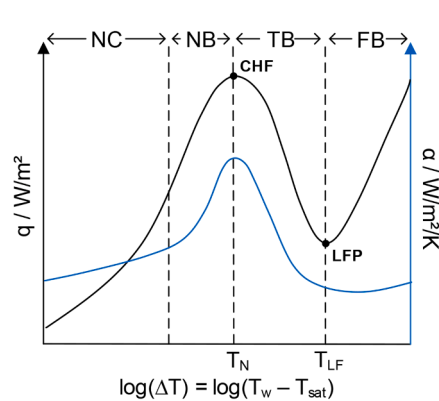
Fig. 19. Temporal evolution of droplet shapes in experiment (left column) and simulation (right column) for droplet diameter 1.95mm and impact velocity 1.95ms^{-1} [175].

Fig. 19 shows the temporal evolution of droplet shape during spreading obtained from experiments and CFD simulations.

Another recent study accounts for SCR relevant conditions in terms of droplet size and velocity [176]. The authors underline the importance of wettability on the impact dynamics and propose regime maps for droplet deposition and rebound at ambient, isothermal conditions.



(a)



(b)

Fig. 20. a) Qualitative droplet evaporation time for characteristic heat transfer regimes and b) Nukiyama boiling curve adapted from [178] showing the wall heat flux q and the heat transfer coefficient α over the temperature difference.

5.5. Spray/wall heat transfer

In SCR systems, heat transfer between wall and liquid is decisive in terms of film and deposit formation not only during droplet impingement but also for existing liquid films. The behavior of an impinging droplet is drastically affected by the temperature of the solid surface. In addition to hydrodynamic regimes presented in previous sections, liquid/wall interaction can be classified by heat transfer characteristics. For the droplet temperature $T_d < T_w$, T_d is increased by impingement heat transfer, while the surface is cooled. As local cooling reaches a critical surface temperature, wall wetting can be observed. Heat transfer between liquid and wall is dependent on the temperature difference, the contact area and the heat transfer coefficient and can be classified into four regimes. Regime definitions are deduced from the Nukiyama boiling curve, which was originally derived for pool boiling [177].

A common technique to measure heat transfer characteristics is an analysis of droplet lifetime, revealing the regime boundaries between natural convection (NC), nucleate boiling (NB), transition boiling (TB) and film boiling (FB). Fig. 20 (a) shows the qualitative evolution of droplet evaporation time as a function of wall superheat describing the excess temperature difference to the liquids boiling point T_B .

Further, a qualitative pool boiling curve gives the wall heat flux q and the heat transfer coefficient α as a function of wall superheat in Fig. 20 (b). Droplet evaporation time clearly shows an inverse correlation to wall temperature compared to wall heat flux, i. e. droplet life time decreases where the heat flux increases with temperature. At low temperatures, heat transferred from the surface is conducted through the liquid and dissipated at the gas-liquid interface by evaporation. This leads to a low heat transfer rate resulting in a long droplet evaporation time in the natural convection regime. With increasing surface temperature, nucleation sites are activated leading to gas bubble growth and rising. Bubble formation in the nucleate boiling regime results in enhanced convection and mixing inducing a dramatic increase of the heat transferred to the liquid and consequently, a decrease of evaporation time. With rising temperature, bubble formation and coalescence is enhanced until reaching a maximum heat flux, which simultaneously marks the minimum droplet lifetime. The upper limit is referred to as critical heat flux (CHF). A further increase in temperature results in the transition boiling regime. Here, an instable, insulating vapor layer develops between surface and liquid locally resulting in a chaotic variation between nucleate and film boiling. Transition boiling is characterized by a reduction of evaporation rate and an increase in droplet lifetime. The vapor layer substantially grows with rising temperature and further prevents liquid-solid contact until a stable vapor layer has developed. This temperature marks the Leidenfrost point (LFP), which corresponds

to the minimum heat flux and and the maximum droplet evaporation time. In the film boiling regime starting from the LFP, the liquid remains separated from the wall by the developed vapor layer. Heat is conducted through the vapor layer, which results in a strong decrease of heat transfer. Rising temperatures in the film boiling regime lead to a slight increase in heat transfer and reduction of droplet evaporation time. [106,178]

For the highly transient process of spray impingement, heat transfer and hydrodynamics are strongly affected by multiple droplet interaction [179]. Characteristics of spray impingement heat transfer are commonly described by the presented boiling curves [161,180–183]. Many studies on spray cooling exist, since it is an advantageous cooling method for technical applications in terms of spatial uniformity and both liquid and energy consumption. Measurements of boiling curves for impinging sprays reveal the temperature dependent heat transfer rate, the critical heat flux (CHF) and the Leidenfrost temperature. High surface temperatures result in increased heat transfer rates. Spray properties (droplet diameter and velocity) described by the Weber number, mass flux density and liquid properties were further identified as governing parameters for heat transfer [161]. Yao and Cox [182] defined spray-related parameters to correlate heat transfer efficiency for a wide range of boundary conditions, spray types and experimental methods. The spray Reynolds Re_{sp} and spray Weber number We_{sp} provide a more accurate reflection of the spray behavior since they include the spray mass flux G as described by Equations (5.3), (5.4) and (5.5).

$$Re_{sp} = \frac{Gd_{32}}{\eta_l} \quad (5.3)$$

$$We_{sp} = \frac{G^2 d_{32}}{\rho_l \sigma} \quad (5.4)$$

$$G = \frac{\dot{m}_{sp}}{A} [\text{kg s}^{-1} \text{m}^{-2}] \quad (5.5)$$

The spray mass flux describes the density of spray impact onto a surface and is found to be decisive for spray heat transfer efficiency. The use of We_{sp} is favored compared to We since the effect of normal impingement velocity on the heat transfer efficiency is not yet clarified [183]. An increase of the spray impact density leads to higher heat transfer efficiencies and strongly affects the boiling curve as it increases both Leidenfrost T_{LF} and Nukiyama temperature T_N and the respective heat fluxes q_{LF} and q_{CHF} [181].

Most studies discussed above account for the isothermal drop or spray impact. For the case of intermittent UWS injection and impingement under SCR conditions, transient heat transfer phenomena have to be accounted for, as droplet and wall temperature change during impact and transitions between different heat transfer regimes may occur [184]. Several studies address the transient nature of spray cooling processes [179,185,186], including the substrate conductivity [163,187], superposed air flow [162] and the transient droplet temperature [188,189]. Tenzer et al. [163] obtained transient boiling curves for water on a stainless steel target measuring the instantaneous, local heat flux in dependence on the spray properties. A theoretical model is provided, that predicts the substrate temperature over time in the film boiling regime taking into account thermal conduction in the substrate and the fluid temperature.

In the context of SCR systems, no detailed studies on transient heat transfer during impingement are available. The heat transfer of sessile urea water droplets was intensively studied under isothermal conditions. Evaporation behavior of millimetric UWS droplets was found to follow the four characteristic heat transfer regimes [31,57]. It is assumed, that urea decomposition and solid formation affect the evaporation behavior. Compared to another salt solution, a non-reproducible chaotic behavior during transition boiling was observed for UWS, which is attributed to gaseous by-product formation from urea decomposition [57]. A comparison of droplet lifetime for UWS with water and NaCl

solution is shown in Fig. 21. Thermal droplet breakup is stated favorable in terms of deposit formation, since it results in smaller secondary droplets experiencing film boiling.

For impinging urea water sprays, heat transfer was observed to follow a non-linear relation to the wall temperature, which is analogous to the heat transfer characteristics known from Nukiyama pool boiling [190]. In comparison to pure water sprays, regime boundaries and characteristic parameters, such as the Leidenfrost temperature and the temperature of CHF, are shifted to higher values for urea water solution [150,190]. With regard to SCR application, thermophysical material properties, surface wettability and roughness are identified as important parameters affecting heat transfer characteristics [190]. Schweigert et al. [191] investigate the effects of mentioned properties using high-speed imaging and IR thermography in parallel on a spray impingement setup without incident flow. Heat transfer is quantitatively described by introduction of an evaporated mass fraction, which is calculated from an energy balance based on the wall temperature data obtained by IR thermography during impingement. Results show that wettability effects are dominant over thermophysical material properties and roughness. Measured boiling curves exhibit a hysteresis due to a change in wettability resulting from the pre-conditioning of the material. Fig. 22 shows two example boiling curves measured for ferritic steel with (HTS) and without (LTS) thermal pre-conditioning. A clear hysteresis and shift of related heat transfer regimes is observed.

The effects of injection conditions, wall surface and material properties on the heat transfer characteristics of impinging urea water sprays can be utilized for a more targeted design of SCR systems in terms of impingement target coatings.

Spray/wall heat transfer of urea water solution in flow environment has not been studied in detail. A critical temperature for liquid film formation was found by Birkhold et al. [63], marking the surface temperature at which wetting is observed for the first time. Brack et al. [19] uses temperature measurements of the tailpipe wall as correlation data for a calculated spray surface load, which is directly related to an increased deposition risk. Characteristic heat transfer regimes of impinging urea water sprays in a flow channel have been observed by Liao et al. [192] for the first time. Temperature measurements of the outer flow channel walls and an inverse heat conduction model are used to calculate heat transfer data over time and correlate them to the operating conditions. The measurement duration covers multiple injection and impingement events and demonstrate the dynamic temperature response of the wall. Fig. 23 shows measured wall temperature data and the resulting spray heat flux calculated from the inverse heat conduction model.

Here, the highest heat flux values are determined for the third in-

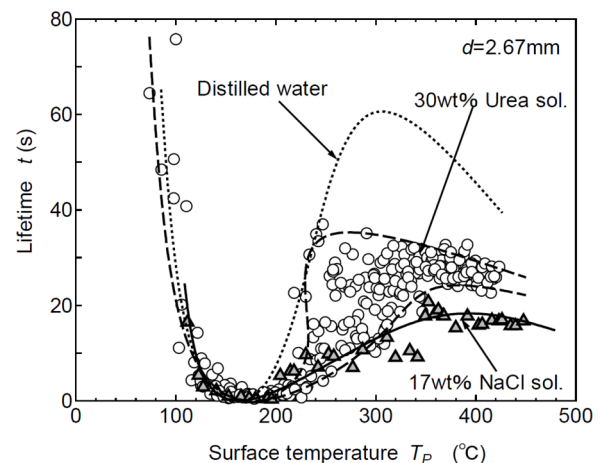


Fig. 21. Evaporation characteristics of UWS, distilled water and NaCl solution droplets. [57].

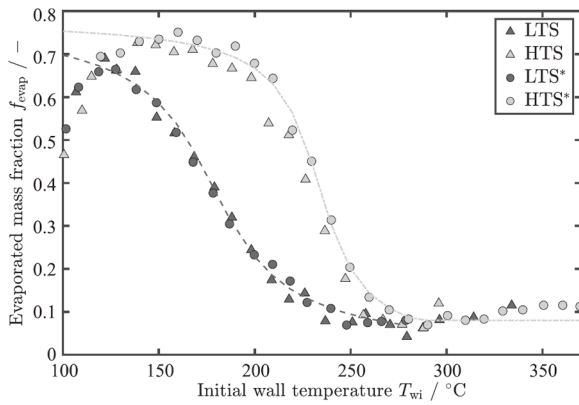


Fig. 22. Hysteresis effect in spray/wall impingement heat transfer (water on ferritic steel). LTS = low temperature state, HTS = high temperature state, *repeated measurements. Reprinted from [191], Copyright (2020), with permission from Elsevier.

jection event, where the critical heat flux regime is reached. Increasing gas flow rates are observed to decrease spray cooling due to enhanced spray entrainment. High gas temperatures lead to increased wall temperatures and, consequently, heat transfer rates, which can be related to different impact regimes [193]. Measurements enable the determination of characteristic parameters such as T_{LF} and q_{CHF} [192,193].

Characterization of liquid/wall heat transfer is substantial for modeling UWS spray impingement. While heat transfer is well described by analytical models for single droplet impact, models for multiple droplet and spray impact heat transfer are mostly empirical, particularly for wall wetting regimes. More details on available droplet and spray

heat transfer correlations and models can be found in recent reviews on spray cooling [138,161,194,195].

Studies on UWS impingement commonly apply the Rohsenow pool boiling correlation [196] to predict wall heat transfer in cases of wetting, which is the case for droplet impingement below T_{LF} and for an existing liquid film. For droplet impact at temperatures exceeding the Leidenfrost point, different approaches can be found to model impingement heat transfer. A commonly applied model for heat transfer in the film boiling regime is an approach proposed by Wruck [197], which implies calculation of effective contact time and area [24,45,53,198]. More precise modeling of impingement heat transfer was proposed by an adaption of the Wruck model [199]. Here, the correlation for the effective contact area by Akao et al. [200] is only applied for We numbers below the splashing threshold. Above, a We independent correlation is introduced.

Spray impingement and heat transfer decides on the extent of liquid film formation and evaporation, which is addressed in the next section.

6. Film and deposit formation

The formation of liquid film by spray impact and resulting solid residues is one of the main challenges of modern SCR systems. Depending on spray impingement hydrodynamics and heat transfer at the wall, the materials are cooled by periodic impact events. With decreasing temperature, liquid deposition is favored and results in the initiation and accumulation of a wall film. Surfaces prone to wetting by spray impact are mixer blades and tailpipe walls, particularly when located in pipe bends or in the spray cone range. Film formation and local cooling inevitably leads to urea precipitation and reaction to undesired by-products. Thus, formation of solid deposits from urea

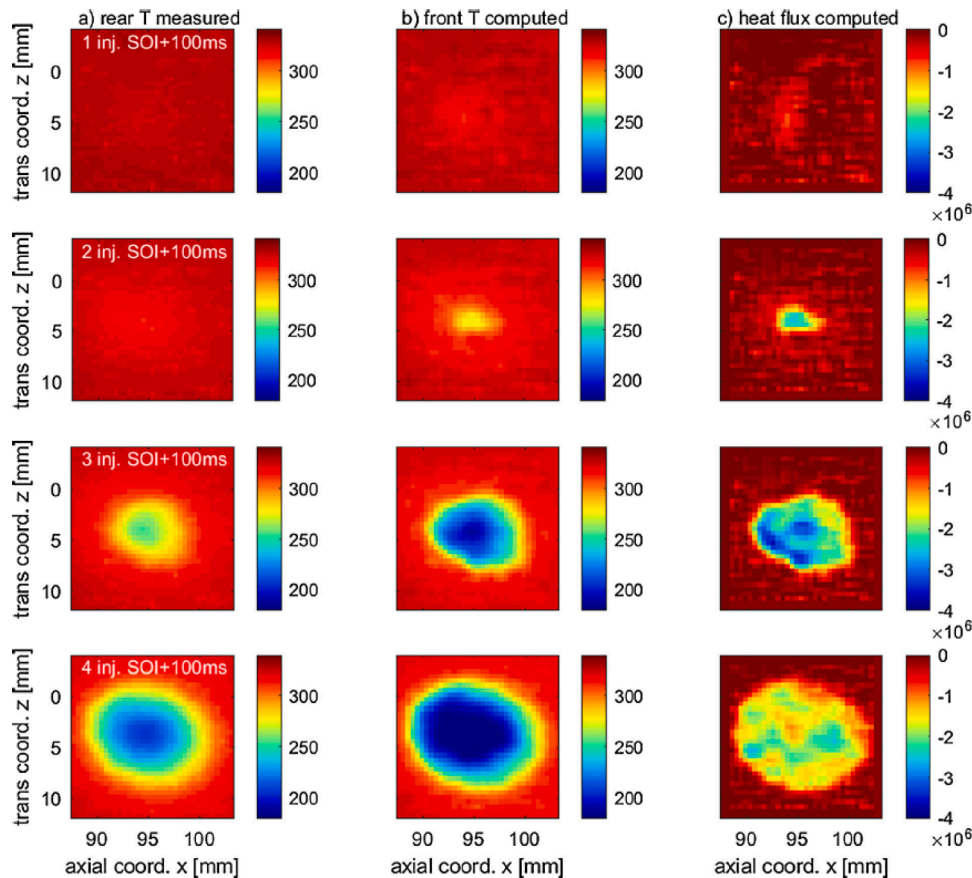


Fig. 23. Heat flux data calculated from an inverse heat conduction model based on temperature measurements at the rear side of a test rig for the first four injection events. Gas flow: 100kg^{-1} , 400°C ; injection parameters: 100ms, 2Hz. Reprinted from [192], Copyright (2020), with permission from Elsevier.

decomposition is the undesirable result from liquid/wall contact. The liquid film mass, area and temperature as well as its residence time are decisive for the amount and composition of solid deposits [19]. The evolution of solid by-products follows the reaction kinetics of thermal urea decomposition. The following sections will discuss the formation of liquid films, evaporation and urea crystallization as well as its chemical decomposition leading to solid deposition.

6.1. Liquid film formation and evaporation

Initiation and accumulation of a liquid wall film in SCR systems is highly dependent on the hydrodynamics and transient heat transfer dynamics of the intermittent spray impact. Generally, liquid is deposited on the wall when the wall temperature lies beneath the wetting boundary, as explained in Section 5.1. For higher wall temperatures, spray impingement results in local cooling without wall wetting [201]. The wetting boundary is often referred to as critical wall temperature T_{cr} , marking the temperature of liquid film initiation. It is determined from a characteristic decrease of the wall cooling rate during wetting [17,150]. While heat transfer is low for non-wetting interaction regimes, heat transfer between wall and liquid is strongly increased by liquid-wall contact. Experiments on film formation at a hot gas test rig indicate a clear dependence of the wetting boundary on the experimental conditions [150]. In this case, a definition of the wetting boundary by the Leidenfrost temperature is not sufficient. Furthermore, the results show that wetting boundaries defined by single droplet experiments can not directly be transferred to spray experiments with smaller droplet sizes. In addition to differing droplet sizes, the wetting boundary for intermittent spray impact is dependent on the transient heat transfer dynamics between wall and liquid. [17,150]

Experimental investigation of the initiation and accumulation of liquid films under SCR conditions is challenging. Few studies give qualitative information on liquid films evolving from urea injection at different conditions [19,46,101,202,203]. Since the setups do not allow for a direct measurement, the film area is estimated by other parameters, e.g. the spray density distribution above the wall [46] or the calculated spray surface load [19]. The experimental results are used to validate CFD simulations of spray impingement and film formation. However, comparability of experimental and numerical data is limited, since direct measurements of the liquid film area and pathways are challenging. Furthermore, the mentioned studies do not consider measurements of the film thickness. Information on film thickness is usually derived from CFD simulations.

Detailed investigations on liquid film dynamics were performed by Grout et al. [18], who studied film formation experimentally at a test bench under realistic conditions offering optical access by the use of glass walls. A quantitative analysis of the liquid film area is conducted by backlight imaging. Liquid film initiation is observed after a characteristic time interval. High gas temperature and mass flow increase the characteristic onset of film formation, whereas high UWS mass flows decrease it. The authors differentiate between three regimes for liquid film: liquid accumulation, liquid film flow and liquid evaporation. The film area continuously increases during injection. After reaching a certain size, liquid film transport by shear stress is observed leading to decreased film thickness, which is promoted by film evaporation due to high gas temperatures [18]. Film movement was further observed by Liao et al. [204]. Here, momentum of spray impingement is identified as main cause for downstream liquid accumulation and resulting solid deposits.

Fig. 24 summarizes influencing factors on liquid film formation, transport and evaporation.

The turbulent flow field exerts shear stresses on the UWS liquid film. Pulsed injection leads to droplet impingement on the liquid film causing periodic motion on the one hand, temperature and concentration gradients on the other hand. For wall films, radial temperature gradients are intensified by low wall temperatures in contrast to the high gas

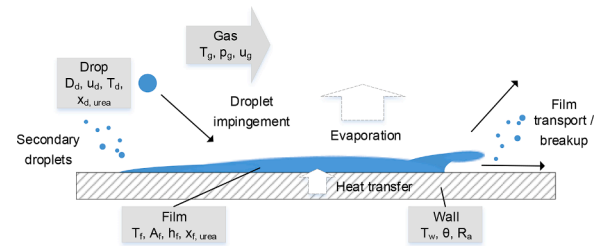


Fig. 24. Major physical phenomena governing film evaporation and flow.

temperature. As several studies show that no deposits are derived in the impingement area [204,205], the transport of accumulated liquid film can be seen as preliminary step of solid deposit formation.

Due to the liquid film exposition to high temperature and convective flow, evaporation occurs and urea can crystallize. Evaporation and crystallization of a two-component droplet or liquid film deposited on a hot surface is strongly dependent on the ambient temperature and flow. Fig. 25 schematically illustrates different evaporation phases by the example of a sessile droplet on a heated surface eventually leading to solidification.

The initial droplet volume is marked by t_0 . In the first phase, the droplet temperature rises at nearly constant composition due to the hot surface. The evaporation rate follows a linear relationship to the droplet temperature and is highest in the vicinity of the three-phase contact line. Reaching a constant temperature, the droplet volume decreases while the solute concentration increases. A higher solute concentration decreases the saturation vapor pressure of the solution and therefore affects the evaporation rate. Fig. 26 (a) shows the vapor pressure for saturated urea water solution as a function of temperature compared to pure water.

Vapor pressure data is calculated based on solubility data of urea depicted in 26 (b). At t_1 the saturation concentration of the solute is reached and the second evaporation phase starts. As evaporation continues with decreased rate, solute precipitation begins at the three-phase contact line and with further decreasing droplet volume, the solidification front moves to the center of the droplet until all liquid is evaporated at t_2 . The initial droplet heat-up is sometimes referred to as separate evaporation phase [209,210].

Schmid et al. [211] studied crystallization characteristics of sessile urea water solution droplets at sub-boiling temperatures and reported the previously described phases of evaporation. Crystal growth during evaporation is observed macroscopically in dependence on substrate surface temperature and wettability. For low temperatures and contact angles, slow crystallization is found to result in a fine white crystal structure, whereas high temperatures and hydrophobic surfaces promote rapid solidification leading to a smooth surface deposit while maintaining the initial droplet shape. Representative solid structures are shown in Fig. 27.

Thermographic imaging during evaporation clearly shows the

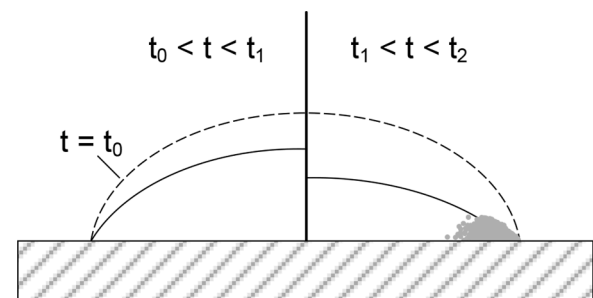


Fig. 25. Schematic evaporation phases of a two-component liquid droplet representing a film on a heated surface.

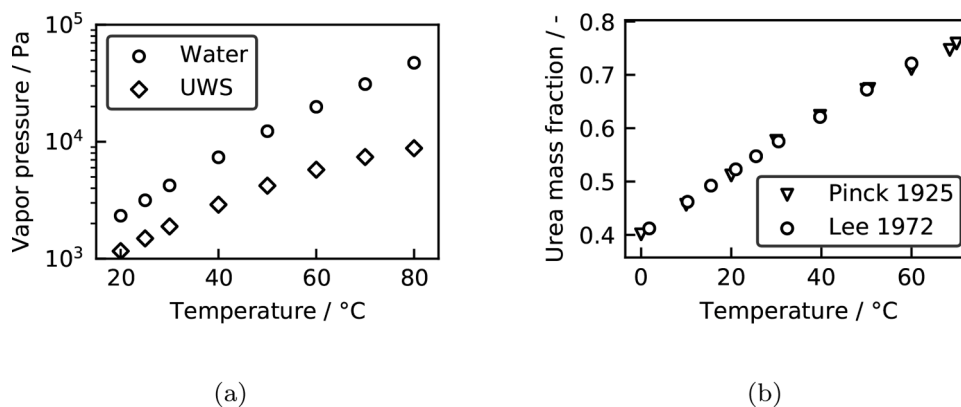


Fig. 26. (a) Saturation vapor pressure of urea water solution compared to pure water based on Wagner equation [206] and (b) solubility data of urea in water [207,208].

temperature rise along the three-phase contact line due to heat of solidification. Furthermore, the rate of solidification is observed to increase with rising temperature. This is explained by higher saturation concentrations of urea present in the crystallization phase causing rapid solidification. [211]

Based on experimental data and literature correlations, Bender et al. [212] propose a model for evaporation and crystallization of sessile UWS droplets. The model allows for resolution of temperature and concentration fields inside the evaporating droplet and accounts for the feedback of the evolved solids on the droplet. Fig. 28 shows a prediction of the temporal evolution of urea mass fraction inside an evaporating sessile droplet and indicates urea crystallization.

The simulations confirm the observations of the solid formation being initiated at the three-phase contact line forming ring-shaped deposits. A parametric study is performed to propose a correlation for the starting time of solids formation in dependence on droplet size, wall temperature and initial urea concentration. The solid growth rate is observed to increase with time after the start of crystallization. [212]

6.2. Kinetics of urea decomposition and by-product formation

Above 133 °C, crystalline urea melts and chemically decomposes. Apart from thermolysis and hydrolysis reactions forming the required reducing agent several side reactions may lead to formation of by-products of higher molecular weight, such as biuret, triuret, cyanuric acid, ammelide, ammeline or melamine [20]. By-product formation and their decomposition is mainly dependent on temperature. Table 1 shows data on the melting and decomposition temperatures of urea and relevant by-products.

The decomposition kinetics of urea and its by-products have been

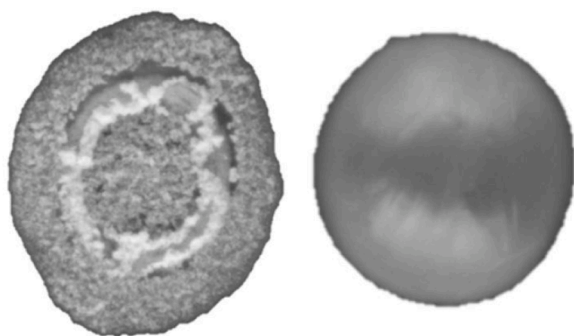


Fig. 27. Characteristic solid structures derived for slow (left) and rapid (right) solidification of a sessile UWS droplet. Reprinted from [211], Copyright (2020), with permission from Elsevier.

extensively studied by several groups [20–23,100,218–220]. Common experimental methods are thermogravimetric analysis (TGA), differential scanning calorimetry (DSC), high performance liquid chromatography (HPLC) and Fourier-transform infrared spectroscopy (FTIR).

A first detailed description of urea decomposition reactions was given by Schaber et al. [20] based on TGA, HPLC, FTIR and ammonium ion-selective electrode (ISE) experiments. Based on experimental and literature data, a reaction scheme of 23 reactions comprising urea and its by-products biuret, cyanuric acid, ammelide, ammeline and melamine was proposed. For urea decomposition at high temperatures, cyanate and cyanurate salts and cyanamide were identified as possible intermediates. Triuret reactions were not included to the reaction scheme. Four temperature regimes for urea decomposition were proposed. The first temperature regime comprises urea melting and vaporization from 133 °C followed by decomposition to ammonia and isocyanic acid. With increasing temperature up to 190 °C, biuret, cyanuric acid and ammelide are formed. The second temperature regime of 190–250 °C is assigned to biuret decomposition. Several side reactions produce cyanuric acid and ammelide. The authors observed formation of a sticky, solid matrix from the melt at 225 °C, which was attributed to ionic formations of different by-products. The temperature regime from 250 to 360 °C was dedicated to cyanuric acid sublimation and decomposition followed by decomposition of ammelide, ammeline and melamine in the fourth temperature regime starting at 360 °C. Complete decomposition of ammelide was observed for 600 °C, ammeline decomposition was seen complete at 700 °C. [20]

Eichelbaum et al. [22] derived a scheme of nine major reactions for urea decomposition from experimental investigations using simultaneous TGA and differential thermal analysis (DTA) measurements coupled with gas chromatography (GC)/mass spectrometry (MS) gas analysis. Reactions for decomposition of ammelide, ammeline and melamine were proposed and complete decomposition was measured for temperatures above 625 °C. However, the reaction scheme lacks in accurate description of relevant parallel and equilibrium reactions. Metal exchanged zeolites were shown to accelerate urea pyrolysis. Bernhard et al. [23] developed a more detailed reaction scheme based on flow reactor experiments and subsequent FTIR and HPLC analysis for gaseous and solid reaction products. The scheme including 15 decomposition reactions covers triuret production and decomposition as well as several equilibrium reactions. [23]

Fig. 29 demonstrates a characteristic mass loss during thermal decomposition of urea measured by TGA.

TGA results clearly demonstrate four characteristic mass loss stages attributed to the evolution and decomposition of typical urea by-products. These data are commonly used to investigate the decomposition behavior of urea and its by-products. When analyzing urea derived deposits, the extent of respective mass loss stages gives an indication of

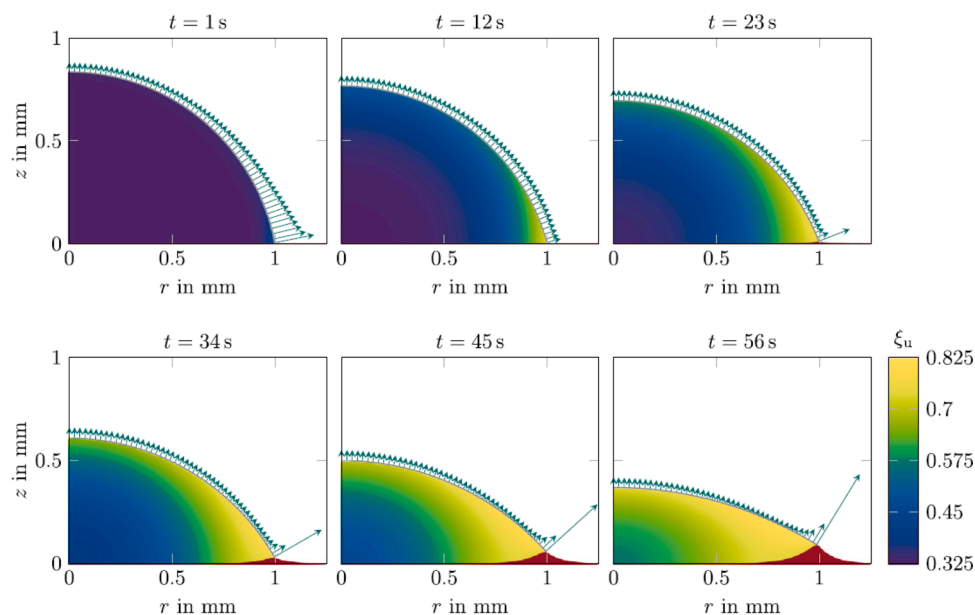


Fig. 28. Numerical results for the temporal evolution of the urea mass fraction inside an evaporating sessile drop and local evaporation rate. Solid formation is indicated in red. The initial temperature of gas and liquid is set to 25°C, the wall temperature to 65°C. Reprinted from [212], Copyright (2020), with permission from Elsevier. (For interpretation of the references to colour in this figure legend, the reader is referred to the web version of this article.)

Table 1

Physical properties of urea and relevant by-products * in water (20°C) ** decomposition prior to melting.

Component	Molecular formula	Molar mass gmol ⁻¹	Melting point °C	Decomp. point °C	Solubility* g ⁻¹	Ref.
Urea	CO(NH ₂) ₂	60.06	132.7	132.7	1079	[213]
Biuret	C ₂ H ₅ N ₃ O ₂	103.9	188–195	187	20	[214]
Triuret	C ₃ H ₆ N ₄ O ₃	146.11	n/a	233	n/a	[213]
Cyanuric acid	C ₃ N ₃ (OH) ₃	129.08	**	250	2	[20,213,215]
Ammelide	C ₃ H ₄ N ₄ O ₂	128.09	**	360	0	[20,216]
Ammeline	C ₃ H ₅ N ₅ O	127.11	**	360	trace	[20,216]
Melamine	C ₃ H ₆ N ₆	126.12	**	300	3.2	[217]

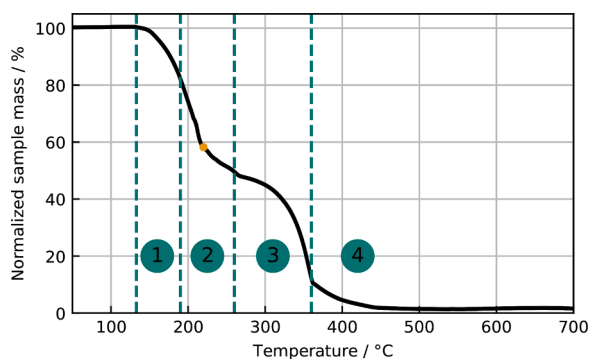


Fig. 29. Mass loss during thermal decomposition of urea measured by TGA with an initial sample mass of 60.3mg and a heating rate of 2K min⁻¹. Characteristic decomposition stages of urea are indicated as stated in literature [20, 22]. 1: urea decomposition, 2: biuret decomposition, 3: cyanuric acid decomposition, 4: ammelide and ammeline decomposition. Solidification (matrix) as mentioned by Schaber et al. [20] is indicated by the orange marker.

the sample composition. Moreover, TGA results deliver valuable data for kinetic reaction modeling.

Based on the experimental results given by Schaber et al. [20], Eichelbaum et al. [22] and Bernhard et al. [23] among others, numerous

authors have developed kinetic schemes for modeling urea decomposition, which has become of great interest in terms of predictive modeling and design of SCR systems. A first kinetic model describing evaporation and decomposition of UWS was proposed by Ebrahimian et al. [221]. The model includes urea thermolysis to ammonia and isocyanic acid, equilibrium reactions forming biuret and the subsequent reactions to cyanuric acid and ammelide. Ammelide decomposition to gaseous by-products is assumed.

Gan et al. [222] developed a semi-detailed kinetic model for urea decomposition based on the work of Schaber et al. [20] and Ebrahimian et al. [221]. The kinetic scheme contains 9 reactions and is applied together with a droplet evaporation model. The dependence of droplet diameter on evaporation time, relative gas velocity and gas temperature is presented. Temperature is identified as decisive factor for deposit yield. However, results deliver only a qualitative comparison of UWS droplet decomposition simulation with deposits derived at an SCR test rig. [222]

Brack et al. [100] proposed a kinetic model based on urea decomposition reactions given by Bernhard et al. [23]. TGA and HPLC experiments were used for detailed model validation. The model describes the production and decomposition reactions of the most important by-products and adequately maps the characteristic decomposition stages of urea. However, relevant physical and chemical processes are not considered. The conversion of biuret to a solid *biuret matrix* species is specified for temperatures around 220 °C. At this temperature,

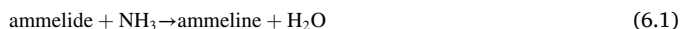
solidification of the melt was visually detected during the experiments, but no specific measurements or thermodynamic information are given. Ammelide decomposition is implemented as sublimation, while other high molecular weight by-products are not considered.

Fig. 30 a) gives an overview on the reactions included in the model.

Tischer et al. [223] present a revised kinetic scheme based on the model of Brack et al. [100] including thermodynamic considerations derived from TGA and differential scanning calorimetry (DSC) data. Experimental data and thermodynamic calculations reveal the presence of an eutectic mixture of urea and biuret, which can explain the phase change effects first observed by Schaber et al. [20]. The phase diagram of urea and biuret is given in Fig. 31.

The phase diagram reveals that biuret becomes liquid at 193 °C in case of a mixture of 67% biuret and 33% urea. By decomposition of urea with increasing temperatures, the amount of urea is decreased and biuret becomes solid again. Based on these data, solidification of biuret is initiated for temperatures above 210 °C before the actual melting point of biuret is reached at 233 °C. Including these effects, the proposed model (see Fig. 30b)) predicts urea decomposition well. However, due to a lack of thermodynamic data of biuret and triuret, not all relevant effects can be included. [223]

Most of the existing models cover urea decomposition until formation of ammelide or ammeline. In literature, various proposals for reaction pathways starting from ammelide at high temperatures are available [20,22,23,219]. Different authors propose amination reactions from ammelide to ammeline (6.1) and from ammeline to melamine (6.2) for temperatures above 250 °C [20,22,23].



In thermal decomposition experiments, ammelide and ammeline are found in the sample mixture up to temperatures of 600 °C and 700 °C respectively [20]. Eichelbaum et al. [22] describe a polymerization of melamine to melem at 500 °C and a subsequent decomposition of melem to (CN)₂ and HNCO for temperatures above 625 °C. Other works mention melon as high temperature product of urea decomposition. A recent study identifies the final pyrolysis products and proposes a kinetic model for urea decomposition over the entire temperature range relevant to SCR application [224]. Reaction kinetics and thermodynamic data of pyrolysis products like cyanamide, melamine, melon, graphitic carbon nitride and others are included to the model.

Literature emphasizes a strong effect of the experimental conditions on urea decomposition kinetics. The heating rate of the sample [20,218, 219] as well as the arrangement of the powder sample and different crucible geometries inside the setup [21,22,219] affect the decomposition behavior. Increased surface area of the sample is assumed to

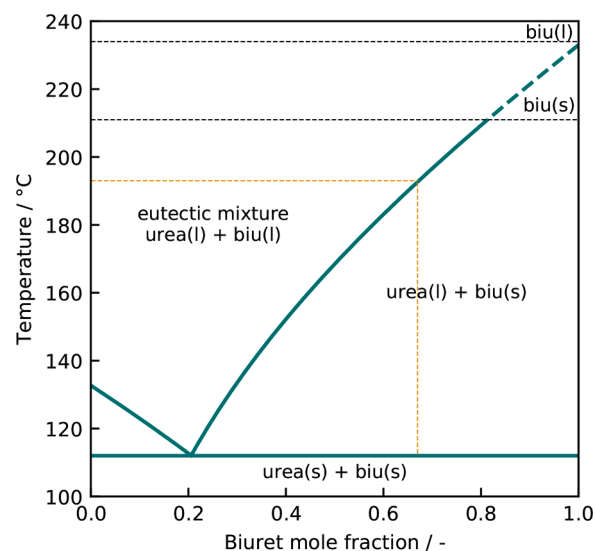
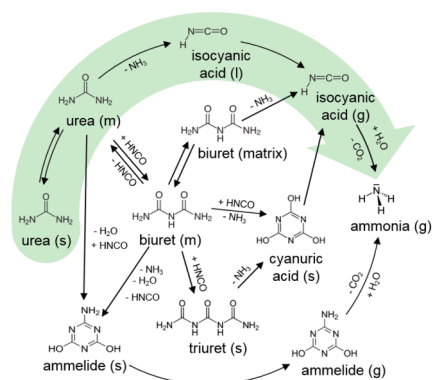
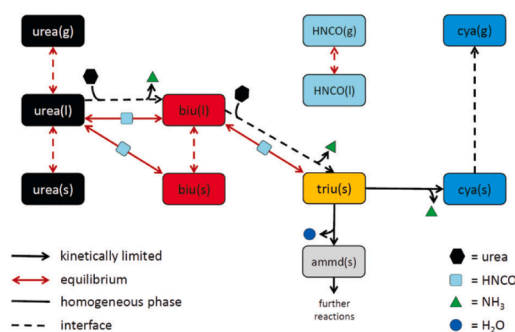


Fig. 31. Phase diagram of eutectic mixture of urea and biuret adapted from Tischer et al. [223]. The orange dotted lines indicate a composition of 67% biuret and 33% urea leading to melting of biuret.

accelerate mass transport of gaseous products at the sample surface and their removal as it was shown by using TGA crucibles of different base areas [22]. This leads to an increase of urea conversion and reduction of by-product formation. The same effect was observed in investigations on the thermal decomposition of urea and its by-products using impregnated monoliths in addition to cup geometries in a flow reactor [21]. Further studies on decomposition of urea in impregnated monoliths state that the presence of water in the gas phase decreases by-product formation due to isocyanic acid hydrolysis [23]. Generally, an accelerated decomposition of urea is observed on surfaces catalyzing the hydrolysis of isocyanic acid if water is present to a sufficient amount [22, 23,225]. Catalytic hydrolysis of isocyanic acid has been investigated experimentally by both kinetic measurements and diffuse reflectance infrared Fourier transform spectra (DRIFTS) studies [87,88,91, 226–228] and by density functional theory (DFT) calculations [89,90]. Regarding solid by-product formation from urea decomposition, positive effects of catalysts dedicated to isocyanic acid hydrolysis have been observed [22,23,64,220]. Formed deposits reveal similar compositions as compared to measurements without catalysts but the catalyst increases the decomposition rate. However, an aging effect of the decomposed products on the catalyst surface was observed [220]. Furthermore, it was found that urea itself can contribute to a direct reduction of NO in the presence of a catalyst [220]. As indicated above,



(a) Brack et al.



(b) Tischer et al.

Fig. 30. Reaction schemes used for kinetic modeling of urea decomposition. a) adapted from [100], b) [223] - published by the PCCP Owner Societies.

isocyanic acid production and its consumption by hydrolysis drastically influence the formation of by-products.

Fig. 32 shows thermogravimetric data on decomposition of pure urea samples with varying initial sample mass and crucible geometries.

The crucible geometries differ in diameter, as the plate features a 2.5 times larger diameter than the cylinder crucible. While maintaining identical initial sample mass, the use of the plate crucible reveals faster decomposition kinetics compared to the cylinder crucible. Furthermore, a higher residual mass is obtained for the plate geometry over 500 °C. By varying the initial sample mass using the cylinder crucible, faster decomposition is observed for the small initial mass. This clearly reveals the importance of the surface-to-volume ratio of the sample. Here, isocyanic acid release at the sample surface plays a major role since it is involved in the thermodynamic equilibrium between urea and biuret as well as between biuret and triuret. Results show that a high surface-to-volume ratio promotes urea decomposition as a result of the increased mass transport of gaseous products at the interface. The key role of isocyanic acid for ammonia preparation, deposit formation and SCR catalysis has often been underestimated in previous studies and will attract more focus of SCR related studies in the next years.

6.3. Deposit formation and characterization

Several studies address the formation of harmful solid deposits due to urea injection at realistic operating conditions using hot gas or engine test benches [19,202,205,229–232]. Deposits derived at different operating conditions are analyzed in terms of position, yield and composition by the analytical methods discussed above. Generally, a strong dependence on temperature, UWS dosing rate and spray impingement locations is found.

Brack et al. [19] propose a classification of operating regimes regarding deposit quantity based on experimental and numerical results. For wall temperatures below 150 °C, mainly crystalline urea is found in solid residues. At these temperatures, intense wall film formation bears the risk of liquid flowing into the SCR catalyst. Wall temperatures of 150 to 250 °C are stated as critical conditions inducing large quantities of deposits. Even a blockage of the pipe can be observed by massive solid formation (Fig. 33).

Moreover, existing deposits are found to act as flow barrier leading to film accumulation near the deposits. Based on their results, Brack et al. [19] regard temperatures above 250 °C as not critical in terms of deposit formation. Generally, a strong relation between wall wetting and solids formation is observed. Concerning deposit composition, a dependence on the liquid film thickness is proposed.

Smith et al. [202] focus on wetting and deposit formation on mixer blades. By optical analysis, two types of deposit growth are observed: *damming growth* by liquid film reaching existing deposits before solidification and *peripheral growth* describing solidification at the edge of existing deposits induced by capillary flow through the porous solid

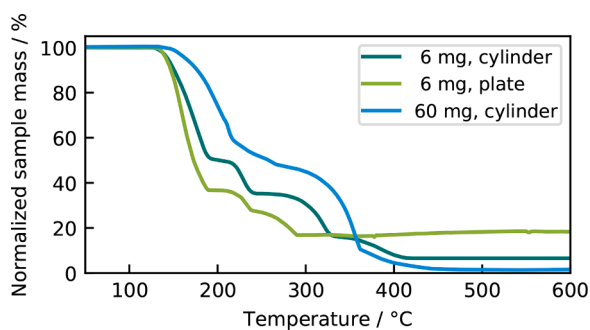


Fig. 32. Effect of experimental boundary conditions on urea thermal decomposition. Experiments are performed using different initial sample masses and cylinder types but an identical heating rate of 2K min⁻¹.

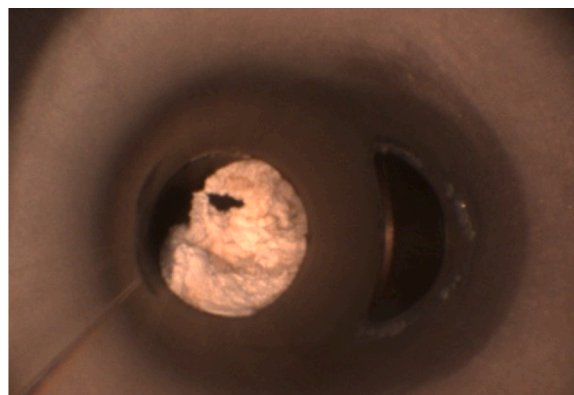


Fig. 33. Severe case of solid deposits formed from urea decomposition leading to pipe blockage. Courtesy of W. Brack, BMW Group, Munich, Germany.

structure. Liquid film pathways and deposit growth from liquid film on a mixer blade is demonstrated in Fig. 34.

Deposit formation is seen to be prevented at locations marked by continuous dilution of the liquid film due to the impinging solution or film transport. [202]

Chemical analysis of deposits is relevant to the identification of critical deposition regimes and to the development of regeneration strategies. Furthermore, it supports the development of models predicting deposit formation, which are essential in the design and optimization of SCR systems. Characteristic decomposition stages revealed by thermogravimetric analysis give a qualitative indication of the deposit composition as a function of temperature [202,230,231]. Few authors apply HPLC analysis for quantification of the deposits chemical composition [19,150,205,232]. Measurement accuracy of HPLC methods for analysis of urea deposits reaches from < 5 to 20% for different by-products. Fig. 35 shows HPLC analysis data of deposits derived in a hot gas test rig at different temperatures.

HPLC data are shown together with experimental and numerical

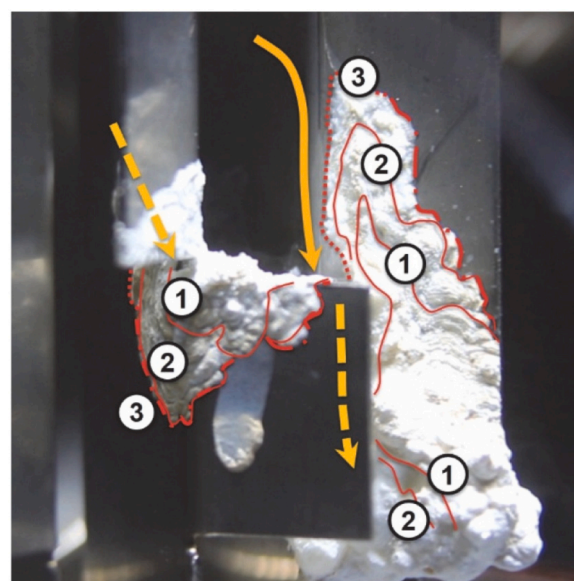


Fig. 34. Deposit growth on mixer blades in an engine test bench operated with 250°C gas temperature, 100kg h⁻¹ exhaust mass flow and an injection rate of 25mg s⁻¹. Yellow arrows indicate liquid film pathways (dashed, if hidden by blades). Dotted red lines: damming growth, dot-dashed red lines: peripheral growth, (1): 20 min, (2): 40 min, (3): 60 min. Republished with permission of SAE International from [202]. (For interpretation of the references to colour in this figure, the reader is referred to the web version of this article.)

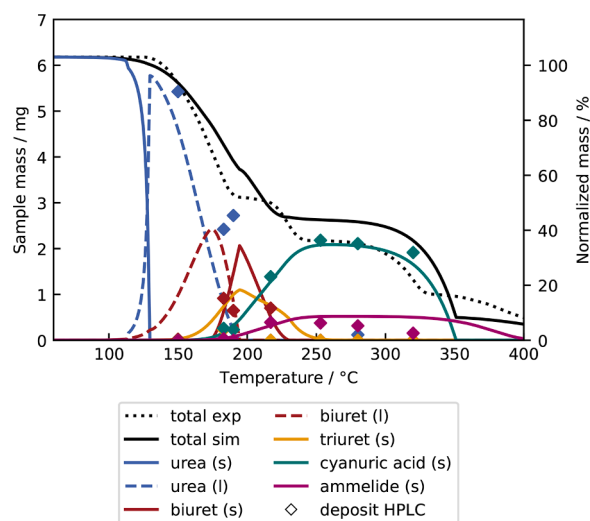


Fig. 35. HPLC analysis results of urea deposits generated at different temperatures. Simulation results for the overall sample mass during urea decomposition and the evolution and consumption of relevant species are compared to experimental TGA and HPLC data. Temperatures of deposit generation are 150, 180, 190, 220, 255, 280 and 320 °C. Reprinted with permission from Börnhorst [150].

results for urea decomposition. Here, the kinetic model proposed by Tischer et al. [223] is applied. From the HPLC results, temperature regimes can be classified by deposit composition. For temperatures below 200 °C, deposits mainly consist of urea and only small amounts of biuret, triuret and cyanuric acid are detected. For temperatures between 200 °C and 250 °C, deposits represent mixtures of biuret, triuret, cyanuric acid and ammelide. In this temperature regime, no urea is left in the samples. Above 250 °C the main component of deposits is cyanuric acid, small amounts of ammelide and ammeline are found. [151]

As shown in Fig. 35, the composition of urea deposits is strongly temperature dependent, as it can be predicted by the evolution and decomposition of by-products during urea decomposition over temperature. The model predicts the temperature regimes for deposit composition well and can therefore benefit the evaluation and design of SCR systems. Generally, high temperatures are often regarded as not critical in terms of solid deposits, as the absolute amount of deposits is low compared to lower temperatures (see Fig. 35). However, in terms of regeneration, deposits formed at high temperatures are persistent and can be accumulated in SCR applications in the long term. Therefore, long-term deposit management requires, on the one hand, sophisticated layout and operation of SCR systems to prevent liquid film formation and deposit build-up, on the other hand, effective regeneration strategies to reduce even high temperature by-products.

In comparison to chemical analyses, literature lacks in detailed topological and morphological characterization of urea deposits. Börnhorst et al. [205] derived topological data on deposits from experiments in a hot gas test rig at different operating conditions, see Fig. 36. The study points out severeness of low temperature operation regarding deposit growth and indicates the effect of operating conditions on deposit load and shape. However, only global structural data is provided. A recent study indicates an influence of the operating conditions on the morphology of solid deposits [233]. Fig. 37 shows microscopic images of deposits derived at a hot gas test rig at two different temperatures.

Crystal structures are identified for the low temperature conditions, while for higher temperatures less structured, porous solids are observed in the top layer of the deposits, while in the bottom layer, similar crystal structures are observed. Differences in morphology are dedicated to different growth mechanisms: *damming growth* and *capillary growth*, which were already observed by Smith et al. [202]. Ates et al. [233]

evaluated 2D and 3D height profiles in terms of surface roughness and performed power spectral density as well as a fractal analyses. Results show strong variations in the surface roughness profiles. Self-affine surfaces and an identical fractal dimension are found for the analyzed deposits. Systematic studies on deposit structure and morphology are desirable for a quantitative description that can be used in further studies concerning wetting behavior, heat and mass transfer or deposit formation kinetics.

7. Role of mixing devices

For efficient NO_x removal, both velocity and species uniformity is required at the entrance of the SCR catalyst to ensure utilization of the entire monolithic catalyst. Mixing lengths for ammonia preparation from UWS are often limited as a result of space restrictions and furthermore, the ideal injection position may not be realized. Static mixing devices are employed to reduce mixing length and the overall size of the aftertreatment system, while maintaining ammonia uniformity at high UWS dosing rates.

Multiple mixer types are available, such as wire-meshes, blade mixer, two-stage mixer and swirl mixer, which differ in their geometrical features [7,234]. When inserting mixing devices to the aftertreatment system, a trade-off between mixing performance and an increase in backpressure has to be found [235]. Furthermore, by introducing additional surfaces to the tailpipe, the risk of film and deposit formation is increased. Wire-mesh mixers package well and do not tend to form deposits, but mixing is poor and backpressure increase is high. Due to a high area-to-volume ratio, evaporation performance is poor. Blade mixers are prone to deposit formation but show good mixing and backpressure performance. Swirl mixers offer excellent mixing performance but deposition free operation results in a substantial backpressure penalty. Two-stage mixers were developed to compensate the mass flow dependent spray impact position by a pre-mixing zone [234]. The choice of mixer type depends on the individual application geometry and operating conditions. [236]

Mixing devices inserted to the SCR mixing section fulfill several functions. By generation of turbulence, mixing devices promote uniform inlet conditions for the SCR catalyst and hence, improve NO_x reduction and decrease ammonia slip as shown in Fig. 38 [7,198,237,238].

Furthermore, mixing elements serve as primary impingement target for the UWS spray and enable secondary atomization [29,202]. Due to exposure to the hot exhaust gas flow, their temperature adapts to the gas temperature resulting in high heat transfer to the impinging liquid [198, 202] compared to heat transfer at the tailpipe wall.

Secondary atomization of impinging UWS on mixing devices is desired and, due to the higher temperatures, droplets are likely to experience thermal breakup or rebound, which are favorable with regard to evaporation and ammonia uniformity. However, consecutive spray impact reduces the mixer temperature and may lead to liquid film formation. In case of a blade mixer, shear flow transports the liquid to the trailing edge of the blades. Here, liquid accumulates and the highly inhomogeneous flow field leads to oscillation. Once a critical amount of liquid is reached, a liquid ligament forms and is cut off the bulk liquid [29]. Fig. 39 shows the formation and detachment of such a ligament at the trailing edge of a mixer blade.

Dörnhöfer et al. [29] have performed experimental and numerical investigations showing that the critical mass for ligament detachment depends on the shear flow velocity and oscillation frequency induced by the mixer flow field. An increase of the shear flow velocity leads to a more frequent breakup of the liquid to ligaments and ligaments to droplets. Furthermore, the secondary droplet size is reduced.

The mechanisms of liquid sheet breakup were studied by numerous authors in the context of air-blast atomization. By high-speed imaging, PDA and PIV measurements, different atomization regimes can be determined [239] and the distributions for the film deformation velocity as well as droplet size and velocity can be assessed [240]. Most works in

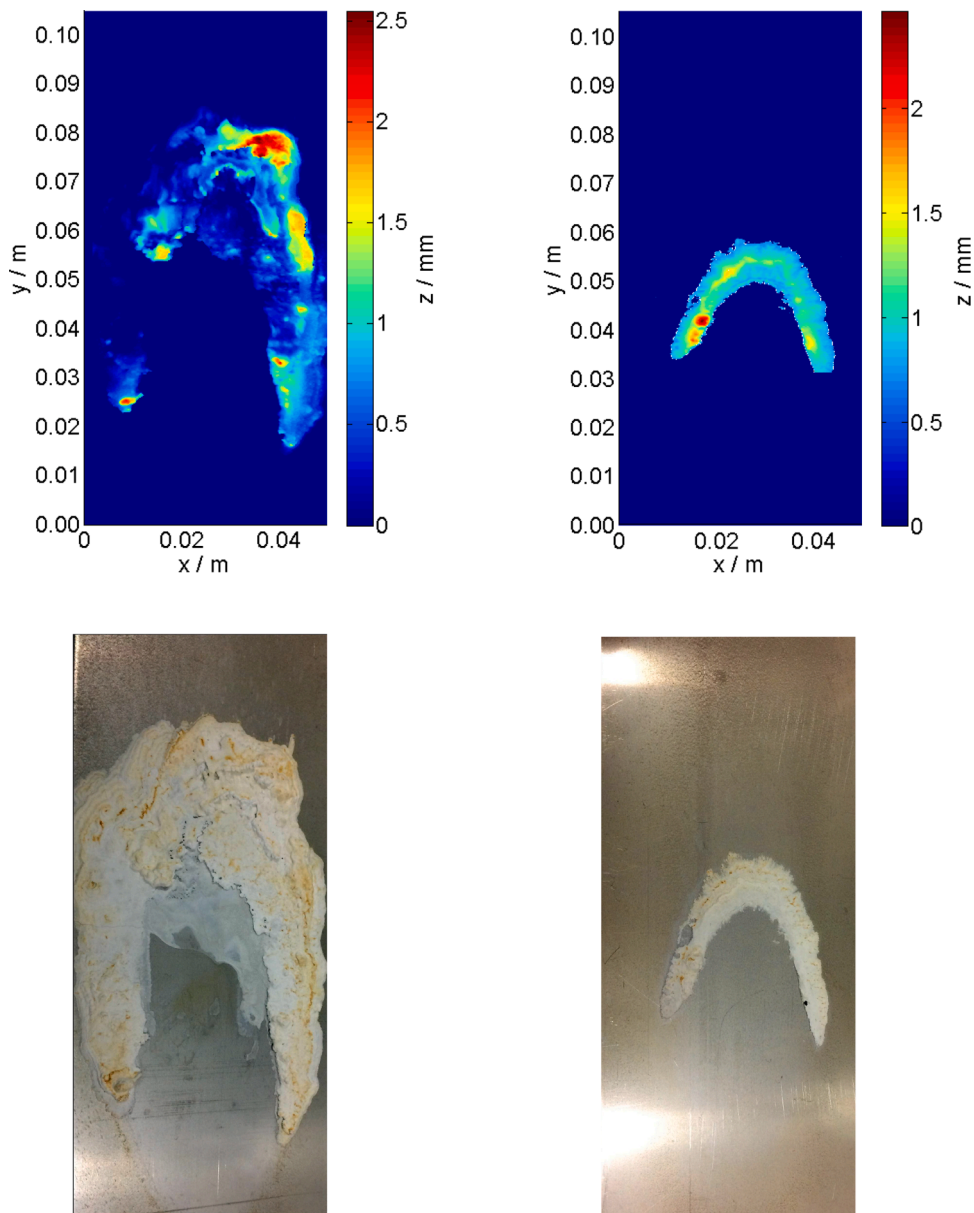


Fig. 36. Topological data and photographs of deposits generated at different operating conditions. Left: 280°C gas temperature, 9.5m s⁻¹ gas velocity; Right: 320°C gas temperature, 8ms⁻¹ gas velocity; positive y-direction represents the flow direction. Reprinted from [205], Copyright (2020), with permission from Elsevier.

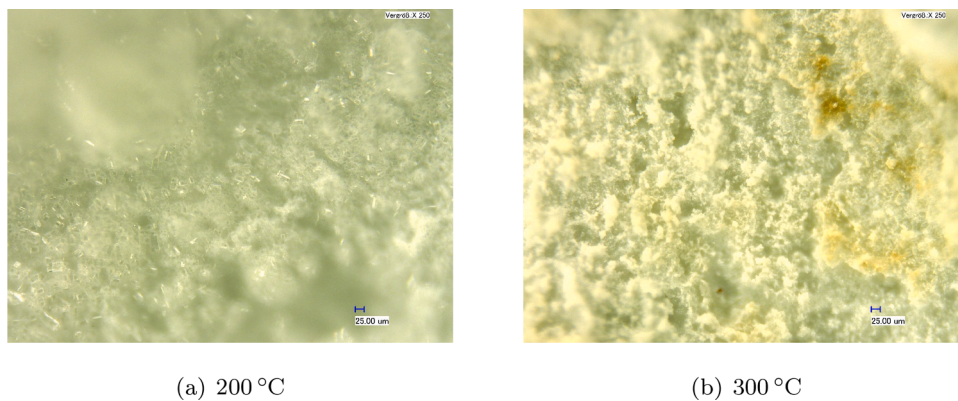


Fig. 37. Microscopic images of deposit samples generated at different gas temperatures in a hot gas test rig. Gas velocity 10ms⁻¹, urea dosage of 1g min⁻¹ for 3 x 45 min.

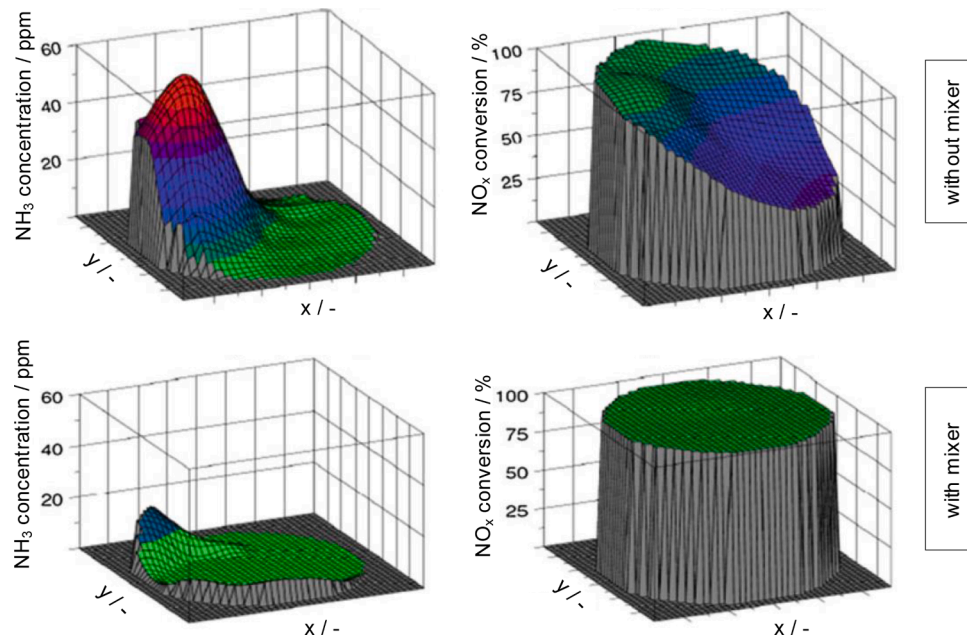


Fig. 38. Influence of an optimized mixing device on NO_x reduction efficiency and ammonia slip. Reprinted by permission from Springer Nature Customer Service Centre GmbH: [7], Springer Nature.

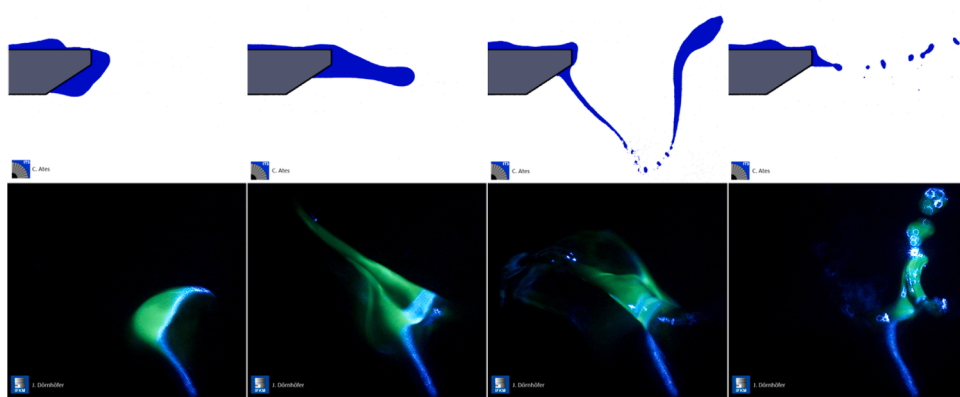


Fig. 39. Liquid accumulation, oscillation, ligament detachment and breakup at a mixer blade edge. Top: simulation by Smoothed Particle Hydrodynamics (SPH) method, bottom: experimental observation by long distance microscopy. Reprinted by permission from Springer Nature Customer Service Centre GmbH: [29], Springer Nature.

this field focus on the spray characteristics downstream the atomizer, which are mainly affected by the air velocity and pressure [241]. Furthermore, liquid properties, such as surface tension, can influence the resulting droplet size [242]. For air-blast atomizers, the effect of liquid film thickness on the Sauter mean diameter of the droplets has not been clarified. On the one hand, an increase in film thickness is stated to increase the SMD [243,244], on the other hand, the film disintegration is described as decoupled from the liquid film thickness at the atomization edge due to liquid accumulation [242,245].

Direct numerical simulation (DNS) is found to be a suitable numerical approach to model primary breakup of air-blast atomization as all scales are resolved. Warncke et al. [240] embedded the highly resolved DNS in a coarser Large eddy simulation (LES). Besides DNS and LES, Volume of fluid (VOF), Reynolds-averaged Navier-Stokes (RANS) and Level set (LS) approaches and their combinations are applied [246,247]. For modeling the entire atomization process including primary and secondary atomization, Eulerian multiphase solvers are coupled with Lagrangian particle tracking [248]. A promising, meshless approach is

given by Smoothed Particle Hydrodynamics (SPH) [249,250]. These achievements in the field of air-blast atomizers might be transferable to the film breakup mechanisms on SCR mixing devices. However, according to the specific conditions and fluid properties, more detailed studies on film breakup on SCR mixing devices are desirable.

Film transport and deposit position are mainly dependent on the operating conditions. Smith et al. [202] investigate wall film flow and deposit formation on a blade mixer in an engine test bench. Results show, that liquid film is extensively distributed from the primary impingement region via blade junctions and film transport takes place on the rear side of the blades. Depending on the contact with impinging liquid, two mechanisms for deposit formation are defined (see Section 6, Fig. 34). Deposits formed on the mixer blades negatively effect the secondary atomization in terms of frequency and secondary droplet size [29]. In the experiments of Smith et al. [202], large secondary droplets are observed for low temperature operation resulting from incomplete preparation of UWS and liquid detachment. Large secondary droplets released by liquid detachment from mixer blades can lead to film

formation downstream the mixer and decrease evaporation efficiency and ammonia uniformity [29]. In close-coupled systems, impingement of these droplets on the catalyst front face is likely.

The use of mixing devices is beneficial for effective ammonia generation from UWS in short distances. However, sufficient mixing performance and, at the same time, avoidance of deposit formation and release of large secondary droplets needs accurate mixer design and positioning as well as knowledge of the mixer operating window. CFD simulation is a valuable tool for design and optimization of mixing devices in SCR systems and will be discussed in the next section.

8. CFD modeling of physical and chemical phenomena in the mixing section

Previous sections discuss the physical and chemical processes in the mixing section of SCR systems relevant for ammonia preparation and the accompanying formation of liquid and solid depositions. Numerical simulation of physical and chemical phenomena in the mixing section of SCR systems by CFD methods is a fundamental tool for system design and optimization. An accurate description of spray evaporation, decomposition and the resulting ammonia distribution particularly contributes to efficient dimensioning of the system layout and catalyst. Furthermore, models capable of predicting potential impingement and harmful deposit formation are desired in aftertreatment engineering. Therefore, there is a strong demand for reliable prediction of the overall system performance by models covering the interactions of all processes in the pipe.

Generally, the solution of the Navier-Stokes equations with finite volume methods is frequently used for SCR applications as it is implemented in open source and commercial CFD software. Prevalent mesh sizes of 2–10 million cells are used depending on application [24]. A common approach is the representation of the spray by a Lagrangian phase. For description of the statistical spray properties and tracking of spray propagation in the turbulent flow field, an adequate number of numerical parcels is introduced. Spray initiation is based on uniform cloud representations with constant droplet size, Rosin-Rammler distributions or experimentally determined droplet size distributions. More detailed representations of the spray can improve SCR performance predictions, as it further increases the accuracy of evaporation and decomposition predictions. LES based studies on UWS spray dynamics are available [251]. A two-zone definition of the spray using different droplet size distributions for the inner and hollow cone was proposed by Rogóz et al. [252]. Experimental spray analysis, as presented in Section 3, is used to validate primary spray atomization and propagation [36,46,53,63,253,254]. Fig. 40 shows numerical results on spray propagation in a hot cross-flow conditions compared to experimental results obtained by shadowgraphy imaging. Several semi-empirical and numerical models were developed for fuel injection and are capable to well predict the spray penetration length [42,44,255,256].

Calculation of the turbulent flow field by appropriate models is decisive for an accurate prediction of spray propagation, mixing and distribution of the required reducing agent ammonia over the catalyst cross-section. RANS models assuming isotropic turbulence are widely applied in SCR related studies, e. g. [17,63,101,257,258]. A more detailed approach of a Reynolds stress model (RSM) was presented by Fischer et al. [198] taking all components of the Reynolds stress tensor into account. Results show an improved representation of the turbulent flow with respect to ammonia uniformity. An adaption of the turbulent Schmidt number is proposed to overcome the underestimation of scalar transport by RANS models. A comparison of different turbulence models indicates the necessity of LES to accurately model the turbulent kinetic energy [259]. Fig. 41 indicates underestimation of the Reynolds stress. The LES results in a good prediction of Reynolds stress, particularly regarding the high turbulent intensity in the exhaust flow core region. Advanced research on suitable turbulence models is desirable, particularly when considering the current developments towards non-tubular

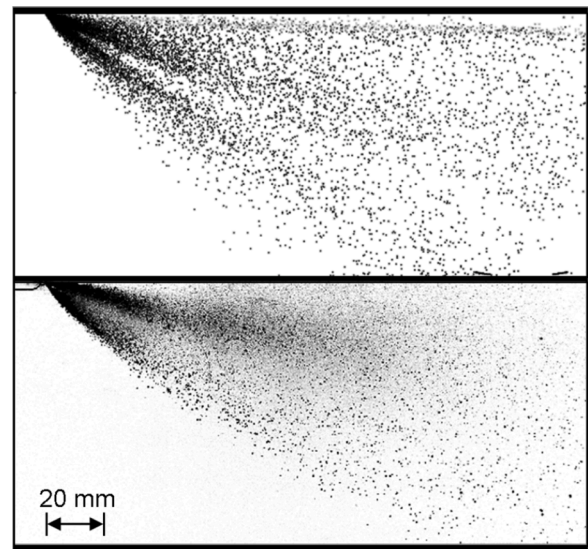


Fig. 40. Simulation result (top) and experimental visualization (bottom) of spray propagation in the experimental setup of Kim et al. [32] for a gas temperature of 150°C and gas velocity of 25m s⁻¹ 10ms after start of injection. Republished with permission of SAE International, from [63]; permission conveyed through Copyright Clearance Center, Inc..

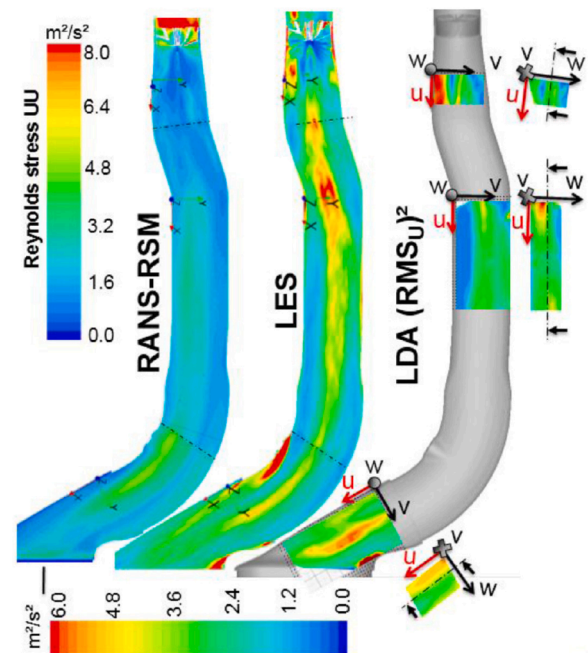


Fig. 41. Comparison of Reynolds stress (UU) prediction by RANS-RSM and LES approach with LDA measurement data in a series exhaust system. Republished with permission of SAE International from [259].

mixing sections and complex mixer geometries.

Another focus of existing SCR modeling studies is the effect of mixing elements on droplet impingement, turbulent flow field and ammonia uniformity [169,198,202,260,261]. Smith et al. [169] investigate ammonia uniformity in two series SCR systems after enhancing and validating a CFD model proposed by Fischer [262]. The study compares a long underbody and a close-coupled SCR system in terms of sensitivity to various parameters and ammonia homogeneity. Results show higher ammonia uniformity for the long SCR system due to increased mixing length and the design of mixer and pipe bends. A comparison of

experimental and numerical results is given in Fig. 42.

Numerical studies involving mixing devices are mostly conducted to evaluate the efficiency of series exhaust geometries. Mixer performance is commonly rated by the ammonia uniformity ahead of the catalyst inlet. However, the simulation results strongly depend on the individual design of the overall SCR system.

Spray evaporation is accounted for by different models discussed in Section 4 [17,28,62,66]. These have been implemented to CFD codes to predict spray penetration and ammonia formation accurately [45,63,68,263,264]. Habchi et al. [68] model spray evaporation in a flow test rig at Diesel exhaust conditions [32]. CFD results show good correlation to the experimentally determined ammonia formation efficiency. The use of reduced models in CFD codes was shown to enable cost-effective prediction of multi-component droplet evaporation [263,264]. Accurate prediction of evaporation kinetics is substantial to further predict the conversion of urea to gaseous reducing agents and the droplet properties prior to impingement.

Numerous studies address numerical modeling of spray impingement and film formation [63,65,169]. Different impingement models are presented in Section 5. Model validation is usually performed by spray impingement experiments in quiescent flow conditions [45,265,266]. Shahariar and Lim [266] use these experiments for validation of a spray/wall interaction model based on approaches of both Kuhnke [132] and Bai and Gosman [125]. A comparison for experimental and simulated spray impingement at quiescent flow conditions is given in Fig. 43.

Optical evaluations based on shadowgraphy measurements as well as wall cooling data determined e. g. by infrared thermal imaging are used for model validation [63,199,266].

Detailed validation of impingement and heat transfer models is decisive for the prediction of the evolving liquid films, which directly affect the amount of solid deposits. 2D liquid film models are frequently used to describe liquid film formation, evaporation and transport [63,101,199,258,267,268]. At reduced complexity, these are capable of predicting shear flow and film breakup phenomena and incorporating evaporation and chemistry models. However, recent studies have shown limitations of the 2D liquid film representation as it is particularly valid

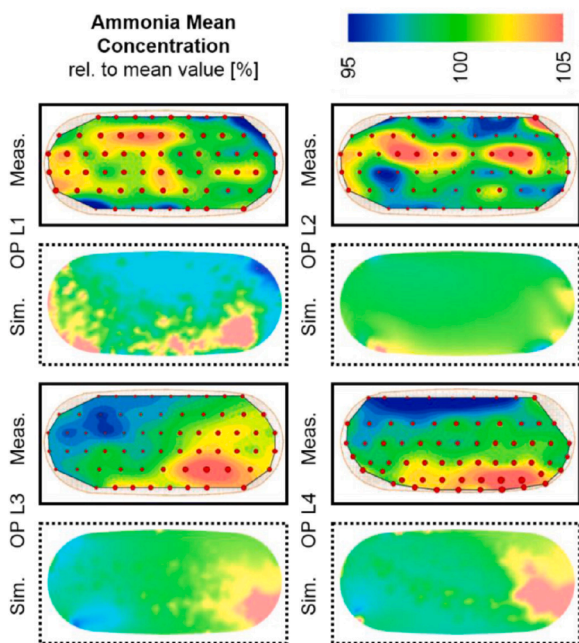


Fig. 42. Ammonia uniformity at the catalyst front face. FTIR measurements and simulation for different operating points with temperatures of 200, 250, 350 and 450°C for OP L1-4 respectively. Republished with permission of SAE International from [169].

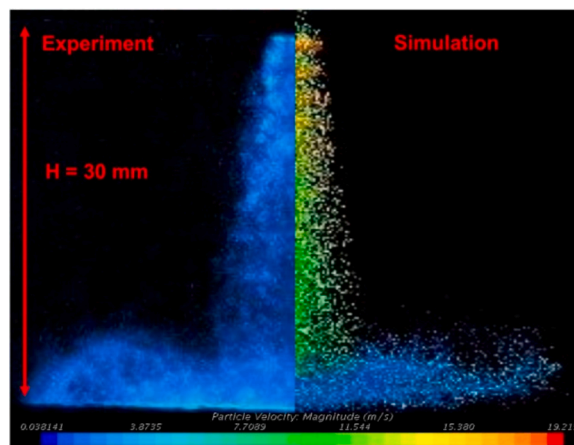


Fig. 43. Comparison of experimental and simulated spray impingement [266].

for thin films ($< 500\mu\text{m}$) [268]. Prediction accuracy is reduced in case of thick UWS films and rivulets [199]. Despite all efforts in liquid film modeling, quantitative experimental data on liquid film thickness for model validation is lacking, as mentioned in Section 6.

Despite these achievements well predicting relevant physics, incorporation of chemical reactions in multi-phase simulations is accompanied by high numerical effort. Here, a particular challenge is the implementation of urea decomposition reactions in the liquid film in CFD simulations [19], which has been extensively studied [68,199,258,267–270]. The target of modeling the long-term evolution of urea deposits in SCR systems yields trade-off solutions concerning the applicable time steps. Fig. 44 gives an overview on the different time step requirements of relevant physical and chemical phenomena.

Spray injection and dispersed flow occur in timescales of milliseconds. Liquid film formation and wall cooling range in timescales of minutes, whereas deposit formation takes place in minutes or even hours. For an adequate representation of injection and spray propagation, numerical time steps of less than milliseconds are required in dependence on gas and droplet velocities. Applying identical time steps for simulations of film and deposit formation would implicate unreasonably high computational costs. For a reliable and quantitative prediction of urea decomposition and by-product formation, different timescale phenomena need to be handled by effective numerical approaches.

Most numerical studies including urea thermal decomposition are limited to the thermolysis and hydrolysis reactions given by Eqs. (1.4) and (1.5) producing ammonia [17,32,53,63,101,202,257,271]. Kim et al. [32] implement a single kinetic rate model to include urea

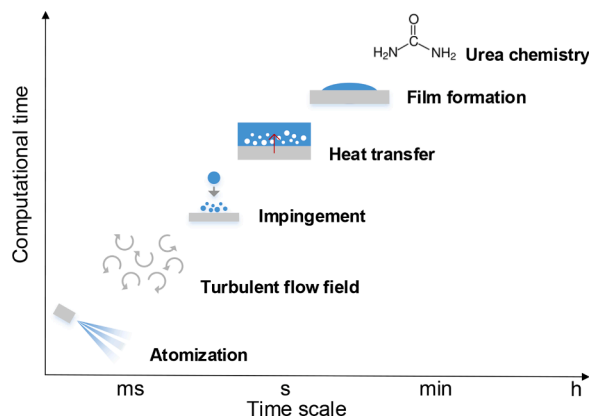


Fig. 44. Time scales of relevant physical and chemical phenomena for comprehensive modeling of UWS decomposition and deposit formation.

decomposition from droplets to a CFD model for prediction of spray mixing and ammonia formation. The Arrhenius expression is defined based on experimental results on ammonia generation. A discrete particle model included in the FLUENT software [272] is used in a Lagrangian frame of reference for modeling spray development. Simulation results match well with measured ammonia conversion data, while no comparison on the spatial ammonia distribution is presented. Further reactions of urea are not included. [32]

Wurzenberger and Wanker [257] presented 3D simulations with Euler-Lagrange approach and the discrete droplet model [273] in FIRE. Here, the monolithic SCR catalyst is integrated to the simulations, which is represented by a 1D model validated by literature data. Considering standard, fast and slow SCR reactions, the calculated rates are used as source terms in the CFD model. Urea thermolysis is accounted for as homogeneous gas phase reaction using a standard power law approach. Subsequent hydrolysis of isocyanic acid or other reactions of urea are not considered. Adequate prediction of SCR reactions is shown, whereas no validation for urea decomposition is presented. [257]

A comprehensive modeling approach comprising multi-phase interactions as well as urea thermo-hydrolysis was first presented by Birkhold et al. [63]. The model describes the turbulent flow and the Lagrangian droplet phase including evaporation and spray/wall interaction. Wall heat transfer and two-component film formation is accounted for. Spray/wall interaction and impingement heat transfer are simulated using models by Kuhnke [132] and Wruck [197] respectively. The fluid film is represented by a 2D finite volume model. Nukiyama boiling [274] is applied to model heat transfer from wall to film. An interface of the CFD software to the Chemkin chemistry solver is utilized to implement urea thermolysis and hydrolysis as homogeneous gas phase reactions. Good agreement to experimental data from Kim et al. [32] is achieved in terms of ammonia conversion as function of gas temperature and velocity. A spray impingement setup is used to validate predicted wall cooling. Fig. 45 shows simulation results for the liquid film thickness and urea content. The wall film is predicted for an injection of 0.83g UWS at a gas temperature of 340 °C.

Evaporation of the wall film is considered in the model, but urea reactions inside the film are not included. Simulation results for film thickness and urea concentration are not compared to experimental data. However, this model enables the prediction of liquid deposition

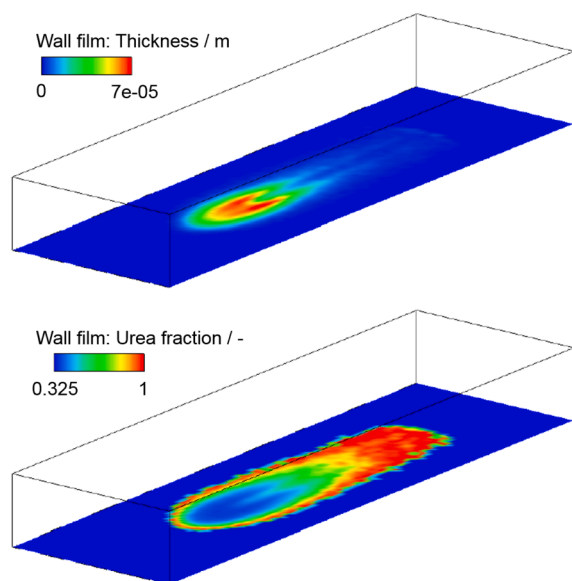


Fig. 45. Simulation results for wall film thickness and urea concentration for an injection of 0.83g UWS at a gas temperature of 340°C derived by a 3D simulation in FIRE. Republished with permission of SAE International, from [63]; permission conveyed through Copyright Clearance Center, Inc..

and indicates critical locations for solid formation. [63]

Numerous subsequent CFD studies rely on the models developed by Birkhold et al. [17,63] in terms of both multi-phase physics and UWS droplet evaporation and decomposition [53,101,202,271].

Aiming to a prediction of deposit formation, several authors enhanced their models by routines to evaluate a deposition risk based on temperature and concentration data in the liquid film [101,199,202,269,275]. This procedure demonstrates critical operating conditions and locations prone to deposit formation. Smith et al. [202] developed a routine to evaluate the risk of deposit formation based on a choice of parameters describing wall film dynamics as well as temperature and concentration data of the liquid film. Fig. 46 presents a visualization of the deposition risk on a mixer blade. A chemistry model describing secondary reactions of urea to solid by-products is not implemented.

Sun et al. [269] presented another approach for prediction of urea deposit formation by a CFD simulation. The procedure includes simulations of the steady flow, spray development, impingement, local wall cooling, a wall film property based evaluation of deposition risk and simulations with a detailed urea decomposition mechanism. Simulations were carried out in the CONVERGE CFD software package and were compared to experiments at an engine test setup. Results are in good agreement with experimental data in terms of deposit location and qualitative composition. However, the simulations were limited to several seconds and are only partially comparable to deposits derived from experiments of 12 h duration.

Habchi et al. [258] account for the competition of isocyanic acid hydrolysis and urea by-product formation by implementing a semi-detailed urea decomposition model into a CFD simulation. The model comprises 12 reactions including the by-products biuret, cyanuric acid and ammeline. Despite a more detailed description of urea decomposition, the model lacks in physical property data of the different compounds as they are assumed to be equal to pure water. Wall temperatures are set identical to the gas temperatures as no heat transfer model is implemented. Based on simulation results, two temperature regimes for deposit formation are proposed. Excessive computational costs limit the simulation duration to 1s and hinder validation by comparison to experimental data on urea decomposition and deposit formation. Computation time for one second of physical time amounts to one week using 256 cores. [258]

The kinetic model was further implemented to the Lagrangian phase model in a subsequent publication [68]. Simulation results are compared to experimental data of UWS droplet evaporation on

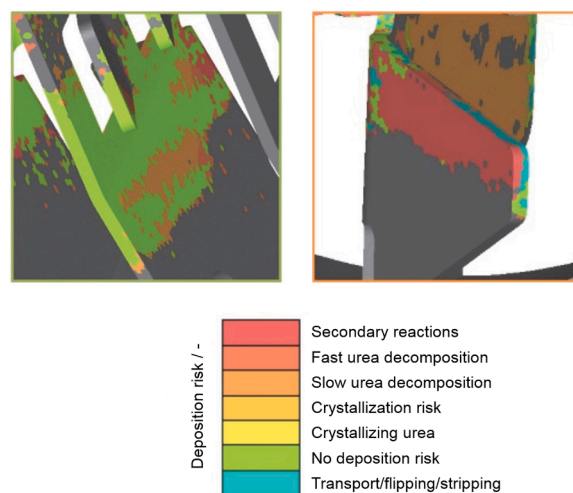


Fig. 46. Deposition risk on the upstream area (left) and the rear blade side (right) calculated from liquid film simulation data such as velocity, temperature and concentrations. Republished with permission of SAE International from [202].

thermocouple rings and quartz beads [58,59] and show satisfactory agreement with regard to droplet size and temperature. The model was further validated against experimental data on spray injection to a hot gas tube from Kim et al. [32]. Good agreement was achieved for different gas temperatures, flow rates and residence times. No detailed information on the computational costs or the effect of the kinetics implementation is available.

Recently, a detailed kinetic model and thermodynamic equilibria of relevant species were integrated into the CFD code StarCCM+ [267]. In this study, physical models and respective parameters describing spray propagation, impingement, film formation and evaporation were applied according to Fischer [262]. By user coding, a 0D batch reactor algorithm for calculation of reaction rates in multiple phases and an adaption of the kinetic scheme proposed by Brack et al. [100] was implemented to the commercial CFD code StarCCM+. This procedure enables the calculation of production and consumption rates of urea, biuret, triuret, cyanuric acid and ammeline based on temperature and concentration data in the liquid film. The procedure was validated against TGA experiments and applied to simulations of a hot gas test rig. Results show acceptable prediction of spray impingement and film formation. However, comparison with experimental data reveals deficits of the applied physical models. Particularly the impingement and heat transfer models lack in accuracy. Due to the implementation of urea decomposition kinetics, the model is able to predict urea reactions in the liquid film and the formation of urea by-products can be investigated locally. Fig. 47 shows an example for deposit formation in the liquid film for a gas temperature of 220 °C and a gas velocity of 11 ms⁻¹ after 18 min physical time.

In relation to the physical time, computational costs are not significantly increased by the integration of decomposition kinetics. However, due to the discrepancy of time step requirements for different physical and chemical phenomena, presented simulations over minutes are highly cost intensive. Limited comparability of experimental and simulation results on deposit composition is given as the experimental duration is 2h, whereas the simulated time is less than 20min.

Tackling the timescale problem, Budziankou et al. [268] proposed a spray source approach significantly reducing computational time. Here, spray parcels are substituted by source terms of mass, momentum and energy, which are applied to the film and gas phase. Pre-simulations of spray injection at different conditions (e.g. gas temperature) were performed using small time steps (0.3 ms) to calculate and save the source terms for the gas and liquid phase. The pre-calculated source terms were then applied to unsteady simulations, where they substitute the Lagrangian parcels and enable the use of larger time steps (5–10 ms). In case of transient operating conditions, source terms were updated periodically. Urea decomposition kinetics were calculated in detail relying on the implementation described by Börnhorst et al. [267]. Simulation results were compared to experimental data from an engine test bench and show good agreement in terms of film formation, wall cooling and position of deposits. Quantitative comparison of deposits after 20min experimental and simulation duration shows deviations, which are attributed to an underestimated isocyanic acid concentration in the liquid film in the simulations. Furthermore, the implementation of recent mechanisms for urea decomposition [223] is recommended.

In a subsequent publication, in addition to the spray source approach, Budziankou et al. [199] implemented a modified Bai-Oneira [167] impingement and Wruck [197] heat transfer model to overcome the aforementioned shortcomings. Furthermore, the deposition risk estimation routine proposed by Smith et al. [202] was adapted and applied to simulations of two engine test benches. Deposition inhibiting and promoting liquid film properties were identified and empirically determined threshold values were applied. Simulation results correlate well with experimental findings, while maintaining reasonable computational speed of 45 - 65sd⁻¹, which is far beyond the capabilities of most mentioned studies. The presented reduction of computational time, for the first time, enables model verification by a direct

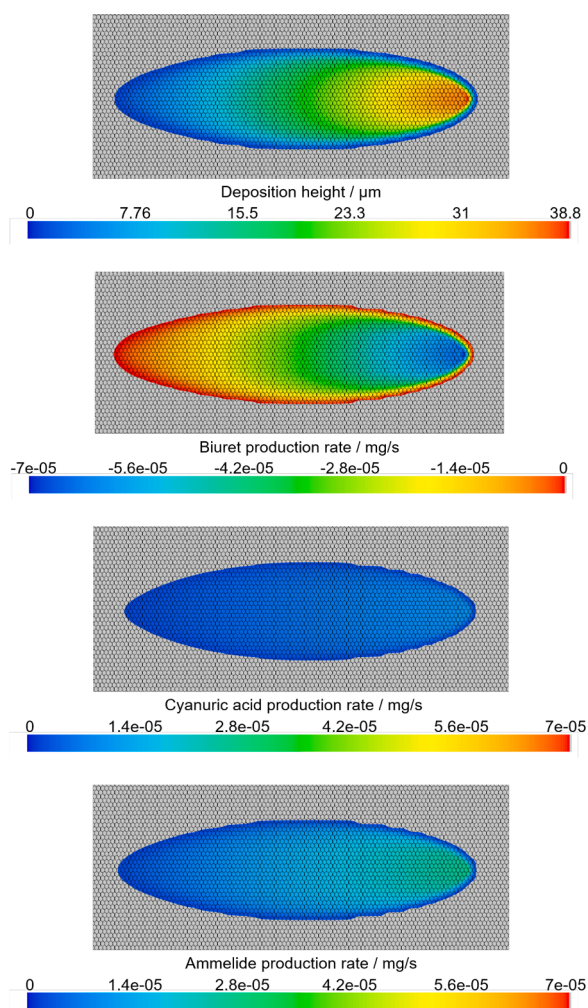


Fig. 47. Simulated solid deposition thickness and by-product formation in the liquid film (gas temperature 220°C, gas velocity 11 ms⁻¹).

comparison of numerical and experimental results for identical time scales [199,268]. Previous studies, constrained by high computation costs, used to correlate experimental results on deposit composition measured after several hours of operation to simulation results for seconds or minutes of physical time [202,258,267,269,275,276].

Consecutive developments of sub-models relevant to UWS injection, evaporation and decomposition in SCR systems by different research groups have led to accurate, comprehensive CFD models describing the overall process from injection to deposit formation. Presented studies demonstrate the capabilities and frequent use of existing CFD models to predict ammonia generation from UWS injection accompanied by liquid and solid depositions. However, high computational costs result from small time step requirements for the representation of the Lagrangian phase in combination with the implementation of urea decomposition kinetics. First approaches to overcome this obstacle were made and implementations to assess deposition risk and to calculate urea decomposition in detail are available.

9. Conclusion and outlook

Efficient NO_x removal by urea SCR systems demands a complete conversion of adequately dosed urea to ammonia and its homogeneous distribution over the catalyst cross section without system degradation by solid by-product deposits. Over the last two decades, tremendous efforts have been made towards a better understanding of physical and chemical sub-processes in the mixing section of SCR systems, which

today enables model-based design of aftertreatment devices.

Detailed knowledge of injection characteristics and spray development is required to enable complete evaporation. A wide range of measurement techniques has been developed to characterize injectors as well as spray evaporation and mixing in diverse system layouts. However, determination of droplet size and velocity distributions at realistic, transient conditions involving high temperatures and non-ideal sprays remains a challenge and limits the prediction accuracy of droplet kinematics and evaporation models.

The gas phase composition, affected by droplet evaporation and urea decomposition, and homogeneous reactions have so far been handled with low priority in urea SCR related research. Several studies call for a better understanding of gas phase reactions, particularly including isocyanic acid, as it affects the catalysts' potential and harmful deposit formation. Low reactivity of isocyanic acid in the gas phase decreases the NO_x removal rate and bears the risk of HNCO emissions. More detailed studies on homogeneous reactions at SCR conditions, HNCO stability and catalytic HNCO hydrolysis are recommended.

Despite sophisticated injector design, system layout and operation, incomplete evaporation and impingement of droplets on the physical system boundaries needs to be accepted and controlled as part of the urea conversion process. In particular, the development towards close-coupled positioning of the aftertreatment system inevitably leads to liquid/wall and liquid/mixer contact. Multi-functional mixer development dedicated not only to turbulence induction, but also to heat transfer and secondary atomization deserves increased attention. Advanced integration of catalytic functions enhancing HNCO hydrolysis might improve urea conversion efficiency. Based on droplet impingement experiments, regime classifications and several models for spray/wall interaction of UWS were developed, which are continuously applied in CFD tools for the development of SCR technologies. However, experimental validation data and respective models have to be performed and selected carefully. Existing regime maps integrate important thermal and kinetic parameters, but not all relevant parameters are accounted for. Recent studies indicate a strong influence of surface properties, particularly wettability and roughness, on hydrodynamic and thermal effects during droplet impact and also reveal hysteresis and memory effects. Furthermore, experimentally determined regime data usually cover a limited range of parameters, such as droplet size, velocity and surface temperature. Extrapolation of regime boundaries to SCR relevant conditions, in particular, the application of data obtained by relatively large and slow droplets to modeling of impingement with small droplets and high velocities demands adequate verification. Furthermore, a suitable transfer of single droplet data to spray models is required. Modeling and utilization of spray/wall interaction is of utmost importance, as it represents the initiation of liquid and solid deposits in SCR systems.

Liquid accumulation, evaporation and transport is rarely studied under realistic conditions as transient measurements of film thickness and concentrations are challenging. These valuable data can contribute to the predictive accuracy of film and deposition models, which are mostly limited to 2D representations in CFD.

Extensive research is available on the position and quantity of solid urea by-products deposited on system walls and mixing devices of diverse SCR geometries. Methods are available for temperature dependent deposit composition analysis and modeling. Yet, long-term accumulation, durability and regeneration strategies of high temperature by-products should not be disregarded. Furthermore, detailed studies on deposit morphology will help to understand the growth mechanisms and predict deposit formation.

Over the last years, there has been significant progress towards predictive modeling of the entire process, including deposit formation, with regard to SCR system engineering and optimization. Presented modeling approaches are promising and push the limits of today's computational capabilities. Despite the scientific interest in integration of chemical kinetics to turbulent, multi-phase flow simulations,

deposition risk approaches are considered to be of increased value to SCR system engineering compared to more detailed deposition models with respect to computational efficiency. Existing CFD models with integrated urea decomposition kinetics often lack in detailed comparison and validation with quantitative experimental data on deposit formation, as the duration of experiments strongly exceeds the simulated physical time.

Particularly for modern, close-coupled systems, interaction of the droplets with the catalyst front face and potential liquid and solid depositions inside the catalyst channels need to be accounted for. These need to be addressed in addition to investigations on the SCR catalytic activity on isocyanic hydrolysis, especially with respect to potential future emission legislations for HNCO and N₂O. Furthermore, the trend towards combination and integration of aftertreatment components, e. g. SCR coated DPF, imposes new challenges.

Several decades of research and development in academics and industry have established urea-based SCR systems as a state-of-the-art aftertreatment technique for NO_x removal from the emissions of IC engines. Existing experimental and numerical methods bear the potential to develop SCR systems according to future requirements of emission regulations independently from the drive technology. The challenge of NO_x removal will remain as long as air is used as oxidizer in combustion systems.

Declaration of Competing Interest

The authors declare that they have no known competing financial interest or personal relationships that could have appeared to influence the work reported in this paper.

Acknowledgements

The authors kindly acknowledge financial support by the German Research Foundation (Deutsche Forschungsgemeinschaft, DFG) through project 237267381 - TRR 150. Our research was further funded by the Research Association for Combustion Engines e.V. (Forschungsvereinigung Verbrennungskraftmaschinen e.V., FVV) and the German Federation of Industrial Research Associations (Arbeitsgemeinschaft industrieller Forschungsvereinigungen, AiF). Furthermore, we appreciate financial support by the Friedrich and Elisabeth Boysen Foundation. We acknowledge Steinbeis GmbH & Co. KG für Technologietransfer (STZ 240 Reaktive Strömung) for a cost-free license of DETCHEM. We would like to thank our colleagues Christian Kuntz, Anna Bertóiné Abai and Carola Kuhn (KIT) for their contributions to our research. Steffen Tischer (KIT) is acknowledged for his support in development of the DETCHEM^{MPTR} module and kinetic modeling. We would like to sincerely thank Thomas Lauer (TU Vienna) for fruitful discussions and cooperation in our joint project (FVV 6012623).

References

- [1] Koch TA, Boehlke T. The averaging bias - a standard miscalculation, which extensively underestimates real CO₂ emissions. *ZAMM Journal of Applied Mathematics and Mechanics* 2021.
- [2] Seboldt D, Lejsek D, Bargende M. Injection strategies for low HC raw emissions in SI engines with CNG direct injection. *Automotive and Engine Technology* 2016; 60:81–91. <https://doi.org/10.1007/s41104-016-0002-4>.
- [3] Lott P, Deutschmann O. Lean-Burn Natural Gas Engines: Challenges and Concepts for an Efficient Exhaust Gas Aftertreatment System. *Emission Control Science and Technology* 2020;7:1–6. <https://doi.org/10.1007/s40825-020-00176-w>.
- [4] Wang Y, Banerjee A, Deutschmann O. Dynamic behavior and control strategy study of CO₂/H₂O co-electrolysis in solid oxide electrolysis cells. *Journal of Power Sources* 2019;412:255–64. <https://doi.org/10.1016/j.jpowsour.2018.11.047>.
- [5] Borchers M, Keller K, Lott P, Deutschmann O. Selective Catalytic Reduction of NO_x with H₂ for Cleaning Exhausts of Hydrogen Engines: Impact of H₂O, O₂, and NO/H₂ Ratio. *Industrial & Engineering Chemistry Research* 2021;60:6613–26. <https://doi.org/10.1021/acs.iecr.0c05630>.

- [6] Knirsch S, Weiß U, Fröhlich A, Pamio G, Helbig J, Ritter H. The new generation of the Audi V6 TDI engine: 25 years of Technology - Dynamics - Innovation, Vienna, Austria. 2014.
- [7] Nova I, Tronconi E. Urea-SCR Technology for deNOx After Treatment of Diesel Exhausts. Springer New York; 2014. <https://doi.org/10.1007/978-1-4899-8071-7>.
- [8] Solla A, Westerholm M, Söderström C, Tormonen K, Härmä T, Nissinen T, et al. Effect of Ammonium Formate and Mixtures of Urea and Ammonium Formate on Low Temperature Activity of SCR Systems. SAE Technical Paper 2005;(2005-01-1856). <https://doi.org/10.4271/2005-01-1856>.
- [9] Kröcher O, Elsener M, Jacob E. New reducing agents for the low-NOx SCR technology. Proceedings of the 5th International Exhaust Gas and Particulate Emissions Forum, Ludwigsburg 2008.
- [10] Ramachandran BR, Halpern AM, Glendening ED. Kinetics and Mechanism of the Reversible Dissociation of Ammonium Carbamate: Involvement of Carbamic Acid. The Journal of Physical Chemistry A 1998;102(22):3934–41. <https://doi.org/10.1021/jp980376n>.
- [11] Wilson JG, Hargrave G. Analysis of a Novel Method for Low-Temperature Ammonia Production Using DEF for Mobile Selective Catalytic Reduction Systems. SAE Technical Paper 2018;(2018-01-0333). <https://doi.org/10.4271/2018-01-0333>.
- [12] Elmøe TD, Sørensen RZ, Quaade U, Christensen CH, Nørskov JK, Johannessen T. A high-density ammonia storage/delivery system based on Mg(NH₃)₆Cl₂ for SCR – DeNOx in vehicles. Chemical Engineering Science 2006;61(8):2618–25. <https://doi.org/10.1016/j.ces.2005.11.038>.
- [13] Deutschmann O, Grunwaldt J-D. Abgasnachbehandlung in mobilen Systemen: Stand der Technik, Herausforderungen und Perspektiven. Chemie Ingenieur Technik 2013;85(5):595–617. <https://doi.org/10.1002/cite.201200188>.
- [14] Merker GP, Teichmann R. Grundlagen Verbrennungsmotoren. Springer Fachmedien Wiesbaden; 2018. <https://doi.org/10.1007/978-3-658-19212-9>.
- [15] Balland J, Schreurs B, Peters M, Parmentier M, Schmitt J, Hardam H, et al. A Super Clean Diesel Vehicle for US LEV-III SULEV Category: Second Report; Advanced A/F Control for NOx Reduction and for SCR Heat Up. Proceedings of the FISITA 2012 World Automotive Congress 2012;189:183–93. https://doi.org/10.1007/978-3-642-33841-0_14.
- [16] Rammelt T, Torkashvand B, Hauck C, Böhm J, Gläser R, Deutschmann O. Nitric Oxide Reduction of Heavy-Duty Diesel Off-Gas by NH₃-SCR in Front of the Turbocharger. Emission Control Science and Technology 2017;3(4):275–88. <https://doi.org/10.1007/s40825-017-0078-y>.
- [17] Birkhold F. Selektive katalytische Reduktion von Stickoxiden in Kraftfahrzeugen: Untersuchung der Einspritzung von Harnstoffwasserlösung. Karlsruhe, Germany: Karlsruhe Institute of Technology; 2007. PhD thesis.
- [18] Grout S, Blaisot J-B, Pajot K, Osbat B. Experimental investigation on the injection of an urea–water solution in hot air stream for the SCR application: Evaporation and spray/wall interaction. Fuel 2013;106:166–77. <https://doi.org/10.1016/j.fuel.2012.09.022>.
- [19] Brack W, Heine B, Birkhold F, Kruse M, Deutschmann O. Formation of Urea-Based Deposits in an Exhaust System: Numerical Predictions and Experimental Observations on a Hot Gas Test Bench. Emission Control Science and Technology 2016;2(3):115–23. <https://doi.org/10.1007/s40825-016-0042-2>.
- [20] Schaber PM, Colson J, Higgins S, Thielen D, Anspach B, Brauer J. Thermal decomposition (pyrolysis) of urea in an open reaction vessel. Thermochimica Acta 2004;424(1-2):131–42. <https://doi.org/10.1016/j.tca.2004.05.018>.
- [21] Lundström A, Andersson B, Olsson L. Urea thermolysis studied under flow reactor conditions using DSC and FT-IR. Chemical Engineering Journal 2009;150(2-3):544–50. <https://doi.org/10.1016/j.cej.2009.03.044>.
- [22] Eichelbaum M, Farrauto RJ, Castaldi MJ. The impact of urea on the performance of metal exchanged zeolites for the selective catalytic reduction of NOx: Part I. Pyrolysis and hydrolysis of urea over zeolite catalysts. Applied Catalysis B: Environmental 2010;97(1-2):90–7. <https://doi.org/10.1016/j.apcatb.2010.03.027>.
- [23] Bernhard AM, Peitz D, Elsener M, Wokaun A, Kröcher O. Hydrolysis and thermolysis of urea and its decomposition byproducts biuret, cyanuric acid and melamine over anatase TiO₂. Applied Catalysis B: Environmental 2012;115-116:129–37. <https://doi.org/10.1016/j.apcatb.2011.12.013>.
- [24] Lauer T. Preparation of Ammonia from Liquid AdBlue - Modeling Approaches and Future Challenges. Chemie Ingenieur Technik 2018;90(6):783–94. <https://doi.org/10.1002/cite.201700107>.
- [25] Kapusta LJ, Teodorczyk A. Laser diagnostics for urea-water solution spray characterization. MATEC Web of Conferences 2017;118:00029. <https://doi.org/10.1051/mateconf/201711800029>.
- [26] Kapusta LJ, Sutkowski M, Rogóż R, Zommara M, Teodorczyk A. Characteristics of Water and Urea–Water Solution Sprays. Catalysts 2019;9(9):750. <https://doi.org/10.3390/catal9090750>.
- [27] Lieber C, Koch R, Bauer H-J. Microscopic Imaging Spray Diagnostics under High Temperature Conditions: Application to Urea–Water Sprays. Applied Sciences 2019;9(20):4403. <https://doi.org/10.3390/app9204403>.
- [28] Lieber C, Koch R, Bauer H-J. Spray evaporation of urea–water solution: Experiments and modelling. Experimental Thermal and Fluid Science 2020;116:110108. <https://doi.org/10.1016/j.expthermflusci.2020.110108>.
- [29] Dörnhöfer J, Börnhorst M, Ates C, Samkhaniani N, Pfeil J, Wörner M, et al. A Holistic View on Urea Injection for NOx Emission Control: Impingement, Re-atomization, and Deposit Formation. Emission Control Science and Technology 2020;6(2):228–43. <https://doi.org/10.1007/s40825-019-00151-0>.
- [30] Spiteri A, Dimopoulos Eggenschwiler P. Experimental Fluid Dynamic Investigation of Urea–Water Sprays for Diesel Selective Catalytic Reduction–DeNOx Applications. Industrial & Engineering Chemistry Research 2014;53(8):3047–55. <https://doi.org/10.1021/ie404037h>.
- [31] Liao Y, Nocivelli L, Dimopoulos Eggenschwiler P, Spiteri A. Experimental investigation of urea-water sprays in selective catalytic reduction (SCR) systems. Proceedings of the 15th Stuttgart International Symposium 2012:953–66. https://doi.org/10.1007/978-3-658-08844-6_65.
- [32] Kim JY, Ryu SH, Ha JS. Numerical prediction on the characteristics of spray-induced mixing and thermal decomposition of urea solution in SCR systems. Proceedings of ICEF04, 2004 Fall Technical Conference of the ASME Internal Combustion Engine Division 2004;(889).
- [33] Postriotti L, Brizi G, Ungaro C, Mosser M, Bianconi F. A methodology to investigate the behaviour of urea-water sprays in high temperature air flow for SCR de-NOx applications. Fuel 2015;150:548–57. <https://doi.org/10.1016/j.fuel.2015.02.067>.
- [34] Payri R, Bracho G, Gimeno J, Moreno A. Investigation of the urea-water solution atomization process in engine exhaust-like conditions. Experimental Thermal and Fluid Science 2019;108:75–84. <https://doi.org/10.1016/j.expthermflusci.2019.05.019>.
- [35] Oh J, Lee K. Spray characteristics of a urea solution injector and optimal mixer location to improve droplet uniformity and NOx conversion efficiency for selective catalytic reduction. Fuel 2014;119:90–7. <https://doi.org/10.1016/j.fuel.2013.11.032>.
- [36] Payri R, Bracho G, Martí-Aldaraví P, Marco-Gimeno J. Computational Study of Urea–Water Solution Sprays for the Analysis of the Injection Process in SCR-like Conditions. Industrial & Engineering Chemistry Research 2020;59(41):18659–73. <https://doi.org/10.1021/acs.iecr.0c02494>.
- [37] Liao Y, Dimopoulos Eggenschwiler P, Spiteri A, Nocivelli L, Montenegro G, Boulouchos K. Fluid Dynamic Comparison of AdBlue Injectors for SCR Applications. SAE International Journal of Engines 2015;8(5):2303–11. <https://doi.org/10.4271/2015-24-2502>.
- [38] Spiteri A, Dimopoulos Eggenschwiler P, Liao Y. Comparison of pressure and air-assisted atomizers for Urea-SCR injection in diesel engine exhaust. In: Bargende M, Reuss H-C, Wiedemann J, editors. 14. Internationales Stuttgarter Symposium. Wiesbaden: Springer Fachmedien Wiesbaden; 2014. ISBN 978-3-658-05129-7. p. 911–21. https://doi.org/10.1007/978-3-658-05130-3_65.
- [39] Huthwohl G, Dolenc S. A new Approach in AdBlue Dosing to Improve Performance and Durability of SCR Systems for the Use in Passenger Cars up to Heavy Duty Vehicles. SAE Technical Paper 2011-01-2095. <https://doi.org/10.4271/2011-01-2095>.
- [40] Cai X, Wörner M, Marschall H, Deutschmann O. CFD Simulation of Liquid Back Suction and Gas Bubble Formation in a Circular Tube with Sudden or Gradual Expansion. Emission Control Science and Technology 2017;3(4):289–301. <https://doi.org/10.1007/s40825-017-0073-3>.
- [41] van Vuuren N, Postriotti L, Brizi G, Picchiotti F. Instantaneous Flow Rate Testing with Simultaneous Spray Visualization of an SCR Urea Injector at Elevated Fluid Temperatures. SAE International Journal of Engines 2017;10(5):2478–85. <https://doi.org/10.4271/2017-24-0109>.
- [42] Wan Y, Peters N. Scaling of spray penetration with evaporation. Atomization and Sprays 1999;9(2):111–32. <https://doi.org/10.1615/AtomizSpr.v9.i2.10>.
- [43] Araneo L, Coghe A, Brunello G, Cossali G. Experimental Investigation of Gas Density Effects on Diesel Spray Penetration and Entrainment. SAE Transactions 1999;(108):679–93.
- [44] Roisman IV, Araneo L, Tropea C. Effect of ambient pressure on penetration of a diesel spray. International Journal of Multiphase Flow 2007;33(8):904–20. <https://doi.org/10.1016/j.ijmultiphaseflow.2007.01.004>.
- [45] Birkhold F, Meingast U, Wassermann P, Deutschmann O. Modeling and simulation of the injection of urea-water-solution for automotive SCR DeNOx-systems. Applied Catalysis B: Environmental 2007;70(1-4):119–27. <https://doi.org/10.1016/j.apcatb.2005.12.035>.
- [46] Varna A, Spiteri AC, Wright YM, Dimopoulos Eggenschwiler P, Boulouchos K. Experimental and numerical assessment of impingement and mixing of urea–water sprays for nitric oxide reduction in diesel exhaust. Applied Energy 2015;157:824–37. <https://doi.org/10.1016/j.apenergy.2015.03.015>.
- [47] van Vuuren N, Brizi G, Buitoni G, Postriotti L, Ungaro C. AUS-32 Injector Spray Imaging on Hot Air Flow Bench. SAE Technical Paper Series. SAE International 400 Commonwealth Drive, Warrendale, PA, United States; 2015. <https://doi.org/10.4271/2015-01-1031>.
- [48] Corbeels PL, Senter DW, Lefebvre AH. Atomization characteristics of a high-speed rotary-bell paint applicator. Atomization and Sprays 1992;2(2):87–99. <https://doi.org/10.1615/AtomizSpr.v2.i2.20>.
- [49] Dorfner V, Donnich J, Durst F, Kohler R. Viscosity and surface tension effects in pressure swirl atomization. Atomization and Sprays 1995;5(3):261–85. <https://doi.org/10.1615/AtomizSpr.v5.i3.20>.
- [50] Shah PR, Ganesh A. Study the influence of pre-heating on atomization of straight vegetable oil through Ohnesorge number and Sauter mean diameter. Journal of the Energy Institute 2018;91(6):828–34. <https://doi.org/10.1016/j.joei.2017.10.006>.
- [51] Urbán A, Malý M, Józsa V, Jedelský J. Effect of liquid preheating on high-velocity airblast atomization: From water to crude rapeseed oil. Experimental Thermal and Fluid Science 2019;102:137–51. <https://doi.org/10.1016/j.expthermflusci.2018.11.006>.
- [52] Kulkarni AP, Megaritis T, Ganippa LC. Insights on the morphology of air-assisted breakup of urea-water-solution sprays for varying surface tension. International Journal of Multiphase Flow 2020;133:103448. <https://doi.org/10.1016/j.ijmultiphaseflow.2020.103448>.

- [53] Nayak NS. The Evaporation and Spray Wall Interaction Behavior of Urea Water Solution (UWS) in Selective Catalytic Reduction (SCR) Systems of Modern Automobiles. SAE Technical Paper 2013;(2013-24-0162). <https://doi.org/10.4271/2013-24-0162>.
- [54] Elperin T, Krasovtsov B. Analysis of evaporation and combustion of random clusters of droplets by a modified method of expansion into irreducible multipoles. *Atomization and Sprays* 1994;4(1):79–97. <https://doi.org/10.1615/AtomizSpr.v4.i1.40>.
- [55] Greenberg JB, Katoshevski D. Vaporization Damköhler Number and Enrichment Effects in Spray Diffusion Flames in an Oscillating Flow Field. *Combustion Science and Technology* 2013;185(6):898–919. <https://doi.org/10.1080/00102202.2013.764288>.
- [56] Greenberg JB, Katoshevski D. Polydisperse spray diffusion flames in oscillating flow. *Combustion Theory and Modelling* 2016;20(2):349–72. <https://doi.org/10.1080/13647830.2015.1132773>.
- [57] Musa SNA, Saito M, Furuhashi T, Arai M. Evaporation characteristics of a single aqueous urea solution droplet. Kyoto, Japan. 2006.
- [58] Wang TJ, Baek SW, Lee SY, Kang DH, Yeo GK. Experimental investigation on evaporation of urea-water-solution droplet for SCR applications. *AIChE Journal* 2009;55(12):3267–76. <https://doi.org/10.1002/aic.11939>.
- [59] Wei L, Youtong Z, Asif M. Investigation on UWS evaporation for vehicle SCR applications. *AIChE Journal* 2016;62(3):880–90. <https://doi.org/10.1002/aic.15078>.
- [60] Brenn G. Concentration fields in evaporating droplets. *International Journal of Heat and Mass Transfer* 2005;48(2):395–402. <https://doi.org/10.1016/j.ijheatmasstransfer.2004.07.039>.
- [61] Brenn G, Deviprasath LJ, Durst F, Fink C. Evaporation of acoustically levitated multi-component liquid droplets. *International Journal of Heat and Mass Transfer* 2007;50(25-26):5073–86. <https://doi.org/10.1016/j.ijheatmasstransfer.2007.07.036>.
- [62] Kontin S, Höfler A, Koch R, Bauer H-J. Heat and Mass Transfer accompanied by Crystallisation of single Particles containing Urea-water-solution. 2010. Brno, Czech Republic
- [63] Birkhold F, Meingast U, Wassermann P, Deutschmann O. Analysis of the Injection of Urea-Water-Solution for Automotive SCR DeNOx-Systems: Modeling of Two-Phase Flow and Spray/Wall-Interaction. SAE Technical Paper 2006-01-0643 2006. <https://doi.org/10.4271/2006-01-0643>.
- [64] Lundström A, Snelling T, Morsing P, Gabriellsson P, Senar E, Olsson L. Urea decomposition and HNCO hydrolysis studied over titanium dioxide, Fe-Beta and γ -Alumina. *Applied Catalysis B: Environmental* 2011;106(3-4):273–9. <https://doi.org/10.1016/j.apcatb.2011.05.010>.
- [65] Abu-Ramadan E, Saha K, Li X. Numerical Modeling of the Impinging Process of Urea-Water Solution Spray on the Heated Walls of SCR Systems. SAE Technical Paper 2012;(2012-01-1301). <https://doi.org/10.4271/2012-01-1301>.
- [66] Stein M, Bykov V, Maas U. The Effect of Evaporation Models on Urea Decomposition from Urea-Water-Solution Droplets in SCR Conditions. *Emission Control Science and Technology* 2017;3(4):263–74. <https://doi.org/10.1007/s40825-017-0075-1>.
- [67] Stein M, Bykov V, Bertóiné Abai A, Janzer C, Maas U, Deutschmann O, et al. A reduced model for the evaporation and decomposition of urea–water solution droplets. *International Journal of Heat and Fluid Flow* 2018;70:216–25. <https://doi.org/10.1016/j.ijheatfluidflow.2018.02.005>.
- [68] Habchi C, Quan S, Drennan S, Bohbot J. Towards Quantitative Prediction of Urea Thermo-Hydrolysis and Deposits Formation in Exhaust Selective Catalytic Reduction (SCR) Systems. SAE Technical Paper Series. SAE International 400 Commonwealth Drive, Warrendale, PA, United States; 2019. <https://doi.org/10.4271/2019-01-0992>.
- [69] Hulgaard T, Dam-Johansen K. Homogeneous nitrous oxide formation and destruction under combustion conditions. *AIChE Journal* 1993;39(8):1342–54. <https://doi.org/10.1002/aic.690390811>.
- [70] Rota R, Antos D, Zanoelo EF, Carra S. Experimental Study and Kinetic Modelling of Nitric Oxide Reduction with Ammonia. *Combustion Science and Technology* 2001;163(1):25–47. <https://doi.org/10.1080/00102200108952150>.
- [71] Kasuya F, Glarborg P, Johnsson JE, Dam-Johansen K. The thermal DeNOx process: Influence of partial pressures and temperature. *Chemical Engineering Science* 1995;50(9):1455–66. [https://doi.org/10.1016/0009-2509\(95\)00008-S](https://doi.org/10.1016/0009-2509(95)00008-S).
- [72] Glarborg P, Dam-Johansen K, Miller JA, Kee RJ, Coltrin ME. Modeling the thermal DeNOx process in flow reactors. Surface effects and Nitrous Oxide formation. *International Journal of Chemical Kinetics* 1994;26(4):421–36. <https://doi.org/10.1002/kin.550260405>.
- [73] Miller JA, Glarborg P. Modeling the thermal De-NOx process: Closing in on a final solution. *International Journal of Chemical Kinetics* 1999;31(11):757–65. [https://doi.org/10.1002/\(SICI\)1097-4601\(1999\)31:11<757::AID-JCK1>3.0.CO;2-V](https://doi.org/10.1002/(SICI)1097-4601(1999)31:11<757::AID-JCK1>3.0.CO;2-V).
- [74] Skreiberg Ø, Kilpinen P, Glarborg P. Ammonia chemistry below 1400 K under fuel-rich conditions in a flow reactor. *Combustion and Flame* 2004;136(4):501–18. <https://doi.org/10.1016/j.combustflame.2003.12.008>.
- [75] Smith J, Phillips J, Graham A, Steele R, Redondo A, Coons J. Homogeneous Chemistry in Lean-Burn Exhaust Mixtures. *The Journal of Physical Chemistry A* 1997;101(48):9157–62. <https://doi.org/10.1021/jp9716647>.
- [76] Torkashvand B, Lott P, Zengel D, Maier L, Hettel M, Grunwaldt J-D, et al. Homogeneous oxidation of light alkanes in the exhaust of turbocharged lean-burn gas engines. *Chemical Engineering Journal* 2019;377:119800. <https://doi.org/10.1016/j.cej.2018.08.186>.
- [77] Schmitt S, Schwarz S, Ruwe L, Horstmann J, Sabath F, Maier L, et al. Homogeneous conversion of NOx and NH3 with CH4, CO, and C2H4 at the diluted conditions of exhaust-gases of lean operated natural gas engines. *International Journal of Chemical Kinetics* 2020. <https://doi.org/10.1002/kin.21435>.
- [78] Günter T, Pesek J, Schäfer K, Bertóiné Abai A, Casapu M, Deutschmann O, et al. Cu-SSZ-13 as pre-turbine NOx-removal-catalyst: Impact of pressure and catalyst poisons. *Applied Catalysis B: Environmental* 2016;198:548–57. <https://doi.org/10.1016/j.apcatb.2016.06.005>.
- [79] Bertóiné Abai A, Zengel D, Janzer C, Maier L, Grunwaldt J-D, Olzmann M, et al. Effect of NO2 on Gas-Phase Reactions in Lean NOx/NH3/O2/H2O Mixtures at Conditions Relevant for Exhaust Gas Aftertreatment. SAE Technical Paper 2021; (2021-01-5005). <https://doi.org/10.4271/2021-01-5005>.
- [80] Caton JA, Siebers DL. Comparison of Nitric Oxide Removal by Cyanuric Acid and by Ammonia. *Combustion Science and Technology* 1989;65(4-6):277–93. <https://doi.org/10.1080/00102208908924054>.
- [81] Miller JA, Bowman CT. Kinetic modeling of the reduction of nitric oxide in combustion products by isocyanic acid. *International Journal of Chemical Kinetics* 1991;23(4):289–313. <https://doi.org/10.1002/kin.550230403>.
- [82] Glarborg P, Kristensen PG, Jensen SH, Dam-Johansen K. A flow reactor study of HNCO oxidation chemistry. *Combustion and Flame* 1994;98(3):241–58. [https://doi.org/10.1016/0010-2180\(94\)90239-9](https://doi.org/10.1016/0010-2180(94)90239-9).
- [83] Chen Z-C, Yang W-J, Zhou J-H, Lv H-K, Liu J-Z, Cen K-F. HNCO hydrolysis performance in urea-water solution thermohydrolysis process with and without catalysts. *Journal of Zhejiang University-SCIENCE A* 2010;11(11):849–56. <https://doi.org/10.1631/jzus.A0900798>.
- [84] Glarborg P, Miller JA, Ruscic B, Klippenstein SJ. Modeling nitrogen chemistry in combustion. *Progress in Energy and Combustion Science* 2018;67:31–68. <https://doi.org/10.1016/j.pecs.2018.01.002>.
- [85] Koebel M, Strutz EO. Thermal and Hydrolytic Decomposition of Urea for Automotive Selective Catalytic Reduction Systems: Thermochemical and Practical Aspects. *Industrial & Engineering Chemistry Research* 2003;42(10):2093–100. <https://doi.org/10.1021/ie020950o>.
- [86] Yim SD, Kim SJ, Baik JH, Nam I-S, Mok YS, Lee J-H, et al. Decomposition of Urea into NH3 for the SCR Process. *Industrial & Engineering Chemistry Research* 2004;43(16):4856–63. <https://doi.org/10.1021/ie034052j>.
- [87] Piazzesi G, Kröcher O, Elsener M, Wokaun A. Adsorption and hydrolysis of isocyanic acid on TiO2. *Applied Catalysis B: Environmental* 2006;65(1-2):55–61. <https://doi.org/10.1016/j.apcatb.2005.12.018>.
- [88] Piazzesi G, Devadas M, Kröcher O, Elsener M, Wokaun A. Isocyanic acid hydrolysis over Fe-ZSM5 in urea-SCR. *Catalysis Communications* 2006;7(8):600–3. <https://doi.org/10.1016/j.catcom.2006.01.022>.
- [89] Czekaj I, Kröcher O, Piazzesi G. DFT calculations, DRIFT spectroscopy and kinetic studies on the hydrolysis of isocyanic acid on the TiO2-anatase (101) surface. *Journal of Molecular Catalysis A: Chemical* 2008;280(1-2):68–80. <https://doi.org/10.1016/j.molcata.2007.10.027>.
- [90] Czekaj I, Kröcher O. Decomposition of Urea in the SCR Process: Combination of DFT Calculations and Experimental Results on the Catalytic Hydrolysis of Isocyanic Acid on TiO2 and Al2O3. *Topics in Catalysis* 2009;52(13-20):1740–5. <https://doi.org/10.1007/s11244-009-9344-8>.
- [91] Kleemann M, Elsener M, Koebel M, Wokaun A. Hydrolysis of Isocyanic Acid on SCR Catalysts. *Industrial & Engineering Chemistry Research* 2000;39(11):4120–6. <https://doi.org/10.1021/ie9906161>.
- [92] Hauck P, Jentys A, Lercher JA. Surface chemistry and kinetics of the hydrolysis of isocyanic acid on anatase. *Applied Catalysis B: Environmental* 2007;70(1-4):91–9. <https://doi.org/10.1016/j.apcatb.2005.12.025>.
- [93] Piazzesi G, Elsener M, Kröcher O, Wokaun A. Influence of NO2 on the hydrolysis of isocyanic acid over TiO2. *Applied Catalysis B: Environmental* 2006;65(3-4):169–74. <https://doi.org/10.1016/j.apcatb.2006.01.002>.
- [94] Ma Y, Wu X, Zhang J, Ran R, Weng D. Urea-related reactions and their active sites over Cu-SAPO-34: Formation of NH3 and conversion of HNCO. *Applied Catalysis B: Environmental* 2018;227:198–208. <https://doi.org/10.1016/j.apcatb.2018.01.026>.
- [95] Seneque M, Can F, Duprez D, Courtois X. NOx Selective Catalytic Reduction (NOx-SCR) by Urea: Evidence of the Reactivity of HNCO, Including a Specific Reaction Pathway for NOx Reduction Involving NO + NO2. *ACS Catalysis* 2016;6(7):4064–7. <https://doi.org/10.1021/acscatal.6b00785>.
- [96] Grossale A, Nova I, Tronconi E, Chatterjee D, Weibel M. NH3–NO/NO2 SCR for Diesel Exhausts Aftertreatment: Reactivity, Mechanism and Kinetic Modelling of Commercial Fe- and Cu-Promoted Zeolite Catalysts. *Topics in Catalysis* 2009;52(13-20):1837–41. <https://doi.org/10.1007/s11244-009-9354-6>.
- [97] Hauck P, Jentys A, Lercher JA. On the quantitative aspects of hydrolysis of isocyanic acid on TiO2. *Catalysis Today* 2007;127(1-4):165–75. <https://doi.org/10.1016/j.cattod.2007.05.012>.
- [98] Kröcher O, Elsener M, Koebel M. An ammonia and isocyanic acid measuring method for soot containing exhaust gases. *Analytica Chimica Acta* 2005;537(1-2):393–400. <https://doi.org/10.1016/j.aca.2004.12.082>.
- [99] Suarez-Bertoa R, Astorga C. Isocyanic acid and ammonia in vehicle emissions. *Transportation Research Part D: Transport and Environment* 2016;49:259–70. <https://doi.org/10.1016/j.trd.2016.08.039>.
- [100] Brack W, Heine B, Birkhold F, Kruse M, Schoch G, Tischer S, et al. Kinetic modeling of urea decomposition based on systematic thermogravimetric analyses of urea and its most important by-products. *Chemical Engineering Science* 2014;106:1–8. <https://doi.org/10.1016/j.ces.2013.11.013>.
- [101] Sadashiva Prabhu S, Nayak NS, Kapilan N, Hindasageri V. An experimental and numerical study on effects of exhaust gas temperature and flow rate on deposit formation in Urea-Selective Catalytic Reduction (SCR) system of modern

- automobiles. *Applied Thermal Engineering* 2017;111:1211–31. <https://doi.org/10.1016/j.applthermaleng.2016.09.134>.
- [102] Börnhorst M, Deuschmann O. Single droplet impingement of urea water solution on a heated substrate. *International Journal of Heat and Fluid Flow* 2018;69:55–61. <https://doi.org/10.1016/j.ijheatfluidflow.2017.10.007>.
- [103] Quissek M, Lauer T, García-Afonso O, Fowles S. Identification of Film Breakup for a Liquid Urea-Water-Solution and Application to CFD. SAE Technical Paper 2019; (2019-01-0983). <https://doi.org/10.4271/2019-01-0983>.
- [104] Bernardin JD, Stebbins CJ, Mudawar I. Effects of surface roughness on water droplet impact history and heat transfer regimes. *International Journal of Heat and Mass Transfer* 1996;40(1):73–88. [https://doi.org/10.1016/S0017-9310\(96\)00067-1](https://doi.org/10.1016/S0017-9310(96)00067-1).
- [105] Bernardin JD, Stebbins CJ, Mudawar I. Mapping of impact and heat transfer regimes of water drops impinging on a polished surface. *International Journal of Heat and Mass Transfer* 1997;40(2):247–67. [https://doi.org/10.1016/0017-9310\(96\)00119-6](https://doi.org/10.1016/0017-9310(96)00119-6).
- [106] Bernardin JD, Mudawar I. The Leidenfrost Point: Experimental Study and Assessment of Existing Models. *Journal of Heat Transfer* 1999;121(4):894. <https://doi.org/10.1115/1.2826080>.
- [107] Karl A, Frohn A. Experimental investigation of interaction processes between droplets and hot walls. *Physics of Fluids* 2000;12(4):785–96. <https://doi.org/10.1063/1.870335>.
- [108] Šikalo S, Marengo M, Tropea C, Ganić E. Analysis of impact of droplets on horizontal surfaces. *Experimental Thermal and Fluid Science* 2002;25(7):503–10. [https://doi.org/10.1016/S0894-1777\(01\)00109-1](https://doi.org/10.1016/S0894-1777(01)00109-1).
- [109] Šikalo S, Tropea C, Ganić EN. Impact of droplets onto inclined surfaces. *Journal of Colloid and Interface Science* 2005;286(2):661–9. <https://doi.org/10.1016/j.jcis.2005.01.050>.
- [110] Šikalo S, Wilhelm H-D, Roisman IV, Jakirlić S, Tropea C. Dynamic contact angle of spreading droplets: Experiments and simulations. *Physics of Fluids* 2005;17(6):062103. <https://doi.org/10.1063/1.1928828>.
- [111] Roisman IV, Opfer L, Tropea C, Raessi M, Mostaghimi J, Chandra S. Drop impact onto a dry surface: Role of the dynamic contact angle. *Colloids and Surfaces A: Physicochemical and Engineering Aspects* 2008;322(1-3):183–91. <https://doi.org/10.1016/j.colsurfa.2008.03.005>.
- [112] Cossali GE, Marengo M, Santini M. Thermally induced secondary drop atomisation by single drop impact onto heated surfaces. *International Journal of Heat and Fluid Flow* 2008;29(1):167–77. <https://doi.org/10.1016/j.ijheatfluidflow.2007.09.006>.
- [113] Castanet G, Liénart T, Lemoine F. Dynamics and temperature of droplets impacting onto a heated wall. *International Journal of Heat and Mass Transfer* 2009;52(3-4):670–9. <https://doi.org/10.1016/j.ijheatmasstransfer.2008.07.024>.
- [114] Marengo M, Antonini C, Roisman IV, Tropea C. Drop collisions with simple and complex surfaces. *Current Opinion in Colloid & Interface Science* 2011;16(4):292–302. <https://doi.org/10.1016/j.cocis.2011.06.009>.
- [115] Berberović E, Roisman IV, Jakirlić S, Tropea C. Inertia dominated flow and heat transfer in liquid drop spreading on a hot substrate. *International Journal of Heat and Fluid Flow* 2011;32(4):785–95. <https://doi.org/10.1016/j.ijheatfluidflow.2011.05.001>.
- [116] Sinha-Ray S, Sinha-Ray S, Yarin AL, Weickgenannt CM, Emmert J, Tropea C. Drop impact cooling enhancement on nano-textured surfaces. Part II: Results of the parabolic flight experiments [zero gravity (0g) and supergravity (1.8g)]. *International Journal of Heat and Mass Transfer* 2014;70:1107–14. <https://doi.org/10.1016/j.ijheatmasstransfer.2013.11.008>.
- [117] Roisman IV, Lembach A, Tropea C. Drop splashing induced by target roughness and porosity: The size plays no role. *Advances in Colloid and Interface Science* 2015;222:615–21. <https://doi.org/10.1016/j.cis.2015.02.004>.
- [118] Schremb M, Roisman IV, Tropea C. Transient effects in ice nucleation of a water drop impacting onto a cold substrate. *Physical Review E* 2017;95(2-1):022805. <https://doi.org/10.1103/PhysRevE.95.022805>.
- [119] Celata GP, Cumo M, Mariani A, Zumbo G. Visualization of the impact of water drops on a hot surface: Effect of drop velocity and surface inclination. *Heat and Mass Transfer* 2006;42(10):885–90. <https://doi.org/10.1007/s00231-006-0139-1>.
- [120] Hutchings IM, Martin GD, Hoath SD. High Speed Imaging and Analysis of Jet and Drop Formation. *Journal of Imaging Science and Technology* 2007;51(5):438. [https://doi.org/10.2352/J.ImagingSci.Technol.\(2007\)51:5\(438\)](https://doi.org/10.2352/J.ImagingSci.Technol.(2007)51:5(438)).
- [121] Thoroddsen ST, Etoh TG, Takehara K. High-Speed Imaging of Drops and Bubbles. *Annual Review of Fluid Mechanics* 2008;40(1):257–85. <https://doi.org/10.1146/annurev.fluid.40.111406.102215>.
- [122] Thoraval M-J, Takehara K, Etoh TG, Thoroddsen ST. Drop impact entrapment of bubble rings. *Journal of Fluid Mechanics* 2013;724:234–58. <https://doi.org/10.1017/jfm.2013.147>.
- [123] Gottfried BS, Lee CJ, Bell KJ. The Leidenfrost phenomenon: Film boiling of liquid droplets on a flat plate. *International Journal of Heat and Mass Transfer* 1966;9(11):1167–88. [https://doi.org/10.1016/0017-9310\(66\)90112-8](https://doi.org/10.1016/0017-9310(66)90112-8).
- [124] Rein M. Interactions between Drops and Hot Surfaces. Rein M. (eds) *Drop-Surface Interactions*. CISM International Centre for Mechanical Sciences (Courses and Lectures), Springer, Vienna. 456; 2002. p. 185–217. <https://doi.org/10.1007/978-3-7091-2594-6-6>.
- [125] Bai C, Gosman AD. Development of Methodology for Spray Impingement Simulation. SAE Technical Paper 950283 1995. <https://doi.org/10.4271/950283>.
- [126] Rioboo R, Tropea C, Marengo M. Outcomes from a Drop Impact on Solid Surfaces. *Atomization and Sprays* 2001;11(2):12. <https://doi.org/10.1615/AtomizSpr.v11.i2.40>.
- [127] Stow CD, Hadfield MG. An Experimental Investigation of Fluid Flow Resulting from the Impact of a Water Drop with an Unyielding Dry Surface. *Proceedings of the Royal Society A: Mathematical, Physical and Engineering Sciences* 1981;373(1755):419–41. <https://doi.org/10.1098/rspa.1981.0002>.
- [128] Mundo C, Sommerfeld M, Tropea C. Droplet-wall collisions: Experimental studies of the deformation and breakup process. *International Journal of Multiphase Flow* 1995;21(2):151–73. [https://doi.org/10.1016/0301-9322\(94\)00069-V](https://doi.org/10.1016/0301-9322(94)00069-V).
- [129] Moreira A, Moita AS, Panão MR. Advances and challenges in explaining fuel spray impingement: How much of single droplet impact research is useful? *Progress in Energy and Combustion Science* 2010;36(5):554–80. <https://doi.org/10.1016/j.pecs.2010.01.002>.
- [130] Staat HJJ, Tran T, Geerdink B, Riboux G, Sun C, Gordillo JM, et al. Phase diagram for droplet impact on superheated surfaces. *Journal of Fluid Mechanics* 2015;779. <https://doi.org/10.1017/jfm.2015.465>.
- [131] Liang G, Shen S, Guo Y, Zhang J. Boiling from liquid drops impact on a heated wall. *International Journal of Heat and Mass Transfer* 2016;100:48–57. <https://doi.org/10.1016/j.ijheatmasstransfer.2016.04.061>.
- [132] Kuhnke D. *Spray wall interaction modelling by dimensionless data analysis*. Aachen, Germany: RWTH Aachen University; 2004. PhD thesis.
- [133] Moita AS, Moreira A. Drop impacts onto cold and heated rigid surfaces: Morphological comparisons, disintegration limits and secondary atomization. *International Journal of Heat and Fluid Flow* 2007;28(4):735–52. <https://doi.org/10.1016/j.ijheatfluidflow.2006.10.004>.
- [134] Tran T, Staat HJJ, Prosperetti A, Sun C, Lohse D. Drop impact on superheated surfaces. *Physical review letters* 2012;108(3):036101. <https://doi.org/10.1103/PhysRevLett.108.036101>.
- [135] Breitenbach J, Roisman IV, Tropea C. *Phenomena of Drop Impact on Hot Surfaces: Pure Newtonian Liquids*. 2015. Tainan, Taiwan
- [136] Bertola V. An impact regime map for water drops impacting on heated surfaces. *International Journal of Heat and Mass Transfer* 2015;85:430–7. <https://doi.org/10.1016/j.ijheatmasstransfer.2015.01.084>.
- [137] Khavari M, Sun C, Lohse D, Tran T. Fingering patterns during droplet impact on heated surfaces. *Soft matter* 2015;11(17):3298–303. <https://doi.org/10.1039/c4sm02878c>.
- [138] Liang G, Mudawar I. Review of drop impact on heated walls. *International Journal of Heat and Mass Transfer* 2017;106:103–26. <https://doi.org/10.1016/j.ijheatmasstransfer.2016.10.031>.
- [139] Richter B, Dullenkopf K, Bauer H-J. Investigation of secondary droplet characteristics produced by an isoctane drop chain impact onto a heated piston surface. *Experiments in Fluids* 2005;39(2):351–63. <https://doi.org/10.1007/s00348-005-1018-0>.
- [140] Wang A-B, Lin C-H, Cheng C-C. Pattern analysis of a single droplet impinging onto a heated plate. *Heat Transfer Asian Research* 2005;34(3):579–94.
- [141] Nishio S, Hirata M. Direct contact phenomenon between a liquid droplet and high temperature solid surface. 6th International Heat Transfer Conference, Toronto, Canada 1978;(1):245–50.
- [142] Kunihiide M, Michiyoshi I. Effects of the initial size of water droplet on its evaporation on heated surfaces. *International Journal of Heat and Mass Transfer* 1979;22(6):979–81. [https://doi.org/10.1016/0017-9310\(79\)90041-3](https://doi.org/10.1016/0017-9310(79)90041-3).
- [143] Yao S-C, Cai KY. The dynamics and Leidenfrost temperature of drops impacting on a hot surface at small angles. *Experimental Thermal and Fluid Science* 1988;1(4):363–71. [https://doi.org/10.1016/0894-1777\(88\)90016-7](https://doi.org/10.1016/0894-1777(88)90016-7).
- [144] Kang BS, Lee DH. On the dynamic behavior of a liquid droplet impacting upon an inclined heated surface. *Experiments in Fluids* 2000;29(4):380–7. <https://doi.org/10.1007/s003489900104>.
- [145] Frost W, Kippenhan CJ. Bubble growth and heat-transfer mechanisms in the forced convection boiling of water containing a surface active agent. *International Journal of Heat and Mass Transfer* 1967;10(7):931–49. [https://doi.org/10.1016/0017-9310\(67\)90070-1](https://doi.org/10.1016/0017-9310(67)90070-1).
- [146] Yang YM, Maa JR. Pool Boiling of Dilute Surfactant Solutions. *Journal of Heat Transfer* 1983;105(1):190. <https://doi.org/10.1115/1.3245541>.
- [147] Manzello SL, Yang JC. On the collision dynamics of a water droplet containing an additive on a heated solid surface. *Proceedings of the Royal Society A: Mathematical, Physical and Engineering Sciences* 2002;458(2026):2417–44. <https://doi.org/10.1098/rspa.2002.0980>.
- [148] Cui Q, Chandra S, McCahan S. The Effect of Dissolving Gases or Solids in Water Droplets Boiling on a Hot Surface. *Journal of Heat Transfer* 2001;123(4):719. <https://doi.org/10.1115/1.1376394>.
- [149] Qiao YM, Chandra S. Experiments on adding a surfactant to water drops boiling on a hot surface. *Proceedings of the Royal Society A: Mathematical, Physical and Engineering Sciences* 1997;453(1959):673–89. <https://doi.org/10.1098/rspa.1997.0038>.
- [150] Börnhorst M. *Urea-Water Sprays in NOx Emission Control Systems: Interaction with Solid Walls and Deposit Formation*. Karlsruhe, Germany: Karlsruhe Institute of Technology; 2019. PhD thesis.
- [151] Tropea C, Roisman IV. Modeling of spray impact on solid surfaces. *Atomization and Sprays* 2000;10(3-5):387–408. <https://doi.org/10.1615/AtomizSpr.v10.i3-5.80>.
- [152] Roisman IV, Prunet-Foch B, Tropea C, Vignes-Adler M. Multiple Drop Impact onto a Dry Solid Substrate. *Journal of Colloid and Interface Science* 2002;256(2):396–410. <https://doi.org/10.1006/jcis.2002.8683>.
- [153] Roisman IV. Dynamics of inertia dominated binary drop collisions. *Physics of Fluids* 2004;16(9):3438–49. <https://doi.org/10.1063/1.1777584>.
- [154] Mundo C, Tropea C, Sommerfeld M. Numerical and experimental investigation of spray characteristics in the vicinity of a rigid Wall. *Experimental Thermal and*

- Fluid Science 1997;15(3):228–37. [https://doi.org/10.1016/S0894-1777\(97\)00015-0](https://doi.org/10.1016/S0894-1777(97)00015-0).
- [155] Kalantari D, Tropea C. Spray impact onto flat and rigid walls: Empirical characterization and modelling. *International Journal of Multiphase Flow* 2007; 33(5):525–44. <https://doi.org/10.1016/j.ijmultiphaseflow.2006.09.008>.
- [156] Stanton DW, Rutland CJ. Modeling fuel film formation and wall interaction in diesel engines. *SAE Transactions* 1996;(105):808–24.
- [157] Senda J, Fujimoto HG. Multidimensional Modeling of Impinging Sprays on the Wall in Diesel Engines. *Applied Mechanics Reviews* 1999;52(4):119–38. <https://doi.org/10.1115/1.3098930>.
- [158] Bai CX, Rusche H, Gosman AD. Modeling of gasoline spray impingement. *Atomization and Sprays* 2002;12(1-3):1–28. <https://doi.org/10.1615/AtomizSpr.v12.i1.23.10>.
- [159] Han Z, Xu Z, Trigui N. Spray/wall interaction models for multidimensional engine simulation. *International Journal of Engine Research* 2000;1(1):127–46. <https://doi.org/10.1243/1468087001545308>.
- [160] Breitenbach J, Roisman IV, Tropea C. From drop impact physics to spray cooling models: a critical review. *Experiments in Fluids* 2018;59(3). <https://doi.org/10.1007/s00348-018-2514-3>.
- [161] Puschmann F, Specht E. Transient measurement of heat transfer in metal quenching with atomized sprays. *Experimental Thermal and Fluid Science* 2004; 28(6):607–15. <https://doi.org/10.1016/j.exthermfluidsci.2003.09.004>.
- [162] Tenzer FM, Roisman IV, Tropea C. Fast transient spray cooling of a hot thick target. *Journal of Fluid Mechanics* 2019;881:84–103. <https://doi.org/10.1017/jfm.2019.743>.
- [163] Cossali GE, Coghe A, Marengo M. The impact of a single drop on a wetted solid surface. *Experiments in Fluids* 1997;22(6):463–72. <https://doi.org/10.1007/s003480050073>.
- [164] Stanton DW, Rutland CJ. Multi-dimensional modeling of thin liquid films and spray-wall interactions resulting from impinging sprays. *International Journal of Heat and Mass Transfer* 1998;41(20):3037–54. [https://doi.org/10.1016/S0017-9310\(98\)00054-4](https://doi.org/10.1016/S0017-9310(98)00054-4).
- [165] Kittel HM, Roisman IV, Tropea C. Splash of a drop impacting onto a solid substrate wetted by a thin film of another liquid. *Physical Review Fluids* 2018;3(7). <https://doi.org/10.1103/PhysRevFluids.3.073601>.
- [166] Garcia Rosa N, Villedieu P, Dewitte J, Lavergne G. A new droplet-wall interaction model. 10th International Conference on Liquid Atomization and Spray Systems, ICLASS. 2006. Kyoto, Japan
- [167] O'Rourke PJ, Amsden AA. A Spray/Wall Interaction Submodel for the KIVA-3 Wall Film Model. SAE Technical Paper 2000;(2000-01-0271). <https://doi.org/10.4271/2000-01-0271>.
- [168] Smith H, Zöschbauer M, Lauer T. Advanced Spray Impingement Modelling for an Improved Prediction Accuracy of the Ammonia Homogenisation in SCR Systems. *SAE International Journal of Fuels and Lubricants* 2015. <https://doi.org/10.4271/2015-01-1054>.
- [169] Quissek M, Budziankou U, Lauer T. A Novel Approach for the Impingement of AdBlue-Droplets based on Smooth Regime Transitions. SAE Technical Paper 2020;(2020-01-2179). <https://doi.org/10.4271/2020-01-2179>.
- [170] Yarin AL. Drop Impact Dynamics: Splashing, Spreading, Receding, Bouncing.... Annual Review of Fluid Mechanics 2006;38(1):159–92. <https://doi.org/10.1146/annurev.fluid.38.050304.092144>.
- [171] Josslerand C, Thoroddsen ST. Drop Impact on a Solid Surface. *Annual Review of Fluid Mechanics* 2016;48(1):365–91. <https://doi.org/10.1146/annurev-fluid-122414-034401>.
- [172] Scheller BL, Bousfield DW. Newtonian drop impact with a solid surface. *AIChE Journal* 1995;41(6):1357–67. <https://doi.org/10.1002/aic.690410602>.
- [173] Bayer IS, Megaridis CM. Contact angle dynamics in droplets impacting on flat surfaces with different wetting characteristics. *Journal of Fluid Mechanics* 2006; 558:415. <https://doi.org/10.1017/S0022112006000231>.
- [174] Börnhorst M, Cai X, Wörner M, Deutschmann O. Maximum Spreading of Urea Water Solution during Drop Impingement. *Chemical Engineering & Technology* 2019;42(11):2419–27. <https://doi.org/10.1002/ceat.201800755>.
- [175] Wörner M, Samkhaniani N, Cai X, Wu Y, Majumdar A, Marschall H, et al. Spreading and rebound dynamics of sub-millimetre urea-water-solution droplets impinging on substrates of varying wettability. *Applied Mathematical Modelling* 2021;95:53–73. <https://doi.org/10.1016/j.apm.2021.01.038>.
- [176] Nukiyama S. The maximum and minimum values of the heat Q transmitted from metal to boiling water under atmospheric pressure. *International Journal of Heat and Mass Transfer* 1966;9(12):1419–33. [https://doi.org/10.1016/0017-9310\(66\)90138-4](https://doi.org/10.1016/0017-9310(66)90138-4).
- [177] VDI Gesellschaft. VDI-Wärmeatlas. 11. Springer; 2013, ISBN 978-3-540-25503-1. <https://doi.org/10.1007/978-3-642-19981-3>.
- [178] Breitenbach J, Roisman IV, Tropea C. Heat transfer in the film boiling regime: Single drop impact and spray cooling. *International Journal of Heat and Mass Transfer* 2017;110:34–42. <https://doi.org/10.1016/j.ijheatmasstransfer.2017.03.004>.
- [179] Puschmann F. Experimentelle Untersuchung der Spraykühlung zur Qualitätsverbesserung durch definierte Einstellung des Wärmeübergangs. Magdeburg, Germany: Otto von Guericke University of Magdeburg; 2003. PhD Thesis.
- [180] Al-Ahmadi HM, Yao SC. Spray cooling of high temperature metals using high mass flux industrial nozzles. *Experimental Heat Transfer* 2008;21(1):38–54. <https://doi.org/10.1080/08916150701647827>.
- [181] Yao SC, Cox TL. A general heat transfer correlation for impacting water sprays of high-temperature surfaces. *Experimental Heat Transfer* 2010;15(4):207–19. <https://doi.org/10.1080/08916150290082649>.
- [182] Labergue A, Gradeck M, Lemoine F. Comparative study of the cooling of a hot temperature surface using sprays and liquid jets. *International Journal of Heat and Mass Transfer* 2015;81:889–900. <https://doi.org/10.1016/j.ijheatmasstransfer.2014.11.018>.
- [183] Roisman IV, Breitenbach J, Tropea C. Thermal atomisation of a liquid drop after impact onto a hot substrate. *Journal of Fluid Mechanics* 2018;842:87–101. <https://doi.org/10.1017/jfm.2018.123>.
- [184] Wendelstorf J, Spitzer K-H, Wendelstorf R. Spray water cooling heat transfer at high temperatures and liquid mass fluxes. *International Journal of Heat and Mass Transfer* 2008;51(19-20):4902–10. <https://doi.org/10.1016/j.ijheatmasstransfer.2008.01.032>.
- [185] Chaze W, Caballina O, Castanet G, Pierson J-F, Lemoine F, Maillat D. Heat flux reconstruction by inversion of experimental infrared temperature measurements – Application to the impact of a droplet in the film boiling regime. *International Journal of Heat and Mass Transfer* 2019;128:469–78. <https://doi.org/10.1016/j.ijheatmasstransfer.2018.08.069>.
- [186] Cebo-Rudnicka A, Malinowski Z, Buczek A. The influence of selected parameters of spray cooling and thermal conductivity on heat transfer coefficient. *International Journal of Thermal Sciences* 2016;110:52–64. <https://doi.org/10.1016/j.ijthermalsci.2016.06.031>.
- [187] Dunand P, Castanet G, Gradeck M, Maillat D, Lemoine F. Energy balance of droplets impinging onto a wall heated above the Leidenfrost temperature. *International Journal of Heat and Fluid Flow* 2013;44:170–80. <https://doi.org/10.1016/j.ijheatfluidflow.2013.05.021>.
- [188] Chaze W, Caballina O, Castanet G, Lemoine F. Spatially and temporally resolved measurements of the temperature inside droplets impinging on a hot solid surface. *Experiments in Fluids* 2017;58(8). <https://doi.org/10.1007/s00348-017-2375-1>.
- [189] Schweigert D, Damson B, Lüders H, Börnhorst M, Deutschmann O. Heat transfer during spray/wall interaction with urea water solution: An experimental parameter study. *International Journal of Heat and Fluid Flow* 2019;78:108432. <https://doi.org/10.1016/j.ijheatfluidflow.2019.108432>.
- [190] Schweigert D, Damson B, Lüders H, Stephan P, Deutschmann O. The effect of wetting characteristics, thermophysical properties, and roughness on spray-wall heat transfer in selective catalytic reduction systems. *International Journal of Heat and Mass Transfer* 2020;152:119554. <https://doi.org/10.1016/j.ijheatmasstransfer.2020.119554>.
- [191] Liao Y, Dimopoulos Eggenschwiler P, Furrer R, Wang M, Boulouchos K. Heat transfer characteristics of urea-water spray impingement on hot surfaces. *International Journal of Heat and Mass Transfer* 2018;117:447–57. <https://doi.org/10.1016/j.ijheatmasstransfer.2017.10.031>.
- [192] Liao Y, Furrer R, Dimopoulos Eggenschwiler P, Boulouchos K. Experimental investigation of the heat transfer characteristics of spray/wall interaction in diesel selective catalytic reduction systems. *Fuel* 2017;190:163–73. <https://doi.org/10.1016/j.fuel.2016.11.035>.
- [193] Liang G, Mudawar I. Review of spray cooling – Part 1: Single-phase and nucleate boiling regimes, and critical heat flux. *International Journal of Heat and Mass Transfer* 2017;115:1174–205. <https://doi.org/10.1016/j.ijheatmasstransfer.2017.06.029>.
- [194] Liang G, Mudawar I. Review of spray cooling – Part 2: High temperature boiling regimes and quenching applications. *International Journal of Heat and Mass Transfer* 2017;115:1206–22. <https://doi.org/10.1016/j.ijheatmasstransfer.2017.06.022>.
- [195] Rohsenow WM. A method of correlating heat transfer data for surface boiling liquids: *Journal of Heat Transfer*. *Journal of Heat Transfer* 1952;(74):969–76.
- [196] Wruck N. Transientes Sieden von Tropfen beim Wandaufprall. Aachen, Germany: RWTH Aachen University; 1998. PhD thesis.
- [197] Fischer S, Bitto R, Lauer T, Krenn C, Tauer J, Pessl G. Impact of the Turbulence Model and Numerical Approach on the Prediction of the Ammonia Homogenization in an Automotive SCR System. *SAE International Journal of Engines* 2012;5(3):1443–58. <https://doi.org/10.4271/2012-01-1291>.
- [198] Budziankou U, Quissek M, Lauer T. A Fast Modeling Approach for the Numerical Prediction of Urea Deposit Formation. SAE Technical Paper Series. SAE International 400 Commonwealth Drive, Warrendale, PA, United States; 2020. <https://doi.org/10.4271/2020-01-0358>.
- [199] Akao J, Akaki K, Mori S, Moriyama A. Deformation Behaviors of a Liquid Droplet Impingement onto a Hot Metal Surface. *Transactions of the Iron and Steel Institute of Japan* 1980;737–43.
- [200] Wang J, Fu H, Hu Y, Cai Y, Chen K. Experiment investigation on the effects of air assisted SCR spray impingement on wall temperature evolution. *Energy* 2020; 204:117943. <https://doi.org/10.1016/j.energy.2020.117943>.
- [201] Smith H, Lauer T, Mayer M, Pierson S. Optical and Numerical Investigations on the Mechanisms of Deposit Formation in SCR Systems. *SAE International Journal of Fuels and Lubricants* 2014;7(2):525–42. <https://doi.org/10.4271/2014-01-1563>.
- [202] Niwa A, Sakatani S, Matsumura E, Kitamura T. Prediction of Spray Behavior in Injected by Urea SCR Injector and the Reaction Products. *SAE International Journal of Fuels and Lubricants* 2017;10(3). <https://doi.org/10.4271/2017-01-2375>.
- [203] Liao Y, Dimopoulos Eggenschwiler P, Rentsch D, Curto F, Boulouchos K. Characterization of the urea-water spray impingement in diesel selective catalytic reduction systems. *Applied Energy* 2017;205:964–75. <https://doi.org/10.1016/j.apenergy.2017.08.088>.
- [204] Börnhorst M, Langheck S, Weickenmeier H, Dem C, Suntz R, Deutschmann O. Characterization of solid deposits from urea water solution injected into a hot gas

- test rig. *Chemical Engineering Journal* 2019;377:119855. <https://doi.org/10.1016/j.cej.2018.09.016>.
- [205] Wagner W. New vapour pressure measurements for argon and nitrogen and a new method for establishing rational vapour pressure equations. *Cryogenics* 1973;13(8):470–82. [https://doi.org/10.1016/0011-2275\(73\)90003-9](https://doi.org/10.1016/0011-2275(73)90003-9).
- [206] Pinck LA, Kelly MA. The Solubility of Urea in Water. *Journal of the American Chemical Society* 1925;47(8):2170–2. <https://doi.org/10.1021/ja01685a502>.
- [207] Lee F-M, Lahti LE. Solubility of urea in water-alcohol mixtures. *Journal of Chemical & Engineering Data* 1972;17(3):304–6. <https://doi.org/10.1021/jc60054a020>.
- [208] Kovalchuk NM, Trybala A, Starov VM. Evaporation of sessile droplets. *Current Opinion in Colloid & Interface Science* 2014;19(4):336–42. <https://doi.org/10.1016/j.cocis.2014.07.005>.
- [209] Ryddner DT, Trujillo MF. Modeling Urea-Water Solution Droplet Evaporation. *Emission Control Science and Technology* 2015;1(1):80–97. <https://doi.org/10.1007/s40825-014-0006-3>.
- [210] Schmid J, Zarikos I, Terzis A, Roth N, Weigand B. Crystallization of urea from an evaporative aqueous solution sessile droplet at sub-boiling temperatures and surfaces with different wettability. *Experimental Thermal and Fluid Science* 2018; 91:80–8. <https://doi.org/10.1016/j.expthermflusc.2017.10.008>.
- [211] Bender A, Stephan P, Gambaryan-Roisman T. A fully coupled numerical model for deposit formation from evaporating urea-water drops. *International Journal of Heat and Mass Transfer* 2020;159:120069. <https://doi.org/10.1016/j.ijheatmasstransfer.2020.120069>.
- [212] Budavari S, Ed.. The Merck Index Eleventh Edition. Chemical & Engineering News 1989;67(49). <https://doi.org/10.1021/cen-v067n049.ifc>.
- [213] Carl Roth GmbH + Co. KG. Sicherheitsdatenblatt gemäß Verordnung (EG) Nr. 1907/2006: Biuret. www.carlroth.com.
- [214] Merck KGaA. Sicherheitsdatenblatt gemäß Verordnung (EG) Nr. 1907/2006: Cyanursäure. <http://www.merckmillipore.com>.
- [215] Bann B, Miller SA. Melamine And Derivatives Of Melamine. *Chemical Reviews* 1958;58(1):131–72. <https://doi.org/10.1021/cr50019a004>.
- [216] Carl Roth GmbH + Co. KG. Sicherheitsdatenblatt gemäß Verordnung (EG) Nr. 1907/2006: Melamin. www.carlroth.com.
- [217] Stradella L, Argentero M. A study of the thermal decomposition of urea, of related compounds and thiourea using DSC and TG-EGA. *Thermochimica Acta* 1993;219: 315–23. [https://doi.org/10.1016/0040-6031\(93\)80508-8](https://doi.org/10.1016/0040-6031(93)80508-8).
- [218] Koryakin A.G. & Gal'perin, V.A. & Sarbaev, A.N. & Finkel'shtein, A.I. Thermography of urea and its pyrolysis products. *Zh Org Khim (Russian Journal of Organic Chemistry)* 1971;(7):972–7.
- [219] Fang HL, DaCosta HF. Urea thermolysis and NOx reduction with and without SCR catalysts. *Applied Catalysis B: Environmental* 2003;46(1):17–34. [https://doi.org/10.1016/S0926-3373\(03\)00177-2](https://doi.org/10.1016/S0926-3373(03)00177-2).
- [220] Ebrahimian V, Nicolle A, Habchi C. Detailed modeling of the evaporation and thermal decomposition of urea-water solution in SCR systems. *AICHE Journal* 2012;58(7):1998–2009. <https://doi.org/10.1002/aic.12736>.
- [221] Gan X, Yao D, Wu F, Dai J, Wei L, Li X. Modeling and simulation of urea-water-solution droplet evaporation and thermolysis processes for SCR systems. *Chinese Journal of Chemical Engineering* 2016;24(8):1065–73. <https://doi.org/10.1016/j.cjche.2016.04.026>.
- [222] Tischer S, Börnhorst M, Amsler J, Schoch G, Deutschmann O. Thermodynamics and reaction mechanism of urea decomposition. *Physical chemistry chemical physics : PCCP* 2019;21(30):16785–97. <https://doi.org/10.1039/c9cp01529a>.
- [223] Kuntz C, Kuhn C, Weickenmeier H, Tischer S, Börnhorst M, Deutschmann O. Kinetic modeling and simulation of high-temperature by-product formation from urea decomposition. *Chemical Engineering Science* 2021;246:116876. <https://doi.org/10.1016/j.ces.2021.116876>.
- [224] Eichelbaum M, Siemer AB, Farrauto RJ, Castaldi MJ. The impact of urea on the performance of metal-exchanged zeolites for the selective catalytic reduction of NOx—Part II. Catalytic, FTIR, and NMR studies. *Applied Catalysis B: Environmental* 2010;97(1-2):98–107. <https://doi.org/10.1016/j.apcatb.2010.03.028>.
- [225] Bernhard AM, Peitz D, Elsener M, Schildhauer T, Kröcher O. Catalytic urea hydrolysis in the selective catalytic reduction of NOx: Catalyst screening and kinetics on anatase TiO2 and ZrO2. *Catalysis Science & Technology* 2013;3(4): 942–51. <https://doi.org/10.1039/c2cy20668d>.
- [226] Peitz D, Bernhard A, Elsener M, Kröcher O. Laboratory test reactor for the investigation of liquid reducing agents in the selective catalytic reduction of NOx. *The Review of scientific instruments* 2011;82(8):084101. <https://doi.org/10.1063/1.3617463>.
- [227] Kröcher O, Elsener M. Materials for thermohydrolysis of urea in a fluidized bed. *Chemical Engineering Journal* 2009;152(1):167–76. <https://doi.org/10.1016/j.cej.2009.04.030>.
- [228] Strots VO, Santhanam S, Adelman BJ, Griffin GA, Derybowski EM. Deposit Formation in Urea-SCR Systems. *SAE International Journal of Fuels and Lubricants* 2009;2(2):283–9. <https://doi.org/10.4271/2009-01-2780>.
- [229] Bai SZ, Lang SG, Yuan KP, Liu Y, Li GX. Experimental Study of Urea Depositions in Urea-SCR System. *Advanced Materials Research* 2014;937:74–9. <https://doi.org/10.4028/www.scientific.net/AMR.937.74>.
- [230] Weeks CL, Ibeling DR, Han S, Ludwig L, Ayyappan P. Analytical Investigation of Urea Depositions in SCR System. *SAE International Journal of Engines* 2015;8(3). <https://doi.org/10.4271/2015-01-1037>.
- [231] Eakle S, Kroll S, Yau A, Gomez J, Henry C. Investigation of Urea Derived Deposits Composition in SCR Systems and Their Potential Effect on Overall PM Emissions. *SAE Technical Paper* 2016;(2016-01-0989). <https://doi.org/10.4271/2016-01-0989>.
- [232] Ates C, Börnhorst M, Koch R, Eck M, Deutschmann O, Bauer H-J. Morphological characterization of urea derived deposits in SCR systems. *Chemical Engineering Journal* 2021;409:128230. <https://doi.org/10.1016/j.cej.2020.128230>.
- [233] Gehrelein J, Lang A, Palmer G. Optimization of SCR Systems by Integration of Mixture Elements. *MTZ worldwide* 2009;70(3):18–22. <https://doi.org/10.1007/BF03227938>.
- [234] Zhang C, Sun C, Wu M, Lu K. Optimisation design of SCR mixer for improving deposit performance at low temperatures. *Fuel* 2019;237:465–74. <https://doi.org/10.1016/j.fuel.2018.10.025>.
- [235] Schiller S, Brandl M, Hoppenstedt B, de Rudder K. Wire Mesh Mixer Optimization for DEF Deposit Prevention. *SAE Technical Paper Series*. SAE International 400 Commonwealth Drive, Warrendale, PA, United States; 2015. <https://doi.org/10.4271/2015-01-0989>.
- [236] Zheng G, Sampath MK, Alcini W, Salanta G, Kotrba A, Axe B. Design Improvements of Urea SCR Mixing for Medium-Duty Trucks. *SAE Technical Paper Series*. SAE International 400 Commonwealth Drive, Warrendale, PA, United States; 2013. <https://doi.org/10.4271/2013-01-1074>.
- [237] Michelin J, Guilbaud F, Guil A, Newbigging I, Jean E, Reichert M, et al. Advanced Compact SCR Mixer: BlueBox. *SAE Technical Paper Series*. SAE International 400 Commonwealth Drive, Warrendale, PA, United States; 2014. <https://doi.org/10.4271/2014-01-1531>.
- [238] Bhayaraju U, Hassa C. Planar liquid sheet breakup of prefilming and nonprefilming atomizers at elevated pressures. *Atomization and Sprays* 2009;19(12):1147–69. <https://doi.org/10.1615/AtomizSpr.v19.i12.50>.
- [239] Warncke K, Geppert S, Sauer B, Sadiki A, Janicka J, Koch R, et al. Experimental and numerical investigation of the primary breakup of an airblasted liquid sheet. *International Journal of Multiphase Flow* 2017;91:208–24. <https://doi.org/10.1016/j.ijmultiphaseflow.2016.12.010>.
- [240] Bhayaraju F, Giuliani, C. Hassa. Planar liquid sheet breakup of pre- and nonprefilming airblast atomisers at elevated ambient air pressure. *ILASS Europe, 20th Annual Conference on Liquid Atomization and Spray Systems, Orleans, France 2005*.
- [241] Aigner M, Wittig S. Swirl and Counterswirl Effects in Prefilming Airblast Atomizers. *Journal of Engineering for Gas Turbines and Power* 1988;110(1): 105–10. <https://doi.org/10.1115/1.3240072>.
- [242] El-Shanawany MS, Lefebvre AH. Airblast Atomization: Effect of Linear Scale on Mean Drop Size. *Journal of Energy* 1980;4(4):184–9. <https://doi.org/10.2514/3.62472>.
- [243] Rizk NK, Lefebvre AH. Influence of atomizer design features on mean drop size. *AIAA Journal* 1983;21(8):1139–42. <https://doi.org/10.2514/3.8217>.
- [244] Bärw E, Geppert S, Koch R, Bauer H-J. Effect of the Precessing Vortex Core on Primary Atomization. *Zeitschrift für Physikalische Chemie* 2015;229(6):909–29. <https://doi.org/10.1515/zpch-2014-0619>.
- [245] Pringuey T, Cant RS. Robust Conservative Level Set Method for 3D Mixed-Element Meshes — Application to LES of Primary Liquid-Sheet Breakup. *Communications in Computational Physics* 2014;16(2):403–39. <https://doi.org/10.4208/cicp.140213.210214a>.
- [246] Sander W, Weigand B. Direct numerical simulation and analysis of instability enhancing parameters in liquid sheets at moderate Reynolds numbers. *Physics of Fluids* 2008;20(5):053301. <https://doi.org/10.1063/1.2909661>.
- [247] Zuzio D, Estivaleres J-L, Villedieu P, Blanchard G. Numerical simulation of primary and secondary atomization. *Comptes Rendus Mécanique* 2013;341(1-2): 15–25. <https://doi.org/10.1016/j.crme.2012.10.003>.
- [248] Braun S, Wieth L, Holz S, Dauch TF, Keller MC, Chaussonnet G, et al. Numerical prediction of air-assisted primary atomization using Smoothed Particle Hydrodynamics. *International Journal of Multiphase Flow* 2019;114:303–15. <https://doi.org/10.1016/j.ijmultiphaseflow.2019.03.008>.
- [249] Holz S, Braun S, Chaussonnet G, Koch R, Bauer H-J. Close Nozzle Spray Characteristics of a Prefilming Airblast Atomizer. *Energies* 2019;12(14):2835. <https://doi.org/10.3390/en12142835>.
- [250] Nishad K, Ries F, Janicka J, Sadiki A. Analysis of spray dynamics of urea–water-solution jets in a SCR-DeNOx system: An LES based study. *International Journal of Heat and Fluid Flow* 2018;70:247–58. <https://doi.org/10.1016/j.ijheatfluidflow.2018.02.017>.
- [251] Rogó z R, Kapusta Ł, Bachanek J, Vankan J, Teodorczyk A. Improved urea-water solution spray model for simulations of selective catalytic reduction systems. *Renewable and Sustainable Energy Reviews* 2020;120:109616. <https://doi.org/10.1016/j.rser.2019.109616>.
- [252] Varna A, Boulouchos K, Spiteri A, Dimopoulos Eggenschwiler P, Wright YM. Numerical Modelling and Experimental Characterization of a Pressure-Assisted Multi-Stream Injector for SCR Exhaust Gas After-Treatment. *SAE International Journal of Engines* 2014;7(4):2012–21. <https://doi.org/10.4271/2014-01-2822>.
- [253] Frühhaber J, Lieber C, Mattes D, Lauer T, Koch R, Bauer H-J. Modeling the Formation of Urea-Water Sprays from an Air-Assisted Nozzle. *Applied Sciences* 2020;10(16):5723. <https://doi.org/10.3390/app10165723>.
- [254] Naber JD, Siebers DL. Effects of Gas Density and Vaporization on Penetration and Dispersion of Diesel Sprays. *SAE Transactions* 1996;(105):82–111.
- [255] Sazhin SS, Feng G, Heikal MR. A model for fuel spray penetration. *Fuel* 2001;80(15):2171–80. [https://doi.org/10.1016/S0016-2361\(01\)00098-9](https://doi.org/10.1016/S0016-2361(01)00098-9).
- [256] Wurzenberger JC, Wanker R. Multi-Scale SCR Modeling, 1D Kinetic Analysis and 3D System Simulation. *SAE Technical Paper* 2005;(2005-01-0948). <https://doi.org/10.4271/2005-01-0948>.
- [257] Habchi C, Nicolle A, Gillet N. Numerical Study of Deposits Formation in SCR Systems Using Urea-Water Solution Injection. *Journal of Materials Science and Nanotechnology* 2018;6(1). <https://doi.org/10.15744/2348-9812.6.104>.

- [258] Zöschbauer M, Smith H, Lauer T. Advanced SCR Flow Modeling with a Validated Large Eddy Simulation. SAE Technical Paper 2015;(2015-01-1046). <https://doi.org/10.4271/2015-01-1046>.
- [259] Budziankou U, Lauer T, Yu X, Schmidt BM, Cho N. Modeling Approach for a Wiremesh Substrate in CFD Simulation. SAE International Journal of Fuels and Lubricants 2017;(2017-01-0971). <https://doi.org/10.4271/2017-01-0971>.
- [260] Michelin J, Nappez P, Guilbaud F, Hinterberger C, Ottaviani E, Gauthier C, et al. Advanced Close Coupled SCR Compact Mixer Architecture. SAE Technical Paper 2015;(2015-01-1020). <https://doi.org/10.4271/2015-01-1020>.
- [261] Fischer S. Simulation of the urea-water-solution preparation and ammonia homogenization with a validated CFD-model for the optimization of automotive SCR-systems. Vienna, Austria: Vienna University of Technology; 2012. PhD thesis.
- [262] Nishad K, Sadiki A, Janicka J. Numerical Investigation of AdBlue Droplet Evaporation and Thermal Decomposition in the Context of NOx-SCR Using a Multi-Component Evaporation Model. Energies 2018;11(1):222. <https://doi.org/10.3390/en11010222>.
- [263] Nishad K, Stein M, Ries F, Bykov V, Maas U, Deutschmann O, et al. Thermal Decomposition of a Single AdBlue Droplet Including Wall-Film Formation in Turbulent Cross-Flow in an SCR System. Energies 2019;12(13):2600. <https://doi.org/10.3390/en12132600>.
- [264] Shahariar GMH, Wardana MKA, Lim OT. Investigation of urea-water solution spray impingement on the hot surface of automotive SCR system. Journal of Mechanical Science and Technology 2018;32(6):2935–46. <https://doi.org/10.1007/s12206-018-0550-9>.
- [265] Shahariar GH, Lim OT. A Study on Urea-Water Solution Spray-Wall Impingement Process and Solid Deposit Formation in Urea-SCR de-NOx System. Energies 2019; 12(1):125. <https://doi.org/10.3390/en12010125>.
- [266] Börnhorst M, Kuntz C, Tischer S, Deutschmann O. Urea derived deposits in diesel exhaust gas after-treatment: Integration of urea decomposition kinetics into a CFD simulation. Chemical Engineering Science 2020;211:115319. <https://doi.org/10.1016/j.ces.2019.115319>.
- [267] Budziankou U, Börnhorst M, Kuntz C, Deutschmann O, Lauer T. Deposit Formation from Urea Injection: a Comprehensive Modeling Approach. Emission Control Science and Technology 2020;6(2):211–27. <https://doi.org/10.1007/s40825-020-00159-x>.
- [268] Sun Y, Sharma S, Vernham B, Shibata K, Drennan S. Urea Deposit Predictions on a Practical Mid/Heavy Duty Vehicle After-Treatment System. SAE Technical Paper Series. SAE International 400 Commonwealth Drive, Warrendale, PA, United States; 2018. <https://doi.org/10.4271/2018-01-0960>.
- [269] Li M, Zhang Y, Liu X, Zhang Q, Li Z. Numerical Investigation on the Urea Deposit Formation Process in a Selective Catalytic Reduction System of a Diesel Engine Based on a Fluid-Solid Coupling Method. ACS omega 2021;6(8):5921–32. <https://doi.org/10.1021/acsomega.1c00021>.
- [270] Munnannur A, Liu ZG. Development and Validation of a Predictive Model for DEF Injection and Urea Decomposition in Mobile SCR DeNOx Systems. SAE Technical Paper 2010;(2010-01-0889). <https://doi.org/10.4271/2010-01-0889>.
- [271] ANSYS Inc.. ANSYS Fluent CFD Software. 2019. www.ansys.com.
- [272] Dukowicz JK. A particle-fluid numerical model for liquid sprays. Journal of Computational Physics 1980;35(2):229–53. [https://doi.org/10.1016/0021-9991\(80\)90087-X](https://doi.org/10.1016/0021-9991(80)90087-X).
- [273] Incropera FP, DeWitt DP, Bergmann TL, Lavine AS. Fundamentals of heat and mass transfer. 7th. John Wiley & Sons; 2013, ISBN 0471457280.
- [274] Zheng G. CFD Modeling of Urea Spray and Deposits for SCR Systems. SAE Technical Paper 2016;(2016-01-8077). <https://doi.org/10.4271/2016-01-8077>.
- [275] Smith H. Modelling Deposit Formation in Automotive SCR Systems. Vienna, Austria: Vienna University of Technology; 2016. PhD thesis.
- [276] Kuhn C, Schweigert D, Kuntz C, Börnhorst M. Single droplet impingement of urea water solution on heated porous surfaces. International Journal of Heat and Mass Transfer 2021. Submitted for publication.



Marion Börnhorst is head of the “Multiphase Processes and Reactors” group at the Institute for Chemical Technology and Polymer Chemistry (ITCP) at Karlsruhe Institute of Technology (KIT), Germany. She received her Ph.D. in Chemical Engineering in 2019. She received the 2020 award of the Friedrich and Elisabeth Boysen Foundation for her findings on spray/wall interaction and urea deposit formation in mobile NO_x emission control systems. Her current research is centered on multiphase reactive processes. Her research interests include multiphase interaction and chemistry in emission control systems such as spray and droplet impingement on solid targets, film formation and solidification from liquid films. Further more, she works on chemical energy storage as well as multi phase reactor design and optimization.



Olaf Deutschmann holds the Chair in Chemical Technology at the Karlsruhe Institute of Technology (KIT), Germany. He is director at the Institute for Chemical Technology and Polymer Chemistry and at the Institute of Catalysis Research and Technology at KIT. His group works on heterogeneous reactions for the synthesis of chemicals and materials, CO₂ reduction in chemical process industry, reduction of pollutant emissions, combustion, and energy conversion by fuel and electrolysis cells. Special focuses are given to the kinetics of catalytic reactions and their interactions with reactive flows. The software packages DETCHEM and CaRMeN were developed under his guidance. He studied physics and chemistry in Magdeburg, Berlin, and Heidelberg. In 1996, he obtained his PhD from Heidelberg University. As Postdoc he worked on high-temperature catalysis at the University of Minnesota and at the Los Alamos National Laboratory. He joined the Faculty of the Department of Chemistry at the University of Karlsruhe, now KIT, in 2003. Olaf Deutschmann is recipient of the DECHEMA Award, the Hermann-Oberth-Medal, and Fellow of The Combustion Institute.